博士論文

Nickel-cerium oxide catalysts for water electrolysis

（水の電気分解におけるニッケルーセリウム酸化物触媒）

於 俊

Nickel-cerium oxide catalysts for water electrolysis

（水の電気分解におけるニッケルーセリウム酸化物触媒）

於 俊

Jun Yu

Department of Mechanical Engineering

The University of Tokyo

Associate Professor Jean-Jacques Delaunay, Supervisor

August 2018

Abstract

Nickel-cerium oxide catalysts for water electrolysis

By

Jun Yu

For society to adapt to the growing demand for clean energy, renewable energy sources must be utilized to a greater degree. Unfortunately, the vast majority of renewable energy sources, such as wind and solar energy source, can only produce energy intermittently. For these renewable energy sources to replace conventional fossil fuel energy sources, energy storage technologies must be developed. A wide variety of energy conversion devices, including hydrogen fuel-cells, metal-air batteries and photoelectrochemical cells, have been explored to convert electrical or solar energy to chemical energy in order to store the energy produced by renewable energy sources. In all of these devices, the oxygen evolution reaction (OER) is a critical reaction. Because the OER is a four-electron reaction, a large overpotential is needed to overcome the large activation barrier and to drive the electrochemical reaction. Finding a suitable OER catalyst with a high efficiency, low overpotential, low-cost and long-term stability is key to enabling widespread adoption of renewable energy sources.

The best OER catalysts reported so far have generally been iridium or ruthenium-based oxides. The scarcity of both iridium and ruthenium, however, significantly limits the widespread use of these catalysts. First-row transition metals such as Ni- and Co-based oxides, have recently been studied as low-cost alternatives to iridium and

ruthenium-based oxide catalysts. However, the OER activities of these catalysts need be further improved compared with the precious metal catalysts, and the stability is not high enough for industry application. Defects in catalysts can enhance the OER performance of the catalysts by altering the local electron density distribution and providing catalytically active sites. Ceria is an example of a non-stoichiometric catalyst material and Ce-based catalysts have exhibited higher catalytic activity for thermal catalytic reactions when defects are introduced into them. However, whether or not defects in ceria and ceria based catalysts can enhance the catalytic activity in low temperature reactions, such as water electrolysis, has yet to be discerned.

In this dissertation, a series of $Ni_yCe_{100-y}O_x$ ($Ni_{95}Ce_5O_x$, $Ni_{90}Ce_{10}O_x$, $Ni_{75}Ce_{25}O_x$, $Ni_{50}Ce_{50}O_x$, $Ni_{25}Ce_{75}O_x$ and $Ni_{10}Ce_{90}O_x$) with different Ni/Ce ratio are synthesized on NF (Nickel Foam)/NiO substrate with simple dip-coating and annealing methods. The surface NiO obtained from the oxidation of NF can prohibit the diffusion of Ni atoms to the deposited $Ni_yCe_{100-y}O_x$ so that the Ni/Ce ratio will be remained. Oxygen vacancy defects are formed successfully in all the NF/NiO/$Ni_yCe_{100-y}O_x$ (simply referred to $Ni_yCe_{100-y}O_x$) catalysts. The concentration of oxygen vacancy defects for $Ni_{75}Ce_{25}O_x$ and $Ni_{50}Ce_{50}O_x$ catalysts are larger than other $Ni_yCe_{100-y}O_x$ catalysts. The overpotential for the $Ni_{75}Ce_{25}O_x$ and $Ni_{50}Ce_{50}O_x$ catalysts are 338 mV and 341 mV to obtain a current density of 10 mA/cm^2, which are lower than other $Ni_yCe_{100-y}O_x$ catalysts. The better oxygen evolution activities of the $Ni_{75}Ce_{25}O_x$ and $Ni_{50}Ce_{50}O_x$ catalysts are because of their similar larger electrochemically active surface areas, lower Tafel slopes and lower charge-transfer resistances. Additionally, the $Ni_yCe_{100-y}O_x$ catalyst with high Ce content ($Ni_{75}Ce_{25}O_x$) is more stable than the $Ni_yCe_{100-y}O_x$ catalyst with low Ce content ($Ni_{95}Ce_5O_x$) during long-

term water electrolysis with a fixed current density of 10 mA/cm^2.

For industry application, NF is used directly as the substrate instead of NF/NiO in order to simplify the synthesis process and reduce the material costs. A series of $NiCeO_x$ with different dip-coating times ($NiCeO_x$-Y) are synthesized directly on commercially available nickel foam (NF) using a simple, low-cost, environmentally friendly and reproducible synthesis method that consists of first dip-coating the NF in a cerium pre-cursor and then annealing the sample at 400 °C. With the dip-coating times increasing from 1 to 20, the concentration of formed oxygen vacancy defects and the OER performance increase firstly and then decrease for $NiCeO_x$-Y catalysts. The $NiCeO_x$-15 catalyst has the largest concentration of oxygen vacancies and shows the best OER performance with the lowest overpotential of 295 mV for 10 mA/cm^2, and the applied potential remains constant for over 100 h for the fixed current density of 10 mA/cm^2. For the $NiCeO_x$ (simply referred to $NiCeO_x$-15) catalyst, Ni atoms from the nickel foam substrate transfer to the top layer and mix with deposited Ce uniformly to form an amorphous $NiCeO_x$ layer through thermal diffusion. The strong electronic interactions between nickel and cerium oxide induce the formation of oxygen vacancy defects in $NiCeO_x$. The large number of oxygen vacancy defects supply an abundance of active OER sites, resulting in the large electrochemically active surface area of the $NiCeO_x$ (ca. 34 times that of NF) catalyst. The oxygen vacancy defects in the $NiCeO_x$ catalyst also promote the mobility of lattice oxygen and enhance the ionic conductivity, resulting in the low mass-transfer resistance These bring in the high OER performance of the $NiCeO_x$ catalyst. In addition, the HER (hydrogen evolution reaction) activity of the $NiCeO_x$ catalyst is the best among the reported Ce-containing catalysts, including Pt-Ce. The

stable performance of the $NiCeO_x$ catalyst in a two-electrode configuration suggests it is a good candidate as a bifunctional catalyst for the overall water splitting.

In summary, a defect-rich $NiCeO_x$ layer is directly synthesized on nickel foam through a simple two-step dip-coating/annealing method. The $NiCeO_x$ catalyst, with the low overpotential of 295 mV for 10 mA/cm^2 and the stability of over 100 hours, is one of the best OER catalysts ever reported, even outperforming the noble metal catalysts. The excellent performance and low-cost, environmentally friendly and reproducible synthesis method of $NiCeO_x$ catalyst make it suitable for industry application. In addition, the stable performance of the $NiCeO_x$ catalyst in a two-electrode configuration suggests it is a good candidate as a bifunctional catalyst for the overall water splitting. This work might open a new avenue for developing Ce-based OER catalysts with high efficiency and stable performance by introducing defects. Nickel foam can be used directly as the source of nickel for the synthesis of Ni-based catalysts through the thermal diffusion of Ni atoms.

Acknowledgements

I would like to express my sincere gratitude to people who have helped me during my Ph.D. study.

First of all, I would like to express my deepest gratitude towards my advisor Professor Jean-Jacques Delaunay. He has offered me the chance to study in Japan and has taught me a lot during my doctoral study. His attitude towards research has impressed me deeply and stimulated me to devote myself to research. The free environment in his group is helpful for the creative idea.

Many thanks to the jury in my Ph.D. defense, Professor Shigeo Maruyama, Professor Hirofumi Daiguji, Professor Hitoshi Tabata and Associate Professor Junho Choi. They have offered constructive comments and suggestions so that this thesis can be improved greatly.

I would like to express my gratitude towards Professor Naoya Shibata and Ms Mamiko Nakabayashi for their kind help for TEM and STEM measurements. Many thanks to Dr. Wenchao Yu for his assistance for electrochemical measurements.

I would like to express my gratitude to all the members in Delaunay lab. Yalun, Yaerium, Qi, Xin and Wang have helped me a lot with my experiments and life in Japan. Kenji has helped me revise my papers. I would also offer my gratitude to other members, including Li-Chung, Hassan, Shichen, Jinghua and Syazwan for their help in my life in Japan. Many thanks to Dr. Changli Li and Dr. Yanbo Li for their valuable discussion and guidance on my partly experimental results.

I gratefully acknowledge the CSC program for the financial support (201506210091) during my doctoral study.

Last but most importantly, I would like to thank my family and friends for their understanding and support. Especially, many thanks to my wife, Ms Bin Lin. With her help and support, I obtain the degree successfully.

Table of Contents

1. Introduction

1.1 water electrolysis

The fast development of society relies on energy, and the energy now we used is mainly from the tradition fossil fuels including petroleum, natural gas and coal. However, the tradition fossil fuels are limited, and have brought in serious environmental problems during the consumption process.[1] For example, the large number of CO_2 emission from burning fossil fuels has led to the increase in the surface temperature of the earth, resulting in the global warming. [1,2] To solve the energy issue, many researchers have focused on developing alternative clean energy.[3–5] Hydrogen fuel has become attractive in recent years because the product is nothing other than water. Among the hydrogen production pathways, water electrolysis is considered as the cleanest way to produce hydrogen.[5,6] Water electrolysis is an electrochemical reaction in which water will be decomposed into hydrogen (H_2) and oxygen (O_2) with the help of electrical energy as the driving force. The required electrical energy can be produced by the renewable energy sources such as wind, solar and waterfall energy. As shown in Figure 1.1, the abundant renewable energy can be transformed to hydrogen through water electrolysis and stored. Then the stored hydrogen will be used directly as a fuel gas for electricity generation in fuel cells. By making use of the renewable energy sources, the production of hydrogen through water electrolysis has little effect on the environment.[2,6–8]

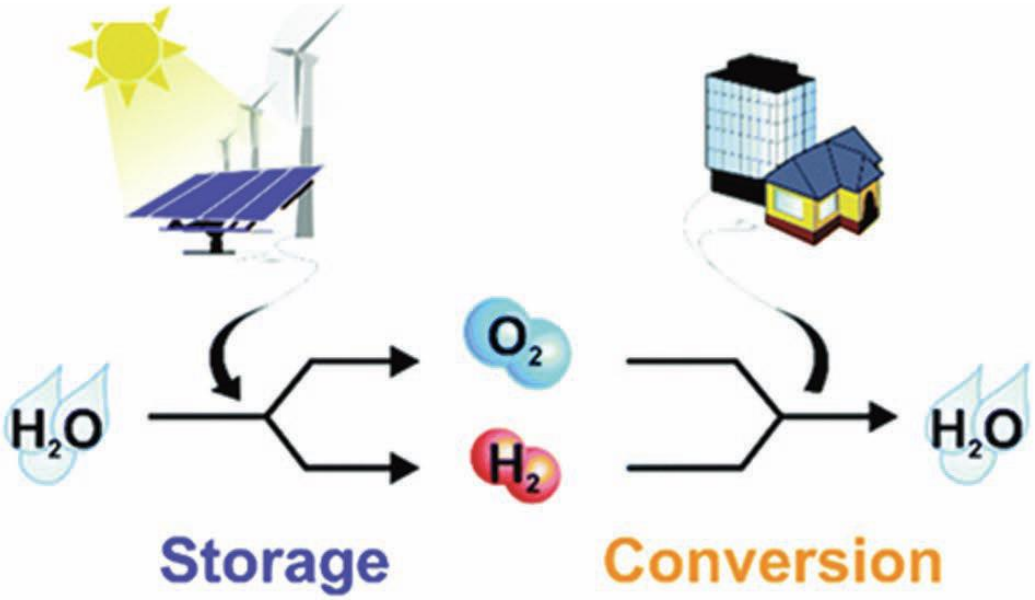

Figure 1.1 Hydrogen and oxygen cycles for energy storage and conversion. Reproduced with permission from Ref. 8.

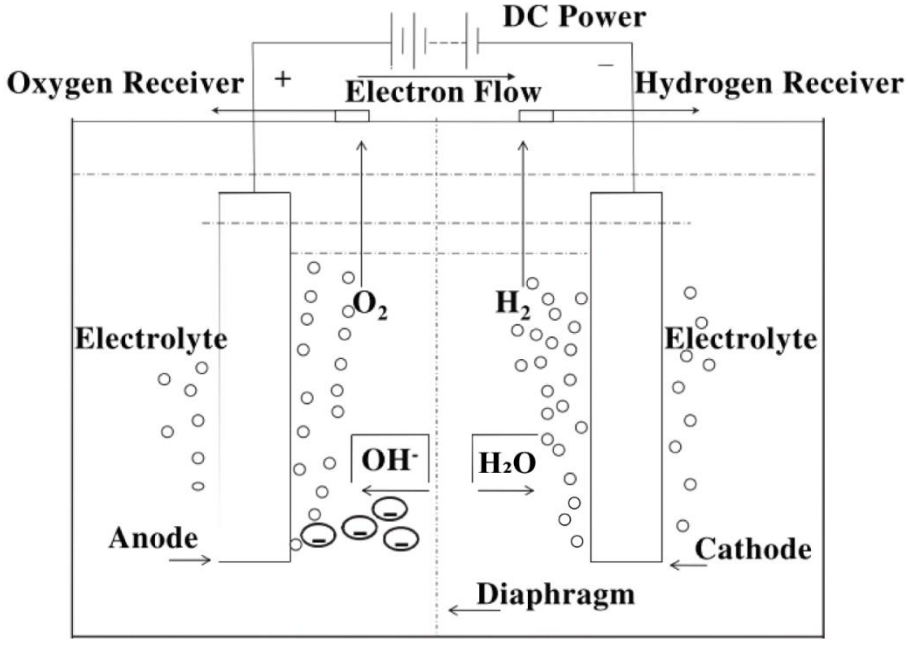

Figure 1.2 A schematic illustration of a basic alkaline water electrolysis system. Reproduced with permission from Ref. 7.

As shown in Figure 1.2, the components of a basic water electrolysis system include two electrodes (cathode and anode), the electrolyte and the power supply. According to the property of the electrolyte, there are acidic water electrolysis and alkaline water electrolysis. The phenomenon of water electrolysis was first discovered in acidic electrolyte, but the alkaline water electrolysis is preferred for industry application. The reason is that the electrodes in acidic electrolyte are more easily corroded and the electrode materials are more expensive compared with that in alkaline electrolyte.[6,7] A basic alkaline water electrolysis system is shown in Figure 1.2. The electrolyte is KOH which consist of ions with good mobility. The applied DC (direct current) power offers the driving force for the water electrolysis. Electrons, in the negative terminal of the DC power supply, transfer to the cathode to react with the adsorbed H_2O, and the H_2O will be reduced to H_2 (Equation 1). In order to keep the electrical charge and ions balance, the generated OH^- transfers to the surface of anode to release electrons and the released electrons will go back to the positive terminal of the DC power supply. During the process, OH^- will be oxidized to O_2 (Equation 2). The overall reaction of the water electrolysis is listed as Equation 3.

Cathode: $2H^+ + 2e \rightarrow H_2$ (1)

Anode: $2OH^- \rightarrow \frac{1}{2}O_2 + H_2O + 2e$ (2)

Overall Reaction: $H_2O \rightarrow H_2 + \frac{1}{2}O_2$ (3)

The water electrolysis reaction can happen only if the thermodynamic resistance is overcome. In other words, the applied voltage should not less than the equilibrium cell voltage (E^0) so that water can be decomposed into hydrogen and oxygen. When

establishing reversibility and without current between cathode and anode reactions, the equilibrium cell voltage is the open cell potential. The equilibrium cell voltage is defined as the equilibrium potential difference between the respective cathode and anode, as described in Equation 4.

$$E^0 = E^0_{anode} - E^0_{cathode} \quad (4)$$

$$\Delta G = nFE^0 \quad (5)$$

The change of the Gibbs free energy (ΔG) of the electrochemical reaction (Equation 3) can be calculated according to the Equation 5, where n is the number of transferred electrons, F is the Faraday constant and E^0 is 1.23 V at room temperature for overall water electrolysis.[7]

1.2 Oxygen Evolution Reaction

The water evolution reaction (OER) in alkaline electrolyte has been described in Equation 2. Compared with the hydrogen evolution reaction (Equation 1), OER is a four electron-proton coupled reaction for per O_2 generation, resulting in much more energy needed for the oxygen evolution reaction. The proposed mechanism for OER in alkaline electrolyte is described from Equation 6 to Equation 10.[9,10]

$$* + OH^- \rightarrow *\text{-}OH + e^- \quad (6)$$

$$*\text{-}OH + OH^- \rightarrow *\text{-}O + e^- + H_2O \quad (7)$$

$$*\text{-}O + OH^- \rightarrow *\text{-}OOH + e^- \quad (8)$$

$$*\text{-}OOH + OH^- \rightarrow *\text{-}O_2 + e^- + H_2O \quad (9)$$

$$*\text{-}O_2 \rightarrow * + O_2 \quad (10)$$

* stands for the OER reactive site. Equation 6 to Equation 9 are the four possible oxygen evolution reactions and Equation 10 is the desorption process of the generated O_2 from the active site.

The key performance parameters for OER include the electrocatalytic activity and the stability. Although the reported activities were measured based on the same electrochemical techniques, the published data sometimes varied among different research groups for the same material.[11] The difference may be related to the different measurement conditions and exhibition format of the activities. In order to make a fair comparison among the large number of OER electrocatalysts, overpotential (η), electrochemically active surface area (ECSA) and tafel slope (b) are taken as the descriptors for the electrocatalytic activity.[12]

Overpotential (η). As described in section 1.1, the applied voltage should not be less than the equilibrium cell voltage (E^0) in order to drive the water splitting reaction. In reality, the applied potential is much larger than E^0 to overcome the sluggish kinetic barriers such as the transfer resistance of electron and ions.[7,13] The applied potential (E), according to the Nernst Equation,[14] can be calculated according to Equation 11.

$$E = E^{0\prime} + \frac{RT}{nF} ln \frac{C_O}{C_R} \tag{11}$$

$$\eta = E - E^0 \tag{12}$$

$E^{0\prime}$ stands for the formal voltage of the overall water splitting reaction, R denotes the universal gas constant, T is the reaction temperature, n is the number of react electrons and F is the Faraday constant. C_O and C_R refer to the concentration of the oxidized and reduced reagents. The overpotential (η) is the difference between the equilibrium cell voltage (E^0) and the applied potential (E), as shown in Equation 12. Notably, the overpotential (η) value is corresponding to the specific current density, and the lower η indicates the higher activity of the electrocatalyst. The overpotential at the current density of 10 mA/cm^2 (geometric area) is usually used to make a comparison among kinds of electrocatalysts because this current density roughly equal to the current density produced by a solar-to-fuels conversion device with 10% efficiency.[10,12]

Electrochemically active surface area (ECSA). The electrochemical active surface area of the electrocatalyst is calculated from the electrochemical double-layer capacitance of the catalyst.[15] The electrochemical double-layer capacitance can be obtained by the cyclic voltammograms (CVs) according to the following steps: 1) A 0.1 V potential range of no obvious Faradaic processes occur is decided by the static CV, and the center of the potential range is within the open-circuit potential (OCP) of the system. 2) CVs with

different scan rates are measured in the 0.1 V non-faradaic potential range, and the measured currents are from the double-layer charging. 3) The slope (C_{DL}) of the current (i_c) at OCP vs scan rates (v) represents the double-layer capacitance (Equation 13). Then the ECSA can be obtained from the double-layer capacitance according to the Equation 14.[12,15–17] The large ECSA can offer abundant active sites for OER, resulting in a high OER activity.

$$i_c = vC_{DL} \tag{13}$$

$$\text{ECSA} = \frac{C_{DL}}{C_S} \tag{14}$$

$$\log(i) = \log(i_0) + \frac{\eta}{b} \tag{15}$$

Tafel slope (b). Tafel slope can be used for reaction mechanism and kinetics analysis, especially helping to determine the rate-determining step by studying the current response sensitivity to the applied potential.[10,13] Tafel slope can be calculated according to Equation 15, where i is the corresponding current density for the overpotential η and i_0 is the exchange current density. Smaller Tafel slope generally indicates the smaller internal barriers for mass and electron transport,[18] and a faster increasing rate of the current density under a smaller overpotential. So, the electrocatalyst with good activity should have small Tafel slope.

Another key parameter for an OER catalyst to be used for the industry application is the stability. The instabilities of the catalysts are usually because of the following 3 reasons. 1) Some materials were oxidized because of the highly applied potential, resulting in the passivation of the catalysts and/or the dissolving of the catalysts in the electrolyte.[19,20] 2) The electrolytes could corrode or react with the catalysts leading to the

dissolving of the catalysts.[21] 3) Some anodes were made up of the substrates like carbon and the pasted active materials. The active materials may be detached from the substrates during the long-term reaction process. The stability of a catalyst is usually evaluated by the method of chronopotentiometry or chronoamperometry. Chronopotentiometry is a technique of recording the change of potential vs testing time at a constant current. Chronoamperometry is a technique of recording the change of current vs testing time at a constant potential. For industry application, excepting for the long-term stability, the catalyst materials should be cheap and the method of catalyst preparation should be simple and easily reproducible.

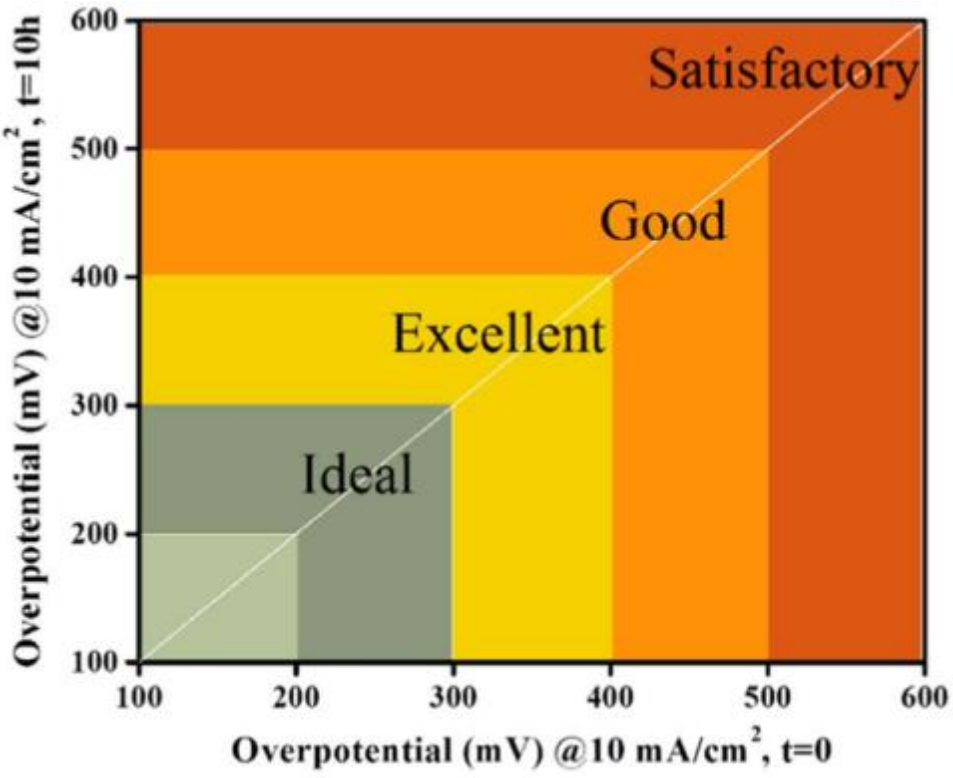

Figure 1.3 The figure of merit for OER. Reproduced with permission from Ref. 13.

In a reported review by Z. Wang *et al*,[13] OER catalysts were divided into different class according to their activity and stability, as depicted in figure 1.3. X axis was the overpotential (η_1) at the current density of 10 mA/cm^2 for the fresh catalyst, and Y axis was the overpotential (η_2) of 10 mA/cm^2 for the catalyst after 10-hour test with a constant current density of 10 mA/cm^2. Only a few catalysts were reported to have the overpotential of lower than 300 mV especially after 10-hour water electrolysis, and these catalysts are the best OER catalysts. A small part of catalysts were reported to have the overpotential which lay between 300 mV and 400 mV. If the overpotential were still lower than 400 mV after 10-hour water electrolysis, these catalysts were excellent OER catalysts. For good and satisfactory OER catalysts, the overpotential η_1 and η_2 should both lie in the range of 400-500 mV and 500-600 mV, respectively.

1.3 Oxygen evolution reaction catalysts

Nobel-metals based catalysts have been reported to exhibit excellent OER activity. Among the noble metals of palladium (Pd), iridium (Ir), platinum (Pt) and ruthenium (Ru), Ru and Ir based catalysts have better activity. With the low overpotential and Tafel slope for OER, Ru and Ir are taken as the state-of-the-art OER electrocatalysts.[13,22,23] But their durability need to be further improved. S. Cherevko and his co-authors studied the activities and stabilities of Ir, Ru, IrO_2 and RuO_2 film OER electrodes with an electrochemical scanning flow cell (SFC) connected to an inductively coupled plasma mass spectrometer (ICP-MS), and the results are shown in Figure 1.4.[21] For both alkaline and acidic electrolytes, the OER activity of Ru and Ir pure metals were better than their metal oxides, however, the durability of RuO_2 and IrO_2 were better compared with their pure metals. But RuO_2 and IrO_2 are not stable under high anodic potentials.[19,20] RuO_2 and IrO_2 will be oxidized to $(Ru^{8+})O_4$ and $(Ir^{6+})O_3$, respectively, which are not stable and will be dissolved by the electrolyte, resulting in the deterioration of the catalysts. A doped bimetallic oxide system $Ru_xIr_{1-x}O_2$ was proposed by researchers in order to improve the stability of RuO_2.[24,25] The incorporation of Ir into RuO_2 suppressed the deterioration without sacrificing much performance of OER. The core-shell structure (IrO_2 @ RuO_2) has been designed by T. Audichon *et al*,[26] and this structure showed not only the lower overpotential (~ 300 mV) but also the increasing stability (only 3.3% mass loss after 1000th cycling). Although many efforts have been done to improve the stability of Ru- and Ir-based catalysts, the dissolving of these catalysts can be only suppressed. For the industry application, their stabilities still need to be further improved. Moreover, the high price of these catalysts has restrained their widely application.

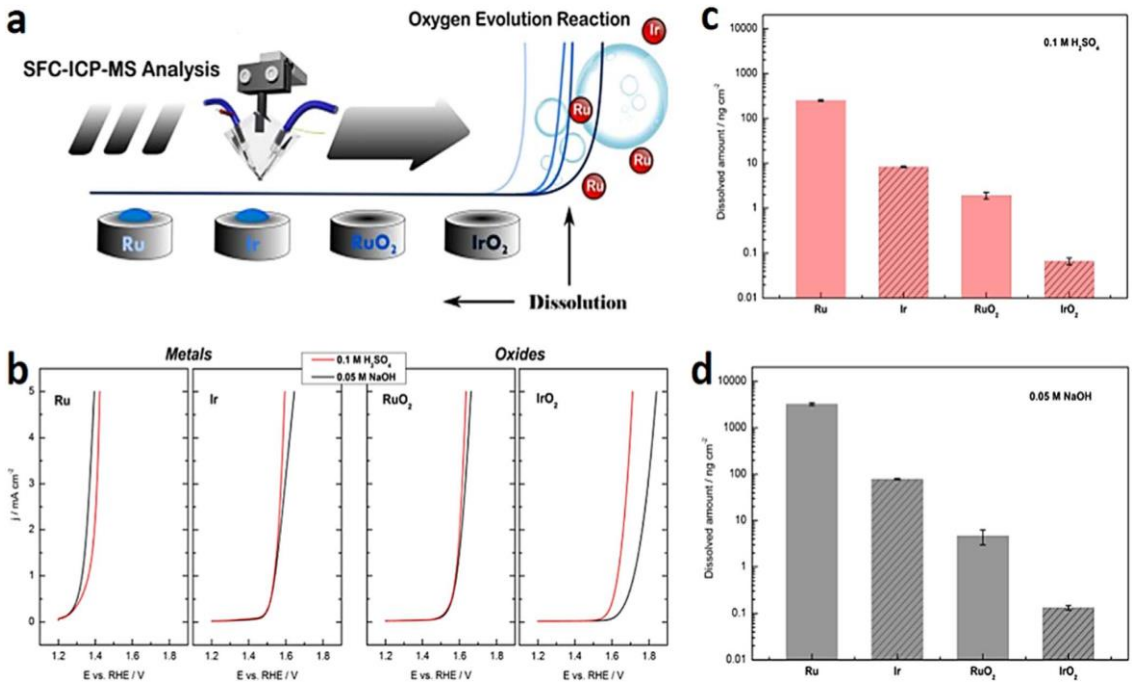

Figure 1.4 (a) OER activity and stability of Ir, Ru, IrO_2 and RuO_2. (b) I-V curves with the scan rate of 10 mV/s. (c, d) Dissolved metal from Ir, Ru, IrO_2 and RuO_2 catalysts measured during a positive potential scan at the scan rate of 10 mV/s. Reproduced with permission from Ref. 21.

Transition metal oxides, especially NiO and CoO_x, have gained a wide research interest for OER because of their high activities, good corrosion resistance and low cost. Ni-based metal oxides used for OER will be discussed in this work. Researchers have devoted great efforts to improving the OER activity of NiO by turning the particle size, increasing the surface area and changing the surface microstructure.[27] K. Fominykh and his co-authors synthesized dispersible and ultra-small crystalline NiO by a solvothermal reaction, and the solvent was tert-butanol.[28] The decreasing particle size of NiO nanoparticles brought in two merits: 1) the part oxidation of Ni^{2+} to Ni^{3+} which is

electrocatalytic active in the nickel compounds, 2) high surface area which can offer more reaction sites to improve the reaction activity. Also, the OER activity of NiO can be enhanced by the incorporation of other metals such as Co and Fe by improving the electric conductivity and increasing the exposing active sites. In order to make a fair comparison about the inherent OER activity among the benchmark catalysts, Ru-, Ir-, Ni- and Co-based electrocatalysts were synthesized using the same method of electrodeposition and same glass carbon substrate by T. F. Jaramillo and his co-authors.[12] The OER activities of $NiCeO_x$, $NiCuO_x$, $NiLaO_x$, $NiCoO_x$, $NiFeO_x$, NiO_x, $CoFeO_x$, CoPi, CoO_x and IrO_x were measured in 1 M KOH electrolyte, and the results are shown in Figure1.5. The OER activity of IrO_x was the best, but the overpotential at the current density of 10 mA/cm^2 decreased from 320 mV to 1050 mV during the 2-hour electrolysis process. Other tested samples were much stable, and had the similar overpotentials between 0.35 V and 0.43 V for 10 mA/cm^2.

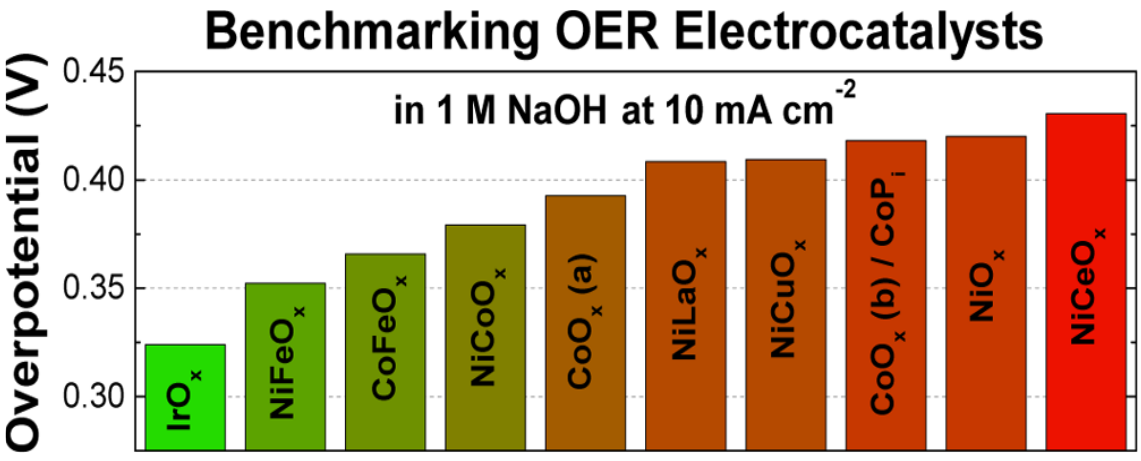

Figure 1.5 OER performance of the reported benchmark catalysts, the electrolyte is 1 M KOH. Reproduced with permission from Ref. 12.

Another effective way to improve the OER activity of Ni-based metal oxides is to

choose a suitable substrate. Carbon nanotubes and graphene are widely used substrates because of their large surface areas and high conductivity.[27,29–31] Chen and his co-authors reported that Ni/N-doped graphene had a high current density of 16.3 mA/cm^2 with the overpotential of 400 mV.[29] The 3D Ni/N-doped graphene catalyst was synthesized through a heterogeneous reaction process followed by liquid-phase doping. Nickle foam (NF) is also considered as an ideal substrate because of the following reasons: 1) high electronic conductivity and high surface area, 2) in situ generated OER catalyst, 2) low cost. Wang and his co-authors synthesized a 3D OER catalyst (NF/PC/AN) consisted of anodized Ni, porous carbon and Ni foam substrate. The porous carbon membrane mid-layer on one hand protected the unstable Ni foam substrate, on the other hand was as the support for the anodized Ni. The anodized Ni (AN) acted as the OER active species. The combination of the high electronic conductive Ni foam and OER active anodize Ni resulted in good OER activity. Moreover, the stable porous carbon enhanced the stability of the catalyst.

Ni-based metal oxides are the good candidates of noble metal oxides as the oxygen evolution reaction catalysts because of their good activities and low cost. However, their OER activity and stability are needed to be further improved. Using a substrate with large surface area and good conductivity is able to greatly improve the activity and stability of a catalyst. But the synthesis methods are usually complicated and cost much. It is an urgent thing to enhance the OER activity and stability of Ni-based catalysts and reduce the cost at the same time for industry application.

1.4 Role of defects in electrocatalyst for oxygen evolution reaction

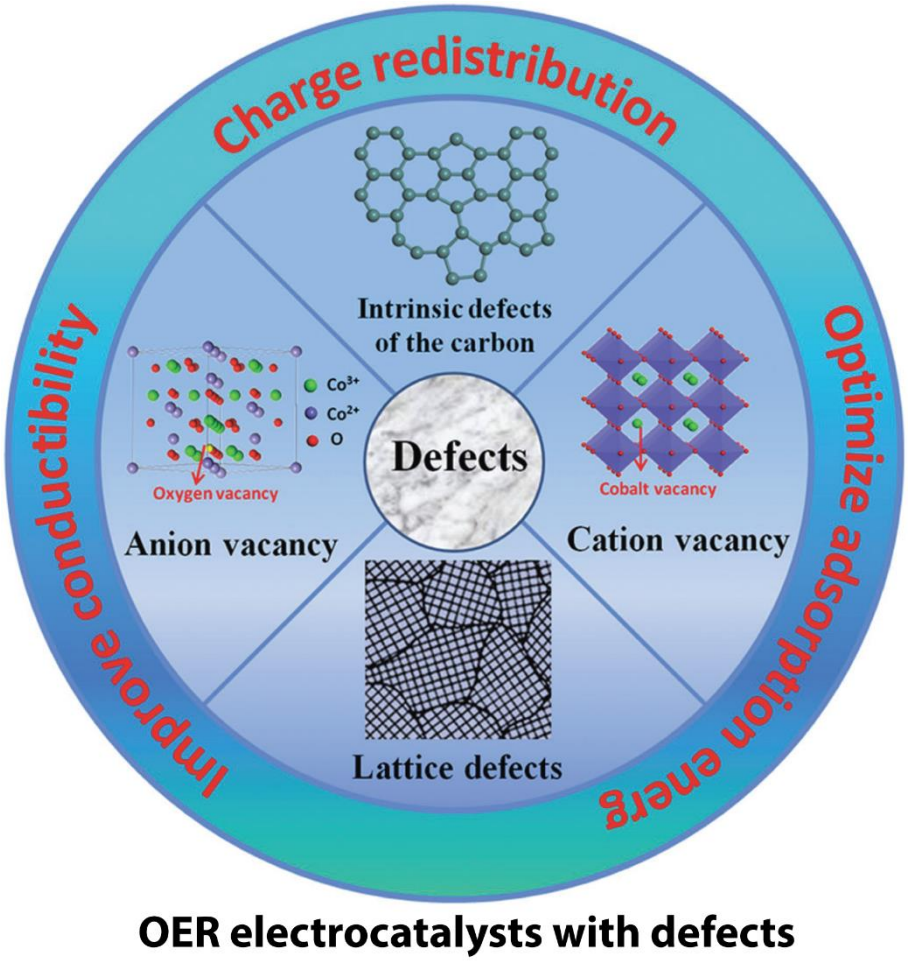

Figure 1.6 Scheme showing various defects and their positive effects on the electrocatalysts. Reproduced with permission from Ref. 8.

Recently, defects have been reported to be able to improve the OER activity of the catalysts by some groups.[8,32–34] The defects exist widely in nanomaterials, which can change their surface and electronic properties. As shown in figure 1.6,[8] different kinds of defects have been found in the materials, which include the intrinsic defects of the carbon, cation vacancy such as cobalt vacancy formed in the cobalt oxide, lattice defects and

anion vacancy. These defects can improve the OER activities of the catalysts by the following three aspects: 1) affecting the charge redistribution in the catalyst; 2) optimizing the adsorption energy for the reactants in oxygen evolution reaction; 3) improving the conductivity of the catalysts.

Oxygen vacancy defects are considered as the most popular anion vacancy defects in transition-metal oxide catalysts because of their low formation energy. Wang and his co-authors synthesized the Co_3O_4 nanosheets with rich oxygen vacancy defects by a plasma-engraving strategy.[34] When applied as the electrode for OER, the oxygen vacancy defects-rich Co_3O_4 nanosheets showed a low overpotential of 1.53 V vs RHE (reversible hydrogen electrode) for the current density of 10 mA/cm^2, while the overpotential for the pristine Co_3O_4 nanosheets was 1.77 V vs RHE. The highly enhanced OER activity of plasma-engaged Co_3O_4 nanosheets is due to the improved conductivity, resulting from the changed electronic properties adjusted by the formed oxygen vacancy defects.

Amorphous catalysts, compared with crystals, have a large number of active sites for OER because of the commonly existed crystal defects in them. Yang and his co-authors synthesized the nanoporous Ni-Co binary oxide layers with amorphous structure through deposition process followed by anodization.[32] This catalyst showed a large electrochemically active surface area (roughness factor up to 17) and low overpotential (ca. 325 mV) for achieving the current density of 10 mA/cm^2. The enhanced OER performance of nanoporous Ni-Co binary oxide layers was from the active sites offered by the large number of surface defects and lattice dislocations in the amorphous structure. Nai and his co-authors synthesized the Ni-Co double hydroxides nanocages with amorphous structure by using Cu_2O nanocrystals as the templates.[33] The good performance of the Ni-Co ADHs nanocages was partly from the amorphous structure. The

abundant under-coordinated metal atoms in the amorphous materials provide rich surface reactive sites, thus facilitating the binding for the adsorbate species such as hydroxyls for OER. Also, the mechanically flexible property of the amorphous structure is helpful to enhance the long-term stability of the OER electrocatalysts.

1.5 Defects in Ce-based catalysts

Cerium belongs to the rare earth family and is more abundant than other rare earth elements in the earth. It has two common oxidation states of Ce^{3+} and Ce^{4+}, which is the key factor for the catalytic activity of Ce-based catalysts. The easily shift between Ce^{3+} and Ce^{4+} results in the ability of oxygen storage and release of CeO_2. This property of CeO_2 is usually characterization by the technique of the "oxygen storage capacity" (OSC) and is related to the concentration of oxygen vacancy defects in CeO_2. Under oxygen-poor conditions, Ce^{4+} in cerium oxide will be partly reduced to Ce^{3+} because of the loss of oxygen. Under oxygen-rich conditions, the reduced Ce (Ce^{3+}) can be oxidized to Ce^{4+} by the supplied oxygen. The easier transformation between Ce^{3+} and Ce^{4+} will bring in the high OSC ability of cerium oxide. The increase in Ce^{3+} fraction in cerium oxide is expected with an increase of oxygen vacancy defects in order to maintain the electronic balance, as shown in Equation 16.[35] The generated oxygen vacancy defects with high mobility can improve the ionic conductivity, and contribute to the transfer of oxygen ion used in the solid solutions.[36]

$$4Ce^{4+} + O^{2-} \rightarrow 4Ce^{4+} + 2e^{-}/\square + 0.5O_2 \rightarrow 2Ce^{4+} + 2Ce^{3+} + \square + 0.5O_2 \quad (16)$$

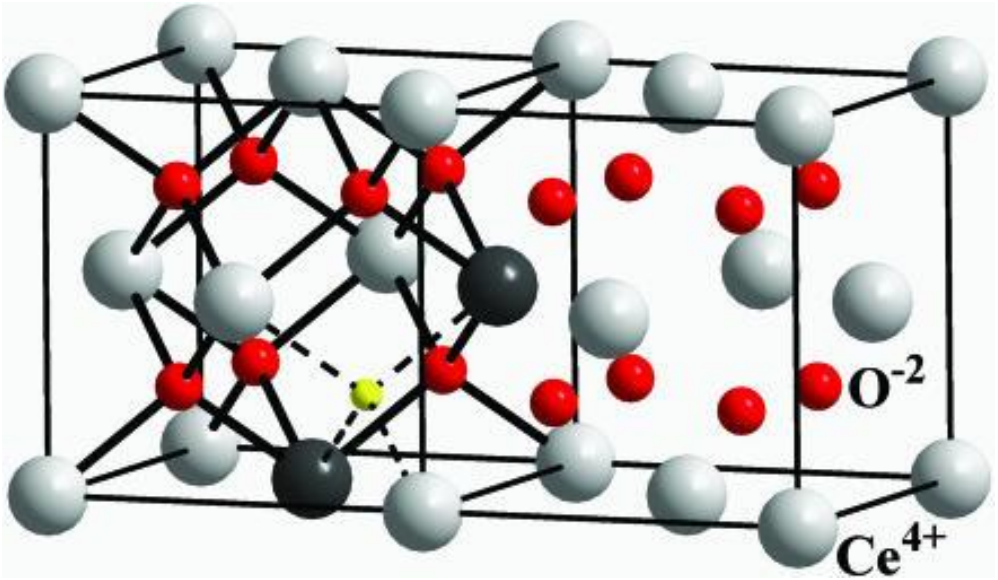

Figure 1.7 The crystal structure of doped CeO_2 (left cube) and undoped CeO_2 (right cube). The dark spheres stand for the trivalent lanthanide ions, and the small yellow sphere stand for the oxygen vacancy. Reproduced with permission from Ref. 37.

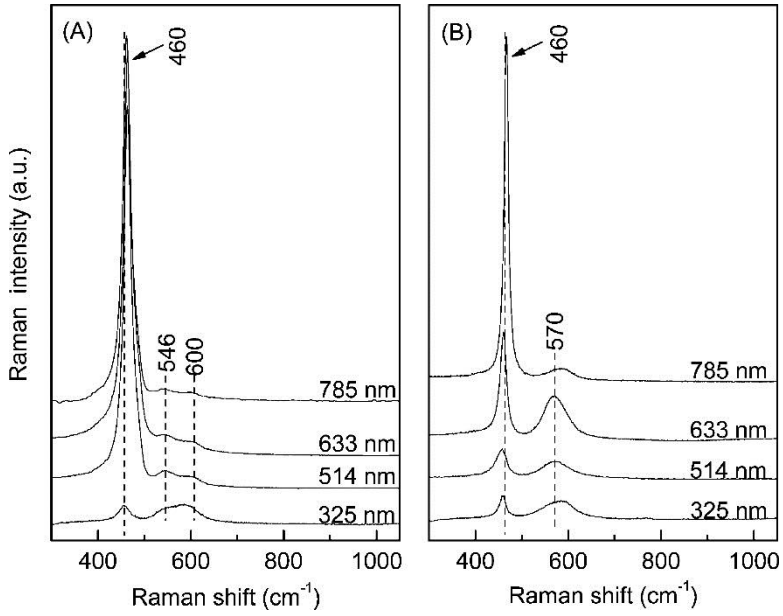

Figure 1.8 Raman spectra of (A) Sm- and (B) Pr-doped ceria with different excitation lasers of 785, 633, 514 and 325 nm. Reproduced with permission from Ref. 38.

Because of the easily shift between Ce^{3+} and Ce^{4+}, defects such as oxygen vacancies are generated in the lattice of CeO_2 by loss of oxygen and/or its electros. The oxidation states of cerium and the defect structure of CeO_2 are related and can be affected by changing the physical parameters. The physical parameters include the oxygen partial pressure,[39] temperature,[40] doped by other elements,[38,41] an electrical field[42] and surface stress.[43] The crystal structures of doped CeO_2 (left) and undoped CeO_2 (right) are shown in Figure 1.7.[37] For the doped CeO_2, two cerium ions (red spheres) were replaced by trivalent lanthanide ions (dark spheres) resulting in the formation of oxygen vacancy defect (yellow sphere). For the undoped CeO_2, no oxygen vacancy defects were detected. Guo and his co-authors studied the oxygen vacancies in a series of rare-earth doped ceria by visible (785, 633 and 514 nm) and UV (325 nm) Raman spectroscopy. According to the intensity of the observed F_{2g} peaks (460 cm^{-1}), the obtained information was mainly from the surface of the sample by using UV Raman spectroscopy. When increasing the wavelength of the excitation laser (from UV to visible region), the detect depth of the sample was increased and the mainly obtained information changed to from the bulk. The Raman spectra of Sm-doped ceria at 785, 633, 514 and 325 nm excitation laser lines are shown in Figure 1.8a. The peak at ca. 460 cm^{-1} was related to the fluorite structure of CeO_2. The peak at ca. 546 cm^{-1} was associated with the oxygen vacancies introduced into the doped CeO_2 for maintaining the charge neutrality because of the Ce^{4+} ions replaced by the ions with lower oxidation states. The peak at ca. 600 cm^{-1} was associated with the intrinsic oxygen vacancies resulting from the presence of Ce^{3+} in CeO_2 nanopowder. From the relative peak areas, the obtained oxygen vacancies introduced by ion doping were proved to be distributed in the lattice of CeO_2. For Pr-doped CeO_2, as shown in Figure 1.8b, only a broad peak centered at ca. 600 cm^{-1} associated oxygen vacancies was

observed.

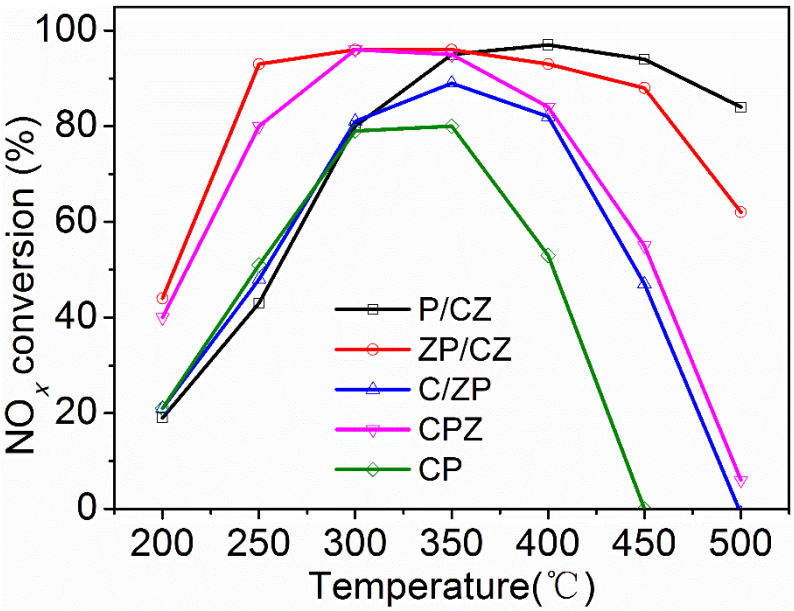

Figure 1.9 NH_3-SCR activities of the catalysts: NO_x conversions with the function of reaction temperatures. Reproduced with permission from Ref. 44.

Because of these good advantages including the easily formed oxygen vacancy defects, Ce-based catalysts have been widely used for thermal catalytic reactions such as the selective catalytic reduction of NO_x and the CO oxidation reaction. [44–47] A series of Ce-based catalysts have been reported to be used for the selective catalytic reduction (SCR) of NO_x by Yu and his co-authors, as shown in Figure 1.9.[44] The zirconium phosphate @ $Ce_{0.75}Zr_{0.25}O_2$ (ZP/CZ) catalyst showed the highest NO_x conversion at low temperatures (below 300 °C). The reason was that the plenty of oxygen vacancies in ZP/CZ facilitated the electron and/or oxygen transfer, resulting the improved activity.

The research goal for this thesis is about the synthesis of a noble-metal free water electrolysis catalyst with high activity and long-term stability in a simple method. Ni-based catalysts are considered as the good candidates for noble-metal catalysts because

of its low cost and high activity for oxygen evolution reaction (OER). However, the OER activities of Ni-based catalysts need be further improved when compared with precious metal catalysts. The stability of Ni-based catalysts are also needed to be enhanced so that the long-term performance of the catalysts can meet the requirement for industry application. The OER activity of a catalyst can be enhanced by introducing defects into the catalyst. Ce-based catalysts with easily formed oxygen vacancy defects have been widely used for thermal catalysis reactions. Cerium oxide is very stable in strong alkaline solution such as KOH solution. Therefore, we have designed Ni doped cerium oxide ($NiCeO_x$) catalyst to combine the advantages of Ni- and Ce- based catalysts and applied for water electrolysis in KOH electrolyte.

References

1 I. . Dresselhaus, M.S.; Thomas, *Nature*, 2001, **414**, 332–337.

2 X. Zou and Y. Zhang, *Chem. Soc. Rev.*, 2015, **44**, 5148–5180.

3 E. E. Benson, C. P. Kubiak, A. J. Sathrum and J. M. Smieja, *Chem. Soc. Rev.*, 2009, **38**, 89–99.

4 T. R. Cook, D. K. Dogutan, S. Y. Reece, Y. Surendranath, T. S. Teets and D. G. Nocera, *Chem. Rev.*, 2010, **110**, 6474–6502.

5 J. A. Turner, *Science (80-.).*, 2017, **305**, 972–975.

6 E. Zoulias and E. Varkaraki, *Tcjst*, 2004, **4**, 41–71.

7 K. Zeng and D. Zhang, *Prog. Energy Combust. Sci.*, 2010, **36**, 307–326.

8 D. Yan, Y. Li, J. Huo, R. Chen, L. Dai and S. Wang, *Adv. Mater.*, 2017, **29**, 1606459.

9 I. C. Man, H. Y. Su, F. Calle-Vallejo, H. A. Hansen, J. I. Martínez, N. G. Inoglu, J. Kitchin, T. F. Jaramillo, J. K. Nørskov and J. Rossmeisl, *ChemCatChem*, 2011, **3**, 1159–1165.

10 N.-T. Suen, S.-F. Hung, Q. Quan, N. Zhang, Y.-J. Xu and H. M. Chen, *Chem. Soc. Rev.*, 2017, **46**, 337–365.

11 R. Frydendal, E. A. Paoli, B. P. Knudsen, B. Wickman, P. Malacrida, I. E. L. Stephens and I. Chorkendorff, *ChemElectroChem*, 2014, **1**, 2075–2081.

12 C. C. L. McCrory, S. Jung, J. C. Peters and T. F. Jaramillo, *J. Am. Chem. Soc.*, 2013, **135**, 16977–16987.

13 M. Tahir, L. Pan, F. Idrees, X. Zhang, L. Wang, J. J. Zou and Z. L. Wang, *Nano Energy*, 2017, **37**, 136–157.

14 J. B. Allen and A. J. Bard, 1980.

15 S. Trasatti and O. A. Petrii, *Pure Appl. Chem.*, 1991, **63**, 711–734.

16 J. D. Benck, Z. Chen, L. Y. Kuritzky, A. J. Forman and T. F. Jaramillo, *ACS Catal.*, 2012, **2**, 1916–1923.

17 Y. Q. Gao, H. B. Li and G. W. Yang, *J. Appl. Phys.*, 2016, **119**, 034902.

18 J. Yu, Q. Cao, B. Feng, C. Li, J. Liu, J. K. Clark and J. Delaunay, 2018, **1**, 1–10.

19 R. Kötz, *J. Electrochem. Soc.*, 1984, **131**, 72.

20 R. Kötz, *J. Electrochem. Soc.*, 1983, **130**, 825.

21 S. Cherevko, S. Geiger, O. Kasian, N. Kulyk, J. P. Grote, A. Savan, B. R. Shrestha, S. Merzlikin, B. Breitbach, A. Ludwig and K. J. J. Mayrhofer, *Catal. Today*, 2016, **262**, 170–180.

22 T. Reier, M. Oezaslan and P. Strasser, *ACS Catal.*, 2012, **2**, 1765–1772.

23 Y. Jiao, Y. Zheng, M. Jaroniec and S. Z. Qiao, *Chem. Soc. Rev.*, 2015, **44**, 2060–2086.

24 E. Mayousse, F. Maillard, F. Fouda-Onana, O. Sicardy and N. Guillet, *Int. J. Hydrogen Energy*, 2011, **36**, 10474–10481.

25 L. E. Owe, M. Tsypkin, K. S. Wallwork, R. G. Haverkamp and S. Sunde, *Electrochim. Acta*, 2012, **70**, 158–164.

26 T. Audichon, T. W. Napporn, C. Canaff, C. Morais, C. Comminges and K. B. Kokoh, *J. Phys. Chem. C*, 2016, **120**, 2562–2573.

27 L. Han, S. Dong and E. Wang, *Adv. Mater.*, 2016, **28**, 9266–9291.

28 K. Fominykh, J. M. Feckl, J. Sicklinger, M. Döblinger, S. Böcklein, J. Ziegler, L. Peter, J. Rathousky, E. W. Scheidt, T. Bein and D. Fattakhova-Rohlfing, *Adv. Funct. Mater.*, 2014, **24**, 3123–3129.

29 S. Chen, J. Duan, J. Ran, M. Jaroniec and S. Z. Qiao, *Energy Environ. Sci.*, 2013, **6**, 3693.

30 X. Yu, T. Hua, X. Liu, Z. Yan, P. Xu and P. Du, *ACS Appl. Mater. Interfaces*, 2014, **6**, 15395–15402.

31 V. M. Dhavale, S. S. Gaikwad, L. George, R. N. Devi and S. Kurungot, *Nanoscale*, 2014, **6**, 13179–13187.

32 Y. Yang, H. Fei, G. Ruan, C. Xiang and J. M. Tour, *ACS Nano*, 2014, **8**, 9518–9523.

33 J. Nai, H. Yin, T. You, L. Zheng, J. Zhang, P. Wang, Z. Jin, Y. Tian, J. Liu, Z. Tang and L. Guo, *Adv. Energy Mater.*, 2015, **5**, 1401880.

34 L. Xu, Q. Jiang, Z. Xiao, X. Li, J. Huo, S. Wang and L. Dai, *Angew. Chemie*, 2016, **128**, 5363–5367.

35 X. Liu, K. Zhou, L. Wang, B. Wang and Y. Li, *J. Am. Chem. Soc.*, 2009, **131**, 3140–3141.

36 C. Sun, H. Li and L. Chen, *Energy Environ. Sci.*, 2012, **5**, 8475.

37 K. Schwarz, *Proc. Natl. Acad. Sci. U. S. A.*, 2006, **103**, 3497.

38 M. Guo, J. Lu, Y. Wu, Y. Wang and M. Luo, *Langmuir*, 2011, **27**, 3872–3877.

39 J. Yu, Z. Si, X. Li, L. Chen, X. Wu and D. Weng, *Catal. Today*, 2016, **267**, 47–55.

40 G. S. Herman, *Surf. Sci.*, 1999, **437**, 207–214.

41 A. Nakajima, A. Yoshihara and M. Ishigame, *Phys. Rev. B*, 1994, **50**, 13297–13307.

42 P. Gao, Z. Wang, W. Fu, Z. Liao, K. Liu, W. Wang, X. Bai and E. Wang, *Micron*, 2010, **41**, 301–305.

43 P. Gao, Z. Kang, W. Fu, W. Wang, X. Bai and E. Wang, *J. Am. Chem. Soc.*, 2010, **132**, 4197–4201.

44 J. Yu, Z. Si, L. Chen, X. Wu and D. Weng, *Appl. Catal. B Environ.*, 2015, **163**, 223–232.

45 Q. Fu, H. Saltsburg and M. Flytzani-Stephanopoulos, *Science (80-.).*, 2003, **301**, 935–938.

46 F. Esch, S. Fabris and L. Zhou, *Science (80-.).*, 2005, **309**, 752–755.

47 L. Chen, P. Fleming, V. Morris, J. D. Holmes and M. A. Morris, *J. Phys. Chem. C*, 2010, **114**, 12909–12919.

2. Synthesis of $Ni_yCe_{100-y}O_x$ catalysts by Ni/Ce mixed solution for oxygen evolution reaction

2.1 Introduction

For society to adapt to the growing demand for clean energy, renewable energy sources must be utilized to a greater degree. Unfortunately, the vast majority of renewable energy sources, such as wind and solar energy sources, can only produce energy intermittently.[1,2] For these renewable energy sources to replace conventional fossil fuel energy sources, energy storage technologies must be improved.[3,4] A wide variety of energy conversion devices, including hydrogen fuel-cells, photoelectrochemical cells and metal-air batteries, have been explored to convert electrical or solar energy to chemical energy in order to store the energy produced by renewable energy sources. In all of these devices, the oxygen evolution reaction (OER) is a critical reaction.[5–10] Because the OER is a four-electron reaction, it has a large activation barrier, and a large overpotential is needed to drive the electrochemical reaction.[11,12] Finding a suitable OER catalyst with a high efficiency, low overpotential, low-cost and long-term stability is key to enabling widespread adoption of renewable energy sources.

The best OER catalysts reported so far have generally been iridium or ruthenium-based oxides. The scarcity of both iridium and ruthenium, however, significantly limits the widespread use of these catalysts.[13,14] First-row transition metals such as Ni- and Co-based oxides, have recently been studied as low-cost alternatives to iridium and ruthenium-based oxide catalysts.[14–18] Ni- and Co-based mixed oxides such as $NiFeO_x$, $NiCoO_x$ and $NiCeO_x$ have been studied as the benchmarking OER electrocatalysts.[15] For

the current density of 10 mA/cm^2, $NiFeO_x$ was shown to have the lowest overpotential of 350 mV, and $NiCeO_x$ with the highest overpotential of 430 mV.[15] Both of these are higher than the 320 mV overpotential of IrO_x.[15] In order to improve the activity of $NiCeO_x$, the Au mid-layer was added. The overpotential of this $NiCeO_x$-Au material was decreased to 280 mV. During a 2-hour stability test, however, the overpotential of $NiCeO_x$-Au increased with the testing time and end up with 310 mV.[19] It is therefore needed to design and synthesize a noble metal free Ni- or Co- based catalyst with a low overpotential and long-time stability.

Defects in catalysts can enhance the OER performance of the catalysts by altering the local electron density distribution in the vicinity of the defects and providing catalytically active sites.[20–22] Ceria is an example of a non-stoichiometric catalyst material that exhibits a higher catalytic activity when defects are introduced into it. The enhancement of the catalytic activity of Ceria by defects has been demonstrated for the selective catalytic reduction of NO_x and the CO oxidation reaction.[23–26] These reactions, however, usually occur at high temperature, and whether or not defects in ceria and ceria based catalysts can enhance catalytic activity in low temperature reactions, such as water electrolysis, has yet to be discerned. Nickel foam (NF) was reported to be a good substrate for OER because of its large surface area and high electronic conductivity.[17,27,28]

In this work, a series of $Ni_yCe_{100-y}O_x$ with different Ni/Ce ratio were synthesized on NF/NiO substrate with simple dip-coating and annealing methods. The surface NiO obtained from the oxidation of NF can prohibit the diffusion of Ni atoms to the deposited $Ni_yCe_{100-y}O_x$ so that the Ni/Ce ratio will be remained. Oxygen vacancy defects are formed successfully in all the NF/NiO/$Ni_yCe_{100-y}O_x$ (simply referred to $Ni_yCe_{100-y}O_x$) catalysts. The concentration of oxygen vacancy defects for $Ni_{75}Ce_{25}O_x$ and $Ni_{50}Ce_{50}O_x$ catalysts are

larger than other $Ni_yCe_{100-y}O_x$ catalysts, resulting in a similar larger electrochemically active surface area and a same lower Tafel slope of 66 mV/decade. The overpotential for $Ni_{75}Ce_{25}O_x$ and $Ni_{50}Ce_{50}O_x$ catalysts are 338 mV and 341 mV to obtain a current density of 10 mA/cm^2 that are lower than other $Ni_yCe_{100-y}O_x$ catalysts. With a fixed current density of 10 mA/cm^2, the $Ni_{75}Ce_{25}O_x$ catalyst exhibits an ultra-high stability of over 100 h, while the $Ni_{95}Ce_5O_x$ catalyst is not stable during 25-hour water electrolysis process.

2.2 Experimental Section

2.2.1 Synthesis of $Ni_yCe_{100-y}O_x$ catalysts on Ni foam/NiO substrate

The synthesis of NF/NiO/$Ni_yCe_{100-y}O_x$ catalysts. The first step was to prepare the NiO substrate. A 10 x 15 mm^2 Nickel Foam (NF, >99.99%, MTI Corporation) substrate with a thickness of 0.08 mm was firstly cleaned by acetone (99%, Wako) in an ultrasonic bath for 5 min. Then the NF was rinsed by deionized water for three times. Subsequently, the NF was dried in air, and annealed for 2 h with a heating rate of 2 °C/min at 400 °C in a muffle furnace. The second step is to prepare the nickel and cerium mixed precursor solution. The precursor solution was prepared by dissolving 0.3 M citric acid and 0.15 M metal ions in 20 ml ethanol. The molar ratio of Ni and Ce ions were 95:5, 90:10, 75:25, 50:50, 25:75, and 10:90 for the catalysts of $Ni_{95}Ce_5O_x$, $Ni_{90}Ce_{10}O_x$, $Ni_{75}Ce_{25}O_x$, $Ni_{50}Ce_{50}O_x$, $Ni_{25}Ce_{75}O_x$ and $Ni_{10}Ce_{90}O_x$, respectively. $Ce(NO_3)_3 \cdot 6H_2O$ offers the Ce ions and $Ni(NO_3)_2 \cdot 6H_2O$ offers the Ni ions. The final step is the preparation of NF/NiO/$Ni_yCe_{100-y}O_x$ catalysts. The prepared precursor solution was deposited onto NiO by dip coating and then annealed in the same manner as the NiO substrate.

2.2.2 Structural characterization

A field emission Scanning electron microscope (SEM, JEOL JSM 7600 FA) was used for the measurements of SEM. A diffractometer (Rigaku Co. Ltd, SmartLab, Japan) with Cu Kα radiation (dwelling time = 2 s, incident angle = 0.5°, step size = 0.02°, λ = 1.541 Å) was used for the colleting of grazing incidence X-ray diffraction data. A Renishaw inVia Raman Microscope system was used to acquire the Raman spectra at room temperature. A ×100 objective and a 532 nm excitation laser were used. A PHI 5000

VersaProbe (ULVAC-PHI) with an Al Kα X-ray source (1486.6 eV) was used to obtain the X-ray photoelectron spectroscopy (XPS). The pass energies of 117.4 eV and 23.5 eV were used for the electron analyzer to analyze the wide scans and narrow scans, respectively.

2.2.3 Electrochemical measurements

A cylindrical glass cell with a standard three-electrode configuration was used for the electrochemical measurements. A Pt wire and a Ag/AgCl electrode were used as the counter electrode and the reference electrode, respectively. The working electrode was NF/NiO/$Ni_yCe_{100-y}O_x$, hereafter simply referred to as the $Ni_yCe_{100-y}O_x$ electrode. A potentiostat (Princeton Applied Research, VersaSTAT 4) was used to perform the electrochemical measurements. The potentials were calibrated against the RHE according to the following equation: ($E_{RHE} = E_{Ag/AgCl} + 0.059\ pH + E^0_{Ag/AgCl}$), where $E_{Ag/AgCl}$ is the potential difference measured between the Ag/AgCl electrode and the working electrode, $E^0_{Ag/AgCl}$ (0.1976 V at 25 °C) is the standard electrode potential for a Ag/AgCl electrode, pH is the pH of the electrolyte solution, and E_{RHE} is the calibrated potential. The electrolytes used were saturated with oxygen before and during the OER experiments.

The polarization curves were collected through linear sweep voltammetry (LSV), and the scan rate was 10 mV/s. Controlled-current water electrolysis was performed using a chronopotentiometric technique.[15] The solution resistance R_s (~ 2 Ω), determined using the electrochemical impedance spectroscopy (EIS) technique,[15] was used to correcte the *iR* drop across the solution. Unless otherwise stated, all given potentials are vs RHE and corrected for the *iR* drop across the electrolyte. Tafel plots obtained from the steady-state polarization curves with a scan rate of 1 mV/s. Cyclic voltammetry (CV) was used to

determine the electrochemical capacitance of the samples presented in this paper.[15,29] The potential was swept in a range from 0.05 V above the open-circuit potential (OCP) to 0.05V below the OCP in a static solution with five different scan rates: 0.005, 0.01, 0.025, 0.05 and 0.1 V s^{-1}. The working electrode was held for 10 s at each end of the potential sweep before continuing to the next sweep. All experiments were performed at room temperature.

2.3 Results and Discussion

2.3.1 Morphologies of $Ni_yCe_{100-y}O_x$ catalysts

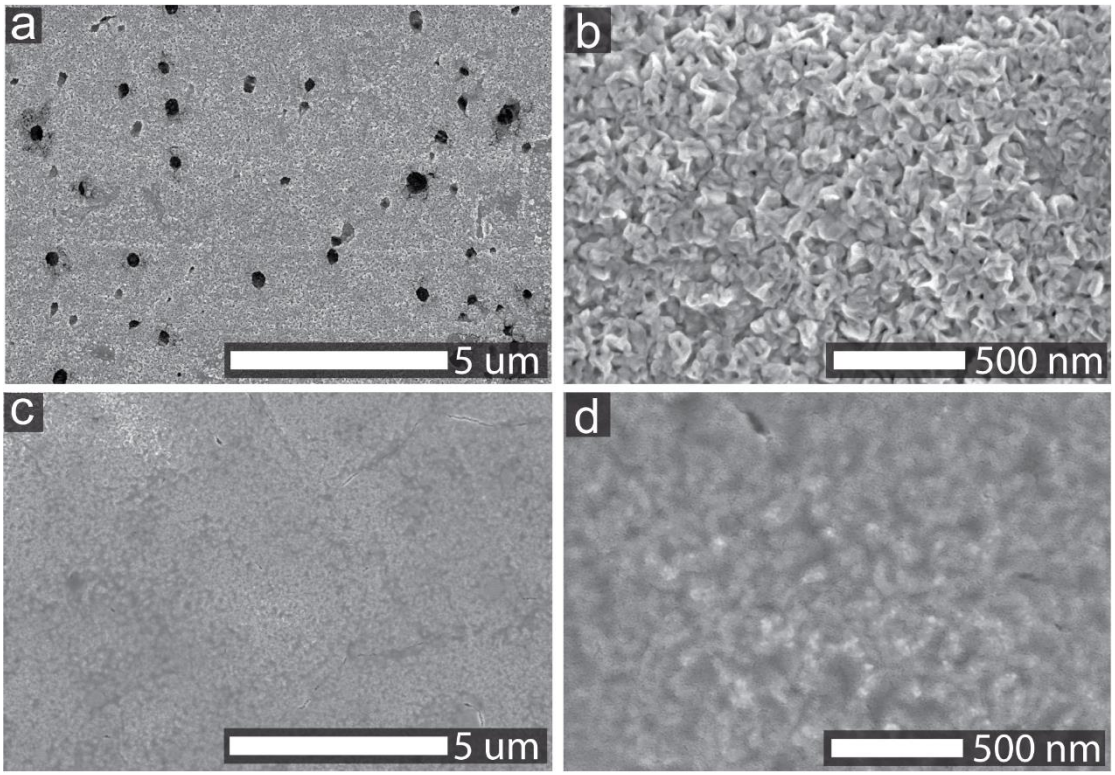

Figure 2.1 SEM images of NiO (a-b) and $Ni_{95}Ce_5O_x$ (c-d) samples.

Holes with sizes varying from several nanometers to a few hundred nanometers were observed on the surface of NiO, as shown in Figure 2.1a. NiO sample was prepared by annealing Ni substrate in the muffle furnace for 2 hours with the elevating rate of 2 °C/min, and these holes were from the Ni foam substrate. The surface of NiO consisted of small nanocrystals, as shown in Figure 2.1b. The $Ni_yCe_{100-y}O_x$ samples were synthesized by depositing nickel and cerium mixed precursor solutions with different Ni/Ce ratio on NiO and then annealing the samples in air. The deposited layer covers the surface of NiO nanocrystals for the $Ni_{95}Ce_5O_x$ sample, as shown in Figure 2.1c and Figure 2.1d. Other

$Ni_yCe_{100-y}O_x$ catalysts have the similar morphologies.

2.3.2 Structure characterization of $Ni_yCe_{100-y}O_x$ catalysts

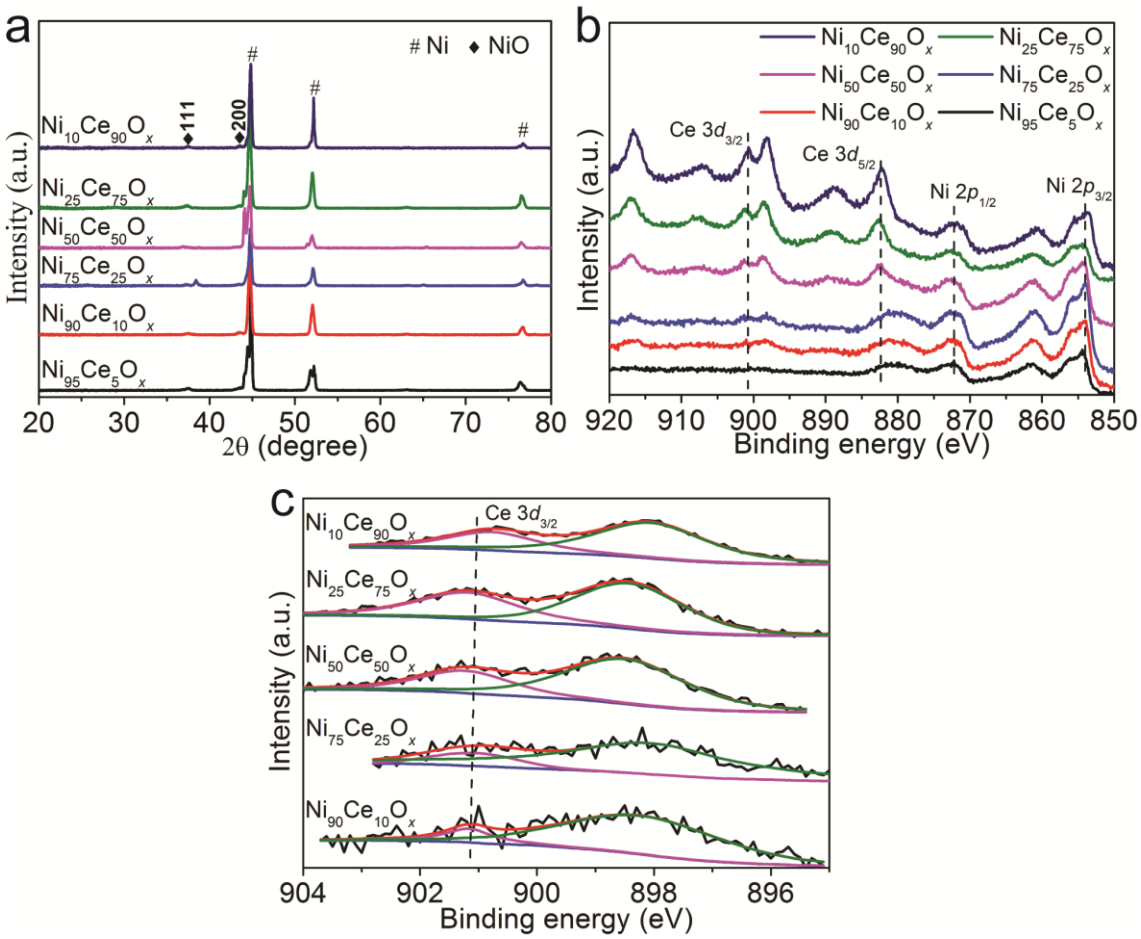

Figure 2.2 (a) X-ray diffraction patterns and (b-c) XPS spectra of $Ni_yCe_{100-y}O_x$ samples.

XRD measurements were performed to examine the crystal structure of the $Ni_yCe_{100-y}O_x$ samples, and the results are shown in Figure 2.2a. Only peaks associated with Ni and NiO were found and no peaks for CeO_2 were detected for $Ni_yCe_{100-y}O_x$ samples. It indicates that Ni and Ce mixed uniformly in the top layer and formed an amorphous structure. The surface element information of the $Ni_yCe_{100-y}O_x$ samples was further

analyzed by XPS. As shown in Figure 2.2b, Ce 3d peaks of CeO_2 and Ni 2p peaks of NiO were observed and indicates that the deposited layers of $Ni_yCe_{100-y}O_x$ catalysts are indeed composed of Ni and Ce mixed oxides. The curve fitting results of Ce $3d_{3/2}$ for $Ni_yCe_{100-y}O_x$ samples are shown in Figure 2.2c. The peak areas of Ce $3d_{3/2}$ for $Ni_{90}Ce_{10}O_x$, $Ni_{75}Ce_{25}O_x$, $Ni_{50}Ce_{50}O_x$, $Ni_{25}Ce_{75}O_x$ and $Ni_{10}Ce_{90}O_x$ samples are 31.7, 55.7, 206.2, 433.0 and 603.3. For $Ni_yCe_{100-y}O_x$ samples, the peak areas of Ce $3d_{3/2}$ are in proportion with the Ce content, and the higher Ce content of the sample, the peak areas of Ce $3d_{3/2}$ will be larger. The sequence of the peak areas of Ce $3d_{3/2}$ of $Ni_yCe_{100-y}O_x$ samples are in accordance with the Ce content in these samples. This indicates that the designed Ni/Ce ratios remain constant for the synthesized $Ni_yCe_{100-y}O_x$ samples.

2.3.3 Formation of defects in $Ni_yCe_{100-y}O_x$ catalysts

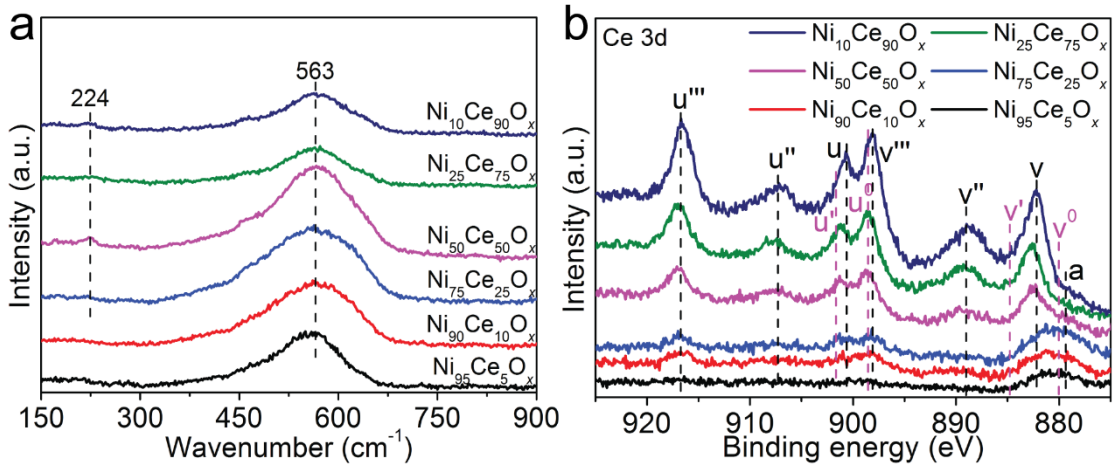

Figure 2.3 (a) Raman spectra and (b) XPS spectra of $Ni_yCe_{100-y}O_x$ samples. The peak labeled *a* in the XPS spectra is ascribed to the Ni 2p peak.

Two Raman peaks of 224 cm^{-1} and 563 cm^{-1} were observed for $Ni_{75}Ce_{25}O_x$, $Ni_{50}Ce_{50}O_x$, $Ni_{25}Ce_{75}O_x$ and $Ni_{10}Ce_{90}O_x$ samples, as shown in Figure 2.3a. For $Ni_{95}Ce_5O_x$

and $Ni_{90}Ce_{10}O_x$ samples, only the peak of 563 cm^{-1} was observed. Crystalline CeO_2 is known to have a strong F_{2g} Raman peak at 464 cm^{-1} related to its fluorite structure.[30] The presence of ions with the oxidation states lower than Ce^{4+} in the CeO_2 has been shown to induce a Raman band, known as the D band, from 500 to 700 cm^{-1}.[30–32] This band is associated with the presence of oxygen vacancy defects created in the non-stoichimometric CeO_{2-y} by the 3+ coordinated ions. In addition to the introduction of the D band, the F_{2g} band will be weakened and becomes asymmetric and broad.[33] In the Raman spectra of the $Ni_yCe_{100-y}O_x$ samples, there is no F_{2g} band, which suggests that there is no crystalline CeO_2 with a fluorite structure in these samples.[34] The broad peak at 563 cm^{-1} (D band) indicates the formation of oxygen vacancy defects. The oxygen vacancy defects should be related to the presence of Ce^{3+} because of the incorporation of Ni into CeO_2, as suggested by the literature[30,31,34]. Furthermore, the amorphous structure of $Ni_yCe_{100-y}O_x$ contributes to the broadness of the peak.[33,34] According to the areas of this peak among different $Ni_yCe_{100-y}O_x$ samples, we can roughly estimate the concentration of oxygen vacancy defects in these catalysts. The peak areas of 563 cm^{-1} for $Ni_{75}Ce_{25}O_x$ and $Ni_{50}Ce_{50}O_x$ samples are similar and larger than that of other $Ni_yCe_{100-y}O_x$ samples, suggesting that these two catalysts own larger concentration of oxygen vacancy defects. The peak at 224 cm^{-1} is related to Ce-OH vibrations which result from surface defects. Different types of hydroxyl groups generated by the dissociation of surface adsorbed water and doubly bridging hydroxyl groups on reduced cerium oxide are detected in the Raman spectra.[35,36]

XPS was carried out on $Ni_yCe_{100-y}O_x$ samples to further analyze the oxygen vacancy defects. The Ce 3d peaks of CeO_2 were observed for $Ni_yCe_{100-y}O_x$ samples, as shown in Figure 2.3b. The Ce 3d band is composed of ten individual peaks, that are labeled on

Figure 2.3b as *v*, *v''*, *v'''*, *u*, *u''*, *u'''*, v^0, *v'*, u^0 and *u'*. The *v*, *v''*, *v'''*, *u*, *u''* and *u'''* peaks represent the $3d^{10}4f^0$ state of Ce^{4+}, and the v^0, *v'*, u^0 and *u'* peaks represent the $3d^{10}4f^1$ state of Ce^{3+}.[19,26,37] The intensities of these peaks increased with the increasing Ce content in $Ni_yCe_{100-y}O_x$ samples. The concentration of Ce^{3+} and Ce^{4+} can be estimated according to the relative areas of the corresponding peaks. The major valence state of Ce was 4+, Ce^{3+} were also detected for $Ni_yCe_{100-y}O_x$ samples. It is commonly known that the oxygen vacancy defects will be formed with the appearance of Ce^{3+} to maintain electrostatic balance according to the equation 1.

$$4Ce^{4+} + O^{2-} \rightarrow 4Ce^{4+} + 2e^-/\square + 0.5O_2 \rightarrow 2Ce^{4+} + 2Ce^{3+} + \square + 0.5O_2 \qquad (2.1)$$

□ represents the empty position by the removal of O^{2-} from the lattice (*i.e.* oxygen vacancy defect). It suggests that the oxygen vacancy defects formed for the $Ni_yCe_{100-y}O_x$ samples, which is consistent with the Raman results.

2.3.4 Electrochemical performances of $Ni_yCe_{100-y}O_x$ catalysts

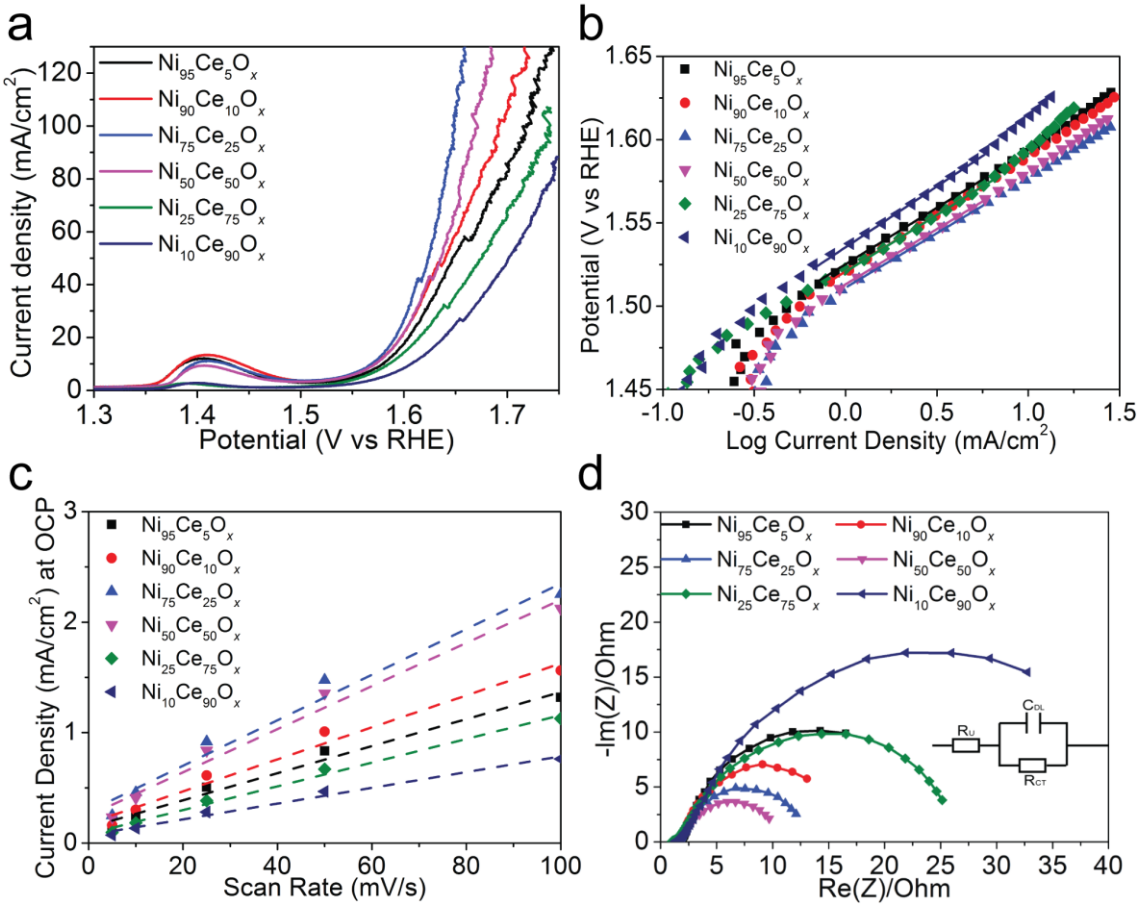

Figure 2.4 (a) Polarization curves of $Ni_yCe_{100-y}O_x$ catalysts for the OER with a scan rate of 10 mV/s. (b) Tafel plots obtained from the steady-state polarization curves with a scan rate of 1 mV/s. (c) Current density at OCP vs CV scan rate for $Ni_yCe_{100-y}O_x$ samples. The slope of current density at OCP vs scan rate stands for the double-layer capacitance. (d) Nyquist plots of $Ni_yCe_{100-y}O_x$ samples obtained at 1.55 V vs RHE. The inset is the electrical equivalent circuit.

To test the electrochemical performance of $Ni_yCe_{100-y}O_x$ catalysts, the polarization curves of these catalysts (Figure 2.4a) were obtained using Linear Sweep Voltammetry (LSV). The overpotentials of the catalysts for the current density of 10 mA/cm^2 are listed in Table 2.1. The $Ni_{10}Ce_{90}O_x$ catalyst showed the lowest current density for the applied

potentials, and had the largest overpotential of 363 mV for the current density of 10 mA/cm^2. The overpotentials for the $Ni_{75}Ce_{25}O_x$ and $Ni_{50}Ce_{50}O_x$ catalysts were 338 mV and 341 mV to obtain the current density of 10 mA/cm^2, which were lower than that of other samples. The Tafel slope results of $Ni_yCe_{100-y}O_x$ catalysts were shown in Figure 2.4b and Table 2.1. The $Ni_{75}Ce_{25}O_x$ and $Ni_{50}Ce_{50}O_x$ catalysts had the same lowest Tafel slope of 66 mV/decade. An electrocatalyst with a low Tafel slope will have a small kinetic barrier for electron and mass transfer.[9,38] This indicates that the transfer barriers of electron and mass in the $Ni_{75}Ce_{25}O_x$ and $Ni_{50}Ce_{50}O_x$ catalysts are lower than other $Ni_yCe_{100-y}O_x$ catalysts.

The double-layer capacitance can be used to estimate the electrochemically active surface area (ECSA) of each sample.[15,39] In order to know the double-layer capacitance, we first obtained CV curves of the capacitance current in the non-Faradaic voltage region (a 0.1 V potential range centered on the OCP) for several different scan rates (Figure 2.5). The rate of change in the current at OCP with respect to the scan rate corresponds to the double-layer capacitance.[40] For this reason, the current at OCP was plotted against the scan rate for the $Ni_yCe_{100-y}O_x$ catalysts, and a line of best fit was fitted for each catalyst's data set, as shown in Figure. 2.4c. The double layer capacitance was 12.3 mF, 14.5 mF, 20.6 mF, 19.5 mF, 10.7 mF and 7.1 mF for the $Ni_{95}Ce_5O_x$, $Ni_{90}Ce_{10}O_x$, $Ni_{75}Ce_{25}O_x$, $Ni_{50}Ce_{50}O_x$, $Ni_{25}Ce_{75}O_x$ and $Ni_{10}Ce_{90}O_x$ samples, respectively. The ECSA can be calculated according to the formula ECSA = C_{DL}/C_s, where a specific capacitance of C_s = 0.040 mF cm^{-2} was used in this work.[15] The calculated ECSA values for the $Ni_yCe_{100-y}O_x$ catalysts as well as other relevant electrochemistry parameters are summarized in Table 1. The ECSAs of the $Ni_{75}Ce_{25}O_x$ and $Ni_{50}Ce_{50}O_x$ catalysts are similar and larger than that of other $Ni_yCe_{100-y}O_x$ catalysts. This is consistent with the observed current densities, as a

larger ECSA means a sample has more active sites and therefore can catalyze more reactions at once and sustain a large current.

The charge transfer resistance (R_{CT}) of the $Ni_yCe_{100-y}O_x$ catalysts were obtained from their Nyquist plots, as shown in Figure 2.4d. As shown in Table 2.1, the R_{CT} of the $Ni_yCe_{100-y}O_x$ catalysts decreased firstly and then increased with the increasing Ce content in the catalysts, and the $Ni_{50}Ce_{50}O_x$ catalyst had the lowest R_{CT} of 7.5 Ω at an applied bias of 1.55 V vs RHE. The $Ni_{75}Ce_{25}O_x$ catalyst also showed a low R_{CT} of 9.9 Ω. However, the R_{CT} of the $Ni_{10}Ce_{90}O_x$ (31.8 Ω) catalyst was much higher than other $Ni_yCe_{100-y}O_x$ catalysts. The small mass-transfer resistance of the $Ni_{75}Ce_{25}O_x$ and $Ni_{50}Ce_{50}O_x$ catalysts stands for their favorable OER kinetics.

For the Ce-based catalysts, the oxygen mobility can be promoted by the generated oxygen vacancy defects, resulting an improved ionic conductivity.[26] Also, the oxygen vacancy defects can be act as the OER active sites to catalyze the water oxidation reaction.[21] Therefore, the larger concentration of oxygen vacancy defects result in the lower Tafel slopes, small mass-transfer resistance and larger ECSAs of the $Ni_{75}Ce_{25}O_x$ and $Ni_{50}Ce_{50}O_x$ catalysts, which account for the higher OER activities for these two catalysts.

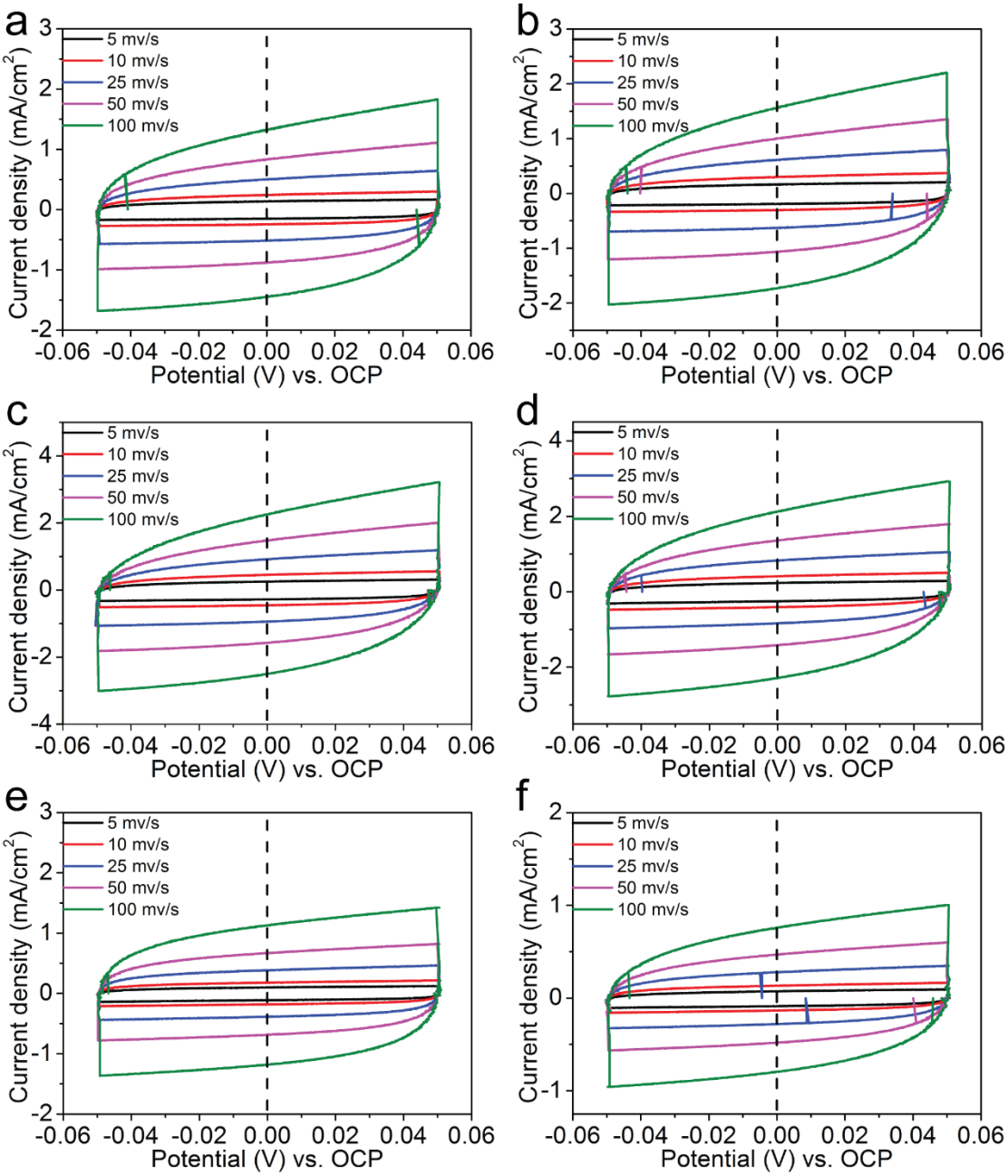

Figure 2.5 Cyclic voltammograms of (a) $Ni_{95}Ce_5O_x$, (b) $Ni_{90}Ce_{10}O_x$, (c) $Ni_{75}Ce_{25}O_x$, (d) $Ni_{50}Ce_{50}O_x$, (e) $Ni_{25}Ce_{75}O_x$ and (f) $Ni_{10}Ce_{90}O_x$ catalysts tested in a region with non-Faradaic process of the voltammogram with the scan rate of 5 mv/s, 10 mv/s, 25 mv/s, 50 mv/s and 100 mv/s.

Table 2.1. Electrochemistry active surface area (ECSA), Tafel slope, mass-transfer resistance (R_{CT}) and the overpotential (η) for the current density of 10 mA/cm^2 for each catalyst investigated in 1 M KOH

Catalyst	ECSA/cm^2	Tafel slope	R_{CT}	η for 10 mA/cm^2
$Ni_{95}Ce_5O_x$	307.5 cm^2	68 mV/decade	18.2 Ω	351 mV
$Ni_{90}Ce_{10}O_x$	362.5 cm^2	68 mV/decade	12.6 Ω	350 mV
$Ni_{75}Ce_{25}O_x$	515 cm^2	66 mV/decade	9.9 Ω	338 mV
$Ni_{50}Ce_{50}O_x$	487.5 cm^2	66 mV/decade	7.5 Ω	341 mV
$Ni_{25}Ce_{75}O_x$	267.5 cm^2	68 mV/decade	21 Ω	356 mV
$Ni_{10}Ce_{90}O_x$	177.5 cm^2	73 mV/decade	31.8 Ω	363 mV

2.3.5 Stability of $Ni_yCe_{100-y}O_x$ catalysts

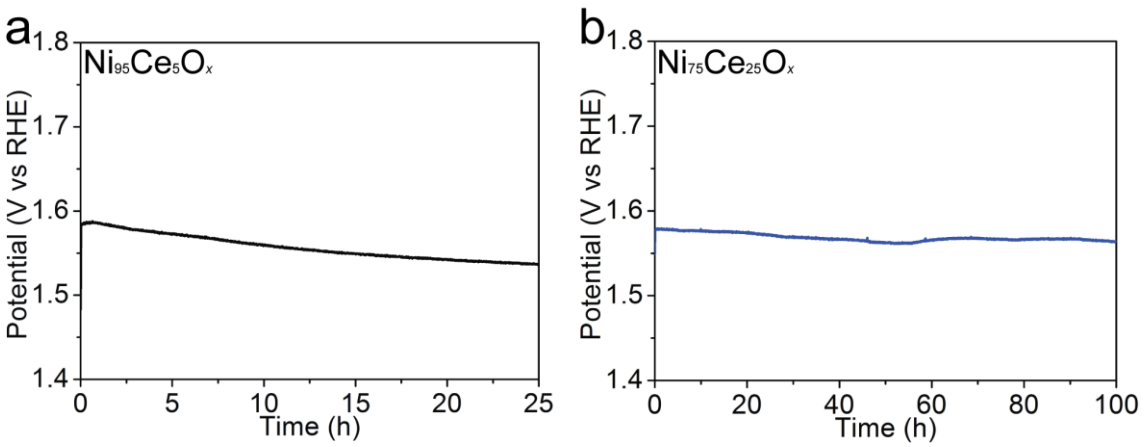

Figure 2.6 Potential trace of the $Ni_{95}Ce_5O_x$ and $Ni_{75}Ce_{25}O_x$ catalysts obtained by fixing the current density for electrolysis at 10 mA/cm^2. The electrolyte was 1 M KOH (pH ≈ 14).

Controlled-current water electrolysis (Figure. 2.6) was performed to analyze the

stability and long-term performance of the $Ni_{95}Ce_5O_x$ and $Ni_{75}Ce_{25}O_x$ catalysts. With a fixed current density of 10 mA/cm^2, the potential for the $Ni_{95}Ce_5O_x$ catalyst decreased clearly during the 25-hour water electrolysis process, while the potential for the $Ni_{75}Ce_{25}O_x$ catalyst remained stable at 1.57 V vs RHE for more than 100 h. This indicates that the $Ni_yCe_{100-y}O_x$ catalyst with high Ce content is more stable than the $Ni_yCe_{100-y}O_x$ catalyst with low Ce content during long-term water electrolysis.

2.4 Conclusions

In summary, a series of NF/NiO/$Ni_yCe_{100-y}O_x$ catalysts were synthesized through the simple dip-coating and annealing methods. The oxygen vacancy defects are formed successfully in all the $Ni_yCe_{100-y}O_x$ catalysts, and the concentration of oxygen vacancy defects for $Ni_{75}Ce_{25}O_x$ and $Ni_{50}Ce_{50}O_x$ catalysts are larger than other $Ni_yCe_{100-y}O_x$ catalysts. This results in the larger electrochemically active surface areas for $Ni_{75}Ce_{25}O_x$ and $Ni_{50}Ce_{50}O_x$ catalysts because of the abundant active sites offered by the defects. The rich oxygen vacancy defects also improve the ionic conductivity so that a lower Tafel slope of 66 mV/decade is obtained for $Ni_{75}Ce_{25}O_x$ and $Ni_{50}Ce_{50}O_x$ catalysts. The improved ionic conductivity also results in the small mass-transfer resistance of $Ni_{75}Ce_{25}O_x$ and $Ni_{50}Ce_{50}O_x$ catalysts, which is favorable for their OER kinetics. Therefore, the $Ni_{75}Ce_{25}O_x$ and $Ni_{50}Ce_{50}O_x$ catalyst exhibit higher OER activity than other $Ni_yCe_{100-y}O_x$ catalysts with the overpotential of 338 mV and 341 mV for the current density of 10 mA/cm^2. Additionally, the $Ni_yCe_{100-y}O_x$ catalyst with high Ce content ($Ni_{75}Ce_{25}O_x$) is more stable than the $Ni_yCe_{100-y}O_x$ catalyst with low Ce content ($Ni_{95}Ce_5O_x$) during long-term water electrolysis with a fixed current density of 10 mA/cm^2.

References

1 A. V. Herzog, T. E. Lipman and D. M. Kammen, *Encycl. Life Support Syst. (EOLSS). Forerunn. Vol. Overv. Life Support Syst. Sustain. Dev.*, 2001, 1–63.

2 N. L. Panwar, S. C. Kaushik and S. Kothari, *Renew. Sustain. Energy Rev.*, 2011, **15**, 1513–1524.

3 S. G. Chalk and J. F. Miller, *J. Power Sources*, 2006, **159**, 73–80.

4 M. Tahir, L. Pan, F. Idrees, X. Zhang, L. Wang, J. J. Zou and Z. L. Wang, *Nano Energy*, 2017, **37**, 136–157.

5 P. G. Bruce, S. A. Freunberger, L. J. Hardwick and J.-M. Tarascon, *Nat. Mater.*, 2012, **11**, 19–29.

6 Y. Gorlin and T. Jaramillo, *J. Am. Chem. Soc.*, 2010, **132**, 13612–13614.

7 T. N. Huan, G. Rousse, S. Zanna, I. T. Lucas, X. Xu, N. Menguy, V. Mougel and M. Fontecave, *Angew. Chemie - Int. Ed.*, 2017, **129**, 4870–4874.

8 M. Zhong, T. Hisatomi, Y. Sasaki, S. Suzuki, K. Teshima, M. Nakabayashi, N. Shibata, H. Nishiyama, M. Katayama, T. Yamada and K. Domen, *Angew. Chemie Int. Ed.*, 2017, **56**, 4739–4743.

9 J. Yu, Q. Cao, B. Feng, C. Li, J. Liu, J. K. Clark and J. Delaunay, 2018, **1**, 1–10.

10 C. Li, T. Hisatomi, O. Watanabe, M. Nakabayashi, N. Shibata, K. Domen and J.-J. Delaunay, *Energy {&} Environ. Sci.*, 2015, **8**, 1493–1500.

11 I. C. Man, H. Y. Su, F. Calle-Vallejo, H. A. Hansen, J. I. Martínez, N. G. Inoglu, J. Kitchin, T. F. Jaramillo, J. K. Nørskov and J. Rossmeisl, *ChemCatChem*, 2011, **3**, 1159–1165.

12 I. Katsounaros, S. Cherevko, A. R. Zeradjanin and K. J. J. Mayrhofer, *Angew.*

Chemie - Int. Ed., 2014, **53**, 102–121.

13 T. Audichon, T. W. Napporn, C. Canaff, C. Morais, C. Comminges and K. B. Kokoh, *J. Phys. Chem. C*, 2016, **120**, 2562–2573.

14 N.-T. Suen, S.-F. Hung, Q. Quan, N. Zhang, Y.-J. Xu and H. M. Chen, *Chem. Soc. Rev.*, 2017, **46**, 337–365.

15 C. C. L. McCrory, S. Jung, J. C. Peters and T. F. Jaramillo, *J. Am. Chem. Soc.*, 2013, **135**, 16977–16987.

16 J. Wang, W. Cui, Q. Liu, Z. Xing, A. M. Asiri and X. Sun, *Adv. Mater.*, 2016, **28**, 215–230.

17 X. F. Lu, L. F. Gu, J. W. Wang, J. X. Wu, P. Q. Liao and G. R. Li, *Adv. Mater.*, 2017, **29**, 1604437.

18 J. X. Feng, H. Xu, Y. T. Dong, S. H. Ye, Y. X. Tong and G. R. Li, *Angew. Chemie - Int. Ed.*, 2016, **55**, 3694–3698.

19 J. W. D. Ng, M. García-Melchor, M. Bajdich, P. Chakthranont, C. Kirk, A. Vojvodic and T. F. Jaramillo, *Nat. Energy*, 2016, **1**, 16053.

20 S. Polarz, J. Strunk, V. Ischenko, M. W. E. Van Den Berg, O. Hinrichsen, M. Muhler and M. Driess, *Angew. Chemie - Int. Ed.*, 2006, **45**, 2965–2969.

21 D. Yan, Y. Li, J. Huo, R. Chen, L. Dai and S. Wang, *Adv. Mater.*, 2017, **29**, 1606459.

22 R. Gao and D. Yan, *Nano Res.*, 2018, **11**, 1883–1894.

23 Q. Fu, H. Saltsburg and M. Flytzani-Stephanopoulos, *Science (80-.).*, 2003, **301**, 935–938.

24 F. Esch, S. Fabris and L. Zhou, *Science (80-.).*, 2005, **309**, 752–755.

25 L. Chen, P. Fleming, V. Morris, J. D. Holmes and M. A. Morris, *J. Phys. Chem. C*, 2010, **114**, 12909–12919.

26 J. Yu, Z. Si, L. Chen, X. Wu and D. Weng, *Appl. Catal. B Environ.*, 2015, **163**, 223–232.

27 L. Han, S. Dong and E. Wang, *Adv. Mater.*, 2016, **28**, 9266–9291.

28 J.-X. Feng, S.-H. Ye, H. Xu, Y.-X. Tong and G.-R. Li, *Adv. Mater.*, 2016, **28**, 4698–4703.

29 C. Fisica and U. Milano, *Pure Appl. Chem.*, 1991, **63**, 711–734.

30 T. Taniguchi, T. Watanabe, N. Sugiyama, A. K. Subramani, H. Wagata, N. Matsushita and M. Yoshimura, *J. Phys. Chem. C*, 2009, **113**, 19789–19793.

31 M. Guo, J. Lu, Y. Wu, Y. Wang and M. Luo, *Langmuir*, 2011, **27**, 3872–3877.

32 A. Nakajima, A. Yoshihara and M. Ishigame, *Phys. Rev. B*, 1994, **50**, 13297–13307.

33 J. E. Spanier, R. D. Robinson, F. Zhang, S.-W. Chan and I. P. Herman, *Phys. Rev. B*, 2001, **64**, 245407.

34 L. He, B. Liang, L. Li, X. Yang, Y. Huang, A. Wang, X. Wang and T. Zhang, *ACS Catal.*, 2015, **5**, 1623–1628.

35 A. Filtschew, K. Hofmann and C. Hess, *J. Phys. Chem. C*, 2016, **120**, 6694–6703.

36 A. Badri, C. Binet and J. Lavalley, *J. Chem. Soc. Faraday Trans.*, 1996, **92**, 4669–4673.

37 J. Chastain, R. C. King and J. F. Moulder, *Handbook of X-ray photoelectron spectroscopy: a reference book of standard spectra for identification and interpretation of XPS data*, Physical Electronics Eden Prairie, MN, 1995.

38 F. Yu, F. Li, B. Zhang, H. Li and L. Sun, *ACS Catal.*, 2015, **5**, 627–630.

39 J. D. Benck, Z. Chen, L. Y. Kuritzky, A. J. Forman and T. F. Jaramillo, *ACS Catal.*, 2012, **2**, 1916–1923.

40 Y. Q. Gao, H. B. Li and G. W. Yang, *J. Appl. Phys.*, 2016, **119**, 034902.

3. Synthesis of $NiCeO_x$ catalysts through thermal diffusion of Ni for oxygen evolution reaction

3.1 Introduction

Using the NF substrate as the source of nickel for the synthesis of nickel-based catalysts has seldom been reported. By doing this, the advantages of NF can be retained, and the NF forms a strong connection with the surface catalyst which is good for the long-term stability of the catalyst.

The NF/NiO/$Ni_yCe_{100-y}O_x$ catalysts with defects have been successfully synthesized and shown good OER performance. In this chapter, NF will be used directly as the substrate instead of NF/NiO in order to simplify the synthesis process and reduce the material costs, which is beneficial for industry application. Moreover, the adhesion between the top catalyst layer and the substrate will be stronger.

In this work, a series of $NiCeO_x$ with different dip-coating times ($NiCeO_x$-Y) were synthesized directly on commercially available nickel foam (NF) using a simple, low-cost, environmentally friendly and reproducible synthesis method that consists of first dip-coating the NF in a cerium pre-cursor and then annealing the sample at 400 °C. With the dip-coating times increasing from 1 to 15, the thickness of the surface layer, the concentration of formed oxygen vacancy defects and the OER performance remain constant increasing for $NiCeO_x$-Y catalysts. For the $NiCeO_x$-20 catalyst, the increased Ce content leads to the decrease of the oxygen vacancy defects, resulting in the lower OER performance than the $NiCeO_x$-15 catalyst.

3.2 Experimental Section

3.2.1 Synthesis of $NiCeO_x$ catalysts with varying thickness on Ni foam substrate

Preparation of the NiO catalyst: A 10 x 15 mm^2 Nickel Foam (NF, >99.99%, MTI Corporation) substrate with a thickness of 0.08 mm was firstly cleaned by acetone (99%, Wako) in an ultrasonic bath for 5 min. Then the NF was rinsed by deionized water for three times. Subsequently, the NF was dried in air, and annealed for 2 h with a heating rate of 2 °C/min at 400 °C in a muffle furnace.

Preparation of the $NiCeO_x$ catalyst: A cerium precursor solution was first synthesized by dissolving $Ce(NO_3)_3 \cdot 6H_2O$ (99.99%, Aldrich) in a mixture of 0.3 M citric acid (98%, Wako) and ethanol.[1] The prepared solution was then deposited onto a cleaned NF substrate (using the same cleaning method described above) by dip-coating. Finally, the sample was annealed in the same manner as the NiO catalyst. A series of $NiCeO_x$-Y ($NiCeO_x$-1, $NiCeO_x$-2, $NiCeO_x$-5, $NiCeO_x$-8, $NiCeO_x$-10, $NiCeO_x$-15, $NiCeO_x$-20) catalysts were prepared using the previous methods, and Y stood for the dip-coating times.

3.2.2 Structural characterization

A field emission Scanning electron microscope (SEM, JEOL JSM 7600 FA) was used for the measurements of SEM. A Renishaw inVia Raman Microscope system was used to acquire the Raman spectra at room temperature. A ×100 objective and a 532 nm excitation laser were used. A PHI 5000 VersaProbe (ULVAC-PHI) with an Al Kα X-ray source (1486.6 eV) was used to obtain the X-ray photoelectron spectroscopy (XPS). The pass energies of 117.4 eV and 23.5 eV were used for the electron analyzer to analyze the wide scans and narrow scans, respectively.

3.2.3 Electrochemical measurements

A cylindrical glass cell with a standard three-electrode configuration was used for the electrochemical measurements. A Pt wire and a Ag/AgCl electrode were used as the counter electrode and the reference electrode, respectively. The working electrode was NF/$NiCeO_x$-Y, hereafter simply referred to as the $NiCeO_x$-Y electrode. A potentiostat (Princeton Applied Research, VersaSTAT 4) was used to perform the electrochemical measurements. The potentials were calibrated against the RHE according to the following equation: ($E_{RHE} = E_{Ag/AgCl} + 0.059\ pH + E^0_{Ag/AgCl}$), where $E_{Ag/AgCl}$ is the potential difference measured between the Ag/AgCl electrode and the working electrode, $E^0_{Ag/AgCl}$ (0.1976 V at 25 °C) is the standard electrode potential for a Ag/AgCl electrode, pH is the pH of the electrolyte solution, and E_{RHE} is the calibrated potential. The electrolytes used were saturated with oxygen before and during the OER experiments.

The polarization curves were collected through linear sweep voltammetry (LSV), and the scan rate was 10 mV/s. Controlled-current water electrolysis was performed using a chronopotentiometric technique.[2] The solution resistance R_s (~ 2 Ω), determined using the electrochemical impedance spectroscopy (EIS) technique,[2] was used to correcte the *iR* drop across the solution. Unless otherwise stated, all given potentials are vs RHE and corrected for the *iR* drop across the electrolyte. Cyclic voltammetry (CV) was used to determine the electrochemical capacitance of the samples presented in this paper.[2,3] The potential was swept in a range from 0.05 V above the open-circuit potential (OCP) to 0.05V below the OCP in a static solution with five different scan rates: 0.005, 0.01, 0.025, 0.05 and 0.1 V s^{-1}. The working electrode was held for 10 s at each end of the potential sweep before continuing to the next sweep. All experiments were performed at room temperature.

3.3 Results and Discussion

3.3.1 Morphologies of $NiCeO_x$ catalysts with varying thickness

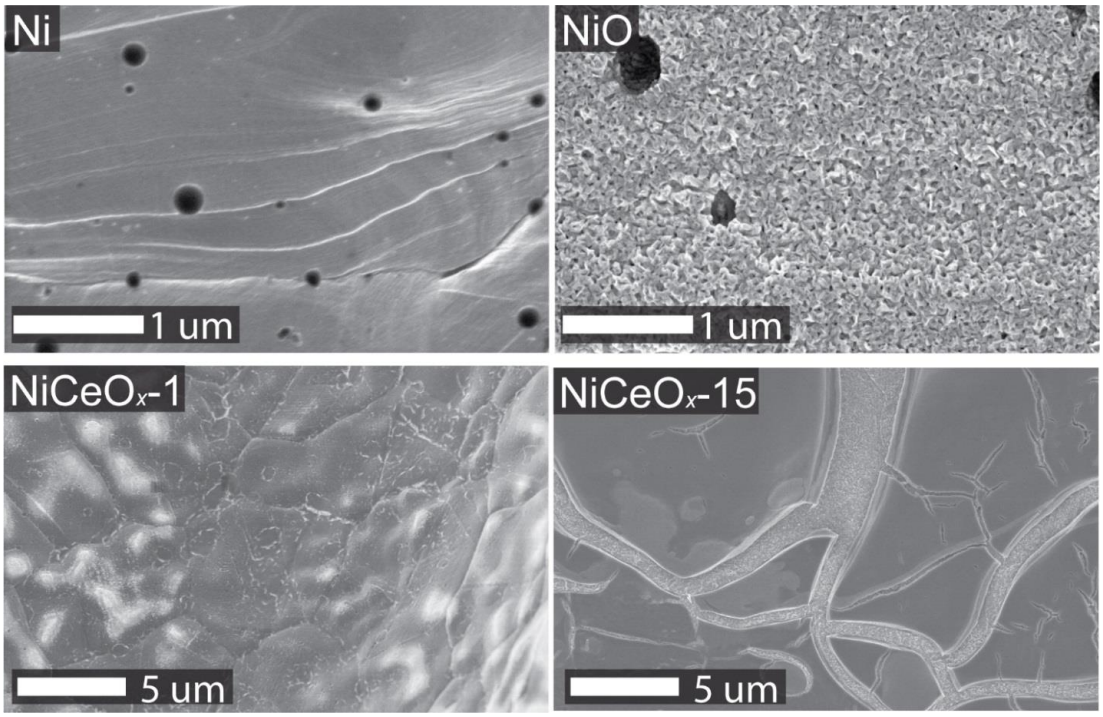

Figure 3.1 SEM images of (a) the Ni, (b) NiO, (c) $NiCeO_x$-1 and (d) $NiCeO_x$-15 samples.

Morphology of the Ni foam (NF) substrate is shown in Figure 3.1a. Holes with sizes varying from several nanometers to a few hundred nanometers were observed on the surface of Ni. NiO sample was prepared by annealing Ni substrate in the muffle furnace for 2 hours with the elevating rate of 2 °C/min. The surface of NiO consisted of small nanocrystals, as shown in Figure 3.1b. The $NiCeO_x$-Y samples were synthesized by depositing a cerium salt solution on NF and then annealing the sample in air to form a $NiCeO_x$ layer on top of the NFs. The synthesis difference among the series $NiCeO_x$-Y samples was the times of dip coating. The morphology of $NiCeO_x$-1 and $NiCeO_x$-15 samples were shown in Figure 3.1c and Figure 3.1d. With increasing the dip-coating times,

the thickness of the deposited $NiCeO_x$ surface layer increased. Cracks, that are believed to have formed as a result of a combination of thermal stress in the layer and the release of gas produced by the decomposition of nitrate ions during the annealing process, were also observed.

3.3.2 Oxygen vacancies of $NiCeO_x$ catalysts with varying thickness

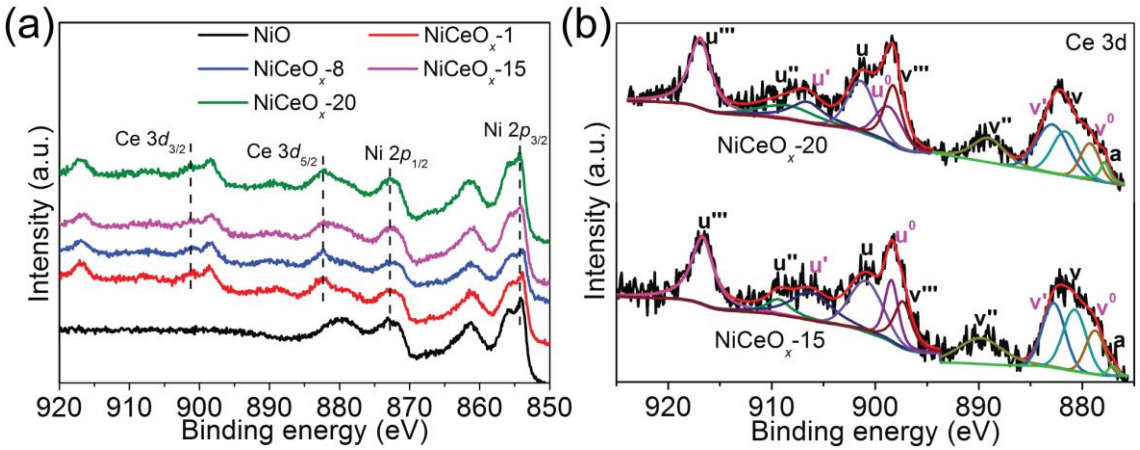

Figure 3.2 (a) XPS spectra of the NiO, $NiCeO_x$-1, $NiCeO_x$-8, $NiCeO_x$-15 and $NiCeO_x$-20 samples. (b) Ce 3d spectra of the $NiCeO_x$-15 and $NiCeO_x$-20 samples. The peak labeled *a* in the XPS spectra is ascribed to the Ni 2p peak.

XPS was carried out on NiO, $NiCeO_x$-1, $NiCeO_x$-8 and $NiCeO_x$-15 and $NiCeO_x$-20 samples to analyze the surface element information of the samples. As shown in Figure 3.2a, the observed XPS peaks in the NiO sample could be attributed to the Ni $2p_{3/2}$ peak (854.1 eV), the Ni $2p_{1/2}$ peak (872.5 eV) and the intense satellite peaks (861.3 eV and 879.9 eV) characteristic of NiO.[4] Additional Ce 3d peaks, associated with CeO_2, were also observed for other $NiCeO_x$-Y samples. This indicates that the cerium oxide has been

formed successfully on the surface of the $NiCeO_x$-Y samples. The Ce 3d band is composed of ten individual peaks, that are labeled on Figure 3.2b as *v*, *v″*, *v‴*, *u*, *u″*, *u‴*, v^0, *v′*, u^0 and *u′*. The *v*, *v″*, *v‴*, *u*, *u″* and *u‴* peaks represent the $3d^{10}4f^0$ state of Ce^{4+}, and the v^0, *v′*, u^0 and *u′* peaks represent the $3d^{10}4f^1$ state of Ce^{3+}.[4–6] Based on the relative areas of the Ce^{3+} and Ce^{4+} peaks, it was possible to determine that the Ce^{3+} concentration is 37% for the $NiCeO_x$-15 sample and 34% for the $NiCeO_x$-20 sample. The increase in the concentration of Ce^{3+} is a result of the reduction of Ce^{4+} by the removal of lattice O^{2-} anions via oxygen vacancy generation.[5] It suggests that more oxygen vacancy defects formed in the $NiCeO_x$-15 sample when compared with the $NiCeO_x$-20 sample. The much more dip-coating times lead to more cerium salt deposited onto Ni foam substrate, resulting in the high Ce content of the $NiCeO_x$-20 sample than that of the $NiCeO_x$-15 sample. According to the results in chapter 2, the concentration of oxygen vacancy defects will decrease when the Ce content is higher than 25%. This may be the reason why the concentration of oxygen vacancy defects in the $NiCeO_x$-20 sample is lower than that in the $NiCeO_x$-15 sample.

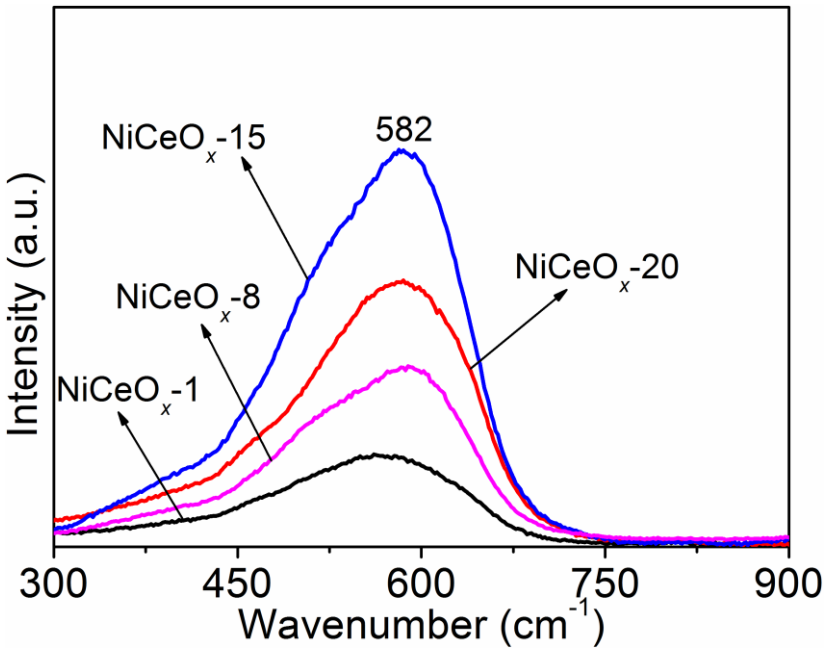

Figure 3.3 Raman spectra of the $NiCeO_x$-1, $NiCeO_x$-8, $NiCeO_x$-15 and $NiCeO_x$-20 samples.

Figure 3.3 shows the Raman spectra of the $NiCeO_x$-1, $NiCeO_x$-8, $NiCeO_x$-15 and $NiCeO_x$-20 samples. A broad peak around 582 cm^{-1} (D band) was observed for all the $NiCeO_x$-Y samples. Crystalline CeO_2 is known to have a strong F_{2g} Raman peak at 464 cm^{-1} related to its crystalline structure.[7] The presence of ions with the oxidation states lower than Ce^{4+} in the CeO_2 has been shown to induce a Raman band, known as the D band, from 500 to 700 cm^{-1}.[7–9] This band is associated with the presence of oxygen vacancy defects created in the non-stoichimometric CeO_{2-y} by the 3+ coordinated ions. In addition to the introduction of the D band, the F_{2g} band will be weakened and becomes asymmetric and broad.[10] In the Raman spectra of the $NiCeO_x$-Y samples, there were no F_{2g} band, which suggests that there is no crystalline CeO_2 with a fluorite structure in the deposited layers.[11] The strong intensity of the peak seen at 582 cm^{-1} (D band) indicates the formation of a large number of oxygen vacancy defects within the $NiCeO_x$ layer. The

oxygen vacancy defects should be related to the presence of Ce^{3+} because of the incorporation of Ni into CeO_2, as suggested by the literature[7,8,11]. Furthermore, the amorphous structure of the $NiCeO_x$-Y layers contributes to the broadness of the peak.[10,11] With the increasing of dip-coating times, the peak area of 582 cm^{-1} increased firstly, and then decreased for the $NiCeO_x$-Y samples. The peak area of the $NiCeO_x$-15 sample is the largest among the samples, indicating that the concentration of oxygen vacancy defects of $NiCeO_x$-15 is the largest. The peak area of 582 cm^{-1} for the $NiCeO_x$-20 sample was lower than that of the $NiCeO_x$-15 sample, suggesting the lower concentration of oxygen vacancy defects. This is in consistent with the XPS results.

3.3.3 Electrochemical performances of $NiCeO_x$ catalysts with varying thickness

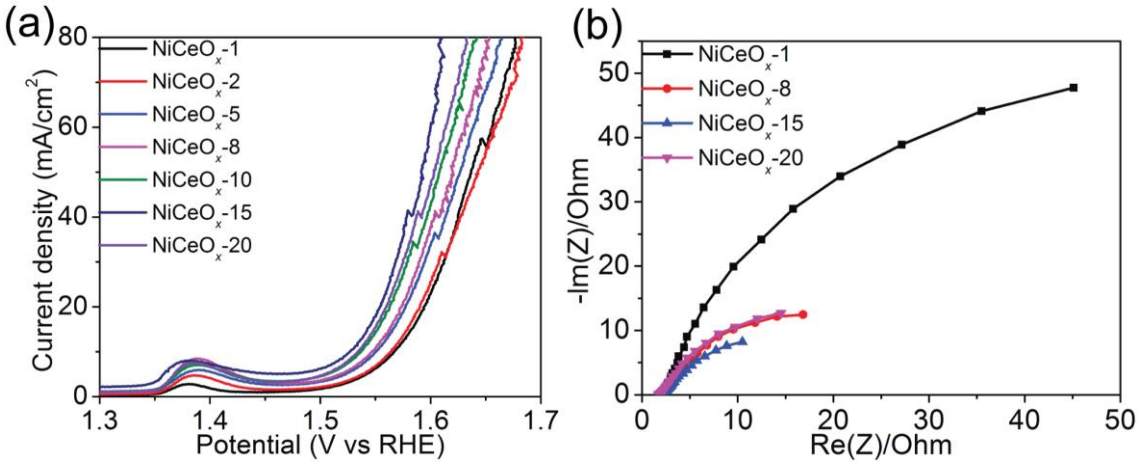

Figure 3.4 (a) Polarization curves of $NiCeO_x$-Y samples for the OER with a scan rate of 10 mV/s. The electrolyte was 1 M KOH. (b) Nyquist plots of the $NiCeO_x$-1, $NiCeO_x$-8, $NiCeO_x$-15 and $NiCeO_x$-20 samples obtained at 1.5 V vs RHE. The inset shows the electrical equivalent circuit.

To test the OER activity of the $NiCeO_x$-Y samples, the polarization curves of the samples were obtained using Linear Sweep Voltammetry (LSV), as shown in Figure 3.4a. The $NiCeO_x$-1 and $NiCeO_x$-2 samples showed the similar current density for the applied potentials. For the applied potentials, the current density of other $NiCeO_x$-Y samples (from $NiCeO_x$-5 to $NiCeO_x$-20) were higher than $NiCeO_x$-1 and $NiCeO_x$-2 samples, and $NiCeO_x$-15 exhibited the best current density. The overpotential (η) at the current density of 10 mA/cm^2 of $NiCeO_x$-Y samples were listed in Table 3.1, and following the sequence η ($NiCeO_x$-1) ≈ η ($NiCeO_x$-2) < η ($NiCeO_x$-5) ≈ η ($NiCeO_x$-8) < η ($NiCeO_x$-10) < η ($NiCeO_x$-15) > η ($NiCeO_x$-20). $NiCeO_x$-15 had the lowest overpotential of 295 mV for the current density of 10 mA/cm^2. The charge transfer resistance (R_{CT}) of the $NiCeO_x$-1, $NiCeO_x$-8, $NiCeO_x$-15 and $NiCeO_x$-20 catalysts were obtained from their Nyquist plots, as shown in Figure 3.4b. The R_{CT} of the $NiCeO_x$-Y catalysts decreased firstly and then increased with the increasing dip-coating times. The $NiCeO_x$-15 catalyst had the lowest R_{CT} of 12 Ω at an applied bias of 1.5 V vs RHE. The $NiCeO_x$-8 and $NiCeO_x$-20 catalysts showed the similar R_{CT} of 20.1 and 19.6 Ω, and the R_{CT} of $NiCeO_x$-1 (77.8 Ω) was much larger than other catalysts. The small mass-transfer resistance of the $NiCeO_x$-15 catalyst is favorable for the OER kinetics.

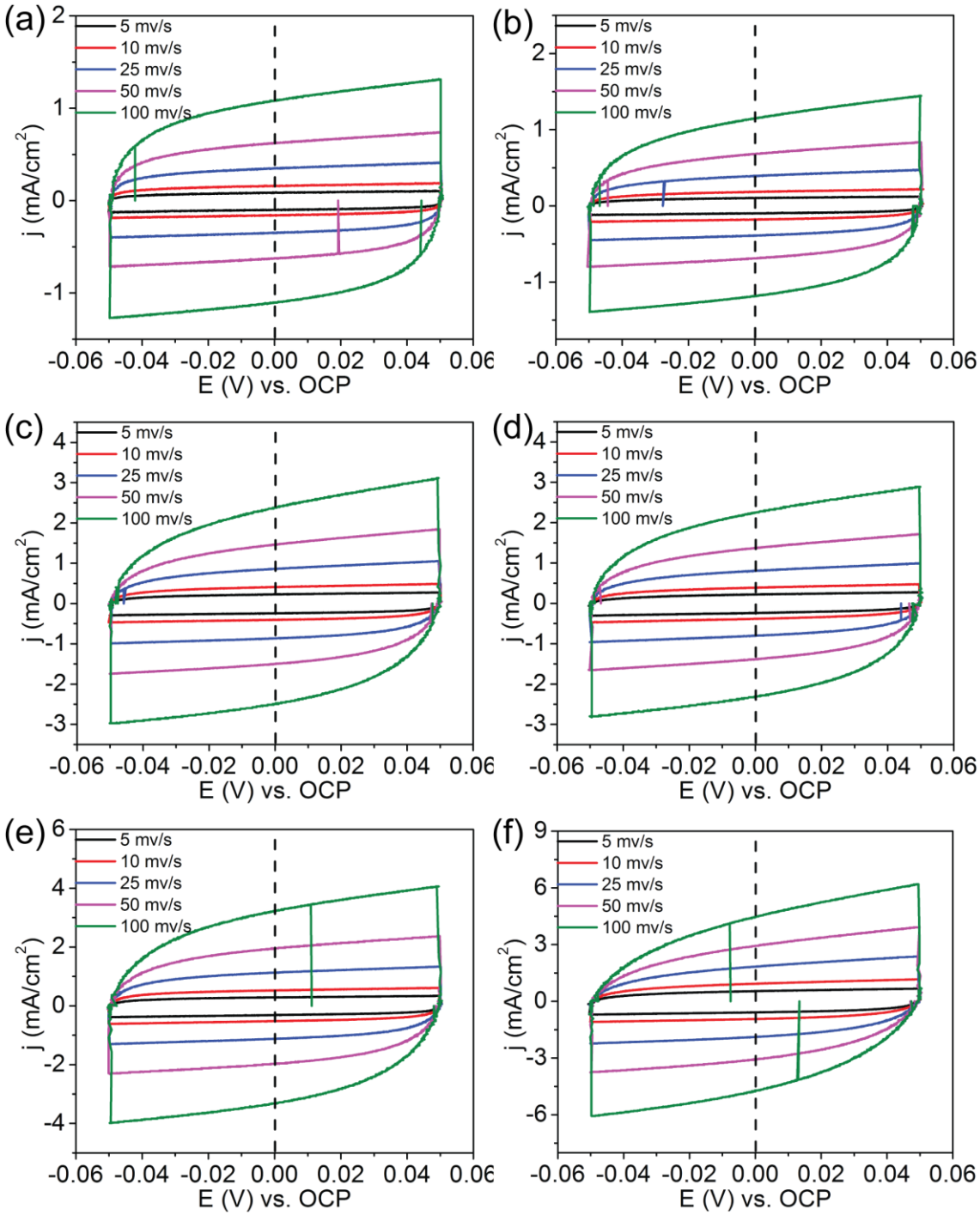
(a)
(b)
(c)
(d)
(e)
(f)
5 mv/s
10 mv/s
25 mv/s
50 mv/s
100 mv/s
j (mA/cm^2)
E (V) vs. OCP

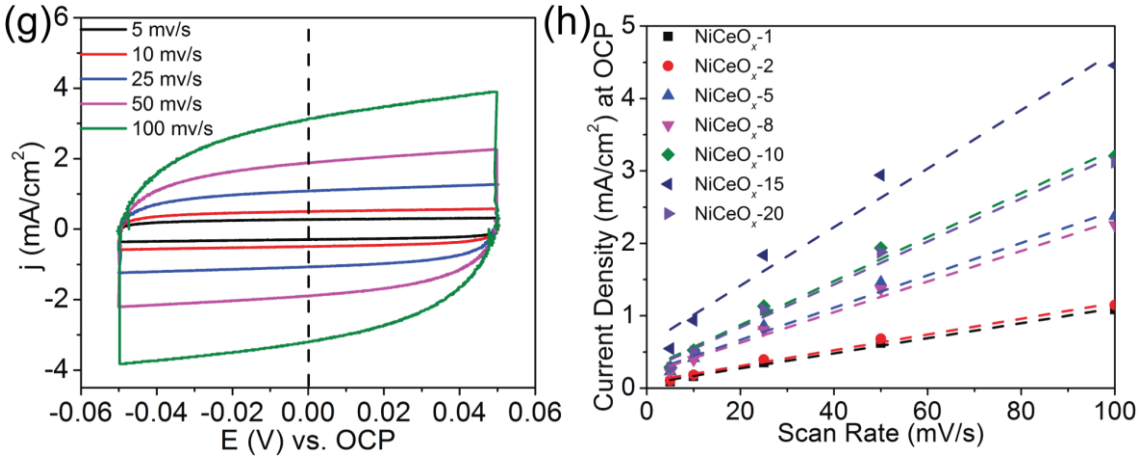

Figure 3.5 Cyclic voltammograms of (a) NiCeO$_x$-1, (b) NiCeO$_x$-2, (c) NiCeO$_x$-5, (d) NiCeO$_x$-8, (e) NiCeO$_x$-10, (f) NiCeO$_x$-15 and (g) NiCeO$_x$-20 samples were performed in a region with non-Faradaic process of the voltammogram with the scan rates of 5 mv/s, 10 mv/s, 25 mv/s, 50 mv/s and 100 mv/s for the OER. The electrolyte was 1 M KOH. (h) Current density at OCP vs CV scan rate for the NiCeO$_x$-Y samples. The slope of current density at OCP vs scan rate represents the double-layer capacitance.

To know the double-layer capacitance, we first obtained CV curves of the capacitance current in the non-Faradaic voltage region (a 0.1 V potential range centered on the OCP) for several different scan rates (Figure 3.5a-3.5g). The rate of change in the current at OCP with respect to the scan rate corresponds to the double-layer capacitance.[12] For this reason, the current at OCP was plotted against the scan rate for the NiCeO$_x$-Y samples, and a line of best fit was fitted for each sample's data set, as shown in Figure 2.4h. The double layer capacitance was 10.4 mF, 10.9 mF, 22.3 mF and 21.1 mF, 30.4 mF, 40.4 mF and 29.7 mF for the NiCeO$_x$-1, NiCeO$_x$-2, NiCeO$_x$-5, NiCeO$_x$-8, NiCeO$_x$-10, NiCeO$_x$-15 and NiCeO$_x$-20 samples, respectively. The ECSA can be calculated according to the formula ECSA = C_{DL}/C_s, where a specific capacitance of C_s = 0.040 mF/cm^2 was

used in this work.[2] The calculated ECSA values for the four samples as well as other relevant electrochemistry parameters are summarized in Table 3.1. The ECSA of $NiCeO_x$-1 and $NiCeO_x$-2 were found to be similar and the lowest among the $NiCeO_x$-Y samples. $NiCeO_x$-5 and $NiCeO_x$-8 samples also had the similar ECSA, and their ECSA nearly twice that of $NiCeO_x$-1. For $NiCeO_x$-10 and $NiCeO_x$-20 samples, their ECSA were about third times that of $NiCeO_x$-1. The $NiCeO_x$-15 sample owed the largest ECSA, which was forth times that of $NiCeO_x$-1. This is consistent with the observed current densities ($J_{NiCeOx\text{-}15} > J_{NiCeOx\text{-}20} \approx J_{NiCeOx\text{-}10} > J_{NiCeOx\text{-}8} \approx J_{NiCeOx\text{-}5} > J_{NiCeOx\text{-}2} \approx J_{NiCeOx\text{-}1}$), as a larger ECSA means a sample has more active sites and therefore can catalyze more reactions at once and sustain a large current.

Table 3.1. Double-layer capacitance (C_{DL}), electrochemically active surface area (ECSA) and overpotential (η) at the current density of 10 mA/cm² of $NiCeO_x$-Y for OER Investigated in 1 M KOH

Catalyst	C_{DL}/cm²	ECSA/cm²	η/mV
$NiCeO_x$-1	10.4 mF	260 cm²	337
$NiCeO_x$-2	10.9 mF	272.5 cm²	334
$NiCeO_x$-5	22.3 mF	557.5 cm²	321
$NiCeO_x$-8	21.1 mF	527.5 cm²	317
$NiCeO_x$-10	30.4 mF	760 cm²	307
$NiCeO_x$-15	40.4 mF	1010 cm²	295
$NiCeO_x$-20	29.7 mF	742.5 cm²	305

3.4 Conclusions

In summary, a series of $NiCeO_x$ catalysts with dip-coating times from 1 to 20 ($NiCeO_x$-Y, Y is the dip-coating times) were successfully synthesized using a simple dip-coating/annealing method. With the largest number of oxygen vacancy defects, the $NiCeO_x$-15 catalyst have the largest electrochemically active surface area, the lowest mass-transfer resistance and the lowest overpotential of 295 mV for 10 mA/cm^2, indicating the OER activity of the $NiCeO_x$-15 catalyst is the best among the $NiCeO_x$-Y catalysts.

References

1 N. Ozera, J. P. Cronin and S. Akyuza, 1999, **3788**, 195–214.

2 C. C. L. McCrory, S. Jung, J. C. Peters and T. F. Jaramillo, *J. Am. Chem. Soc.*, 2013, **135**, 16977–16987.

3 C. Fisica and U. Milano, *Pure Appl. Chem.*, 1991, **63**, 711–734.

4 J. Chastain, R. C. King and J. F. Moulder, *Handbook of X-ray photoelectron spectroscopy: a reference book of standard spectra for identification and interpretation of XPS data*, Physical Electronics Eden Prairie, MN, 1995.

5 J. Yu, Z. Si, L. Chen, X. Wu and D. Weng, *Appl. Catal. B Environ.*, 2015, **163**, 223–232.

6 J. W. D. Ng, M. García-Melchor, M. Bajdich, P. Chakthranont, C. Kirk, A. Vojvodic and T. F. Jaramillo, *Nat. Energy*, 2016, **1**, 16053.

7 T. Taniguchi, T. Watanabe, N. Sugiyama, A. K. Subramani, H. Wagata, N. Matsushita and M. Yoshimura, *J. Phys. Chem. C*, 2009, **113**, 19789–19793.

8 M. Guo, J. Lu, Y. Wu, Y. Wang and M. Luo, *Langmuir*, 2011, **27**, 3872–3877.

9 A. Nakajima, A. Yoshihara and M. Ishigame, *Phys. Rev. B*, 1994, **50**, 13297–13307.

10 J. E. Spanier, R. D. Robinson, F. Zhang, S.-W. Chan and I. P. Herman, *Phys. Rev. B*, 2001, **64**, 245407.

11 L. He, B. Liang, L. Li, X. Yang, Y. Huang, A. Wang, X. Wang and T. Zhang, *ACS Catal.*, 2015, **5**, 1623–1628.

12 Y. Q. Gao, H. B. Li and G. W. Yang, *J. Appl. Phys.*, 2016, **119**, 34902.

4. Oxygen vacancy-rich $NiCeO_x$ catalyst for water electrolysis

4.1 Introduction

In the last chapter, the $NiCeO_x$-Y catalysts with oxygen vacancy defects were reported to be synthesized directly on NF successfully. The $NiCeO_x$-15 catalyst showed the best OER activity among the $NiCeO_x$-Y catalysts. However, the reason for the formation of oxygen vacancy defects in $NiCeO_x$-Y catalysts need be further investigated, and the relationship between oxygen vacancy defects and the OER performance lacks of direct experimental evidence.

In this work, the formation of the $NiCeO_x$ top layer of the $NiCeO_x$ catalyst has been explained. During the annealing step, Ni atoms diffuse from the NF substrate into the deposited layer, forming an amorphous $NiCeO_x$ layer through thermal diffusion. The incorporation of Ni into CeO_2 induces a large number of oxygen vacancies. The oxygen vacancies are shown to enhance the catalytic activity of the $NiCeO_x$ catalyst by supplying an abundance of active sites and improving the ionic conductivity, allowing it to outperform noble metal OER catalysts. Furthermore, the $NiCeO_x$ catalyst is found to be extremely stable, making it viable as an electrocatalyst in industrial scale water splitting.

4.2 Experimental Section

4.2.1 Synthesis of $NiCeO_x$ and NiO/CeO_2 catalysts

For NiO catalyst, a 10 x 15 mm^2 Nickel Foam (NF, >99.99%, MTI Corporation) substrate with a thickness of 0.08 mm was firstly cleaned by acetone (99%, Wako) in an ultrasonic bath for 5 min. Then the NF was rinsed by deionized water for three times. Subsequently, the NF was dried in air, and annealed for 2 h with a heating rate of 2 °C/min at 400 °C in a muffle furnace. For NiO/CeO_2 catalyst, a cerium precursor solution was first synthesized by dissolving $Ce(NO_3)_3 \cdot 6H_2O$ (99.99%, Aldrich) in a mixture of 0.3 M citric acid (98%, Wako) and ethanol.[1] The prepared solution was then deposited onto a prepared NiO by dip-coating. Finally, the sample was annealed in the same manner as the NiO catalyst. For $NiCeO_x$ catalyst, a cleaned NF (using the same cleaning method described above) instead of NiO as the substrate and the synthesis method are the same with that of NiO/CeO_2.

4.2.2 Structural Characterization of $NiCeO_x$ and NiO/CeO_2 catalysts

A field emission Scanning electron microscope (SEM, JEOL JSM 7600 FA) was used for the measurements of SEM. A diffractometer (Rigaku Co. Ltd, SmartLab, Japan) with Cu Kα radiation (dwelling time = 2 s, incident angle = 0.5°, step size = 0.02°, λ = 1.541 Å) was used for the colleting of grazing incidence X-ray diffraction data. A Renishaw inVia Raman Microscope system was used to acquire the Raman spectra at room temperature. A ×100 objective and a 532 nm excitation laser were used. A PHI 5000 VersaProbe (ULVAC-PHI) with an Al Kα X-ray source (1486.6 eV) was used to obtain the X-ray photoelectron spectroscopy (XPS). The pass energies of 117.4 eV and 23.5 eV

were used for the electron analyzer to analyze the wide scans and narrow scans, respectively. The cross-sectional TEM samples were prepared using a FIB-SEM (JEOL JIB 4600F). High resolution TEM images, diffraction patterns and scanning transmission electron microscopy (STEM) images were measured with a JEOL JEM-2800. STEM-EDS (line EDS at below 1 nm resolution) was measured using an X-MAX 100TLE SDD detector (Oxford Instruments).

4.2.3 Electrochemical measurements of $NiCeO_x$ and NiO/CeO_2 catalysts

A cylindrical glass cell with a standard three-electrode configuration was used for the electrochemical measurements. A Pt wire and a Ag/AgCl electrode were used as the counter electrode and the reference electrode, respectively. The working electrode was NF, NiO, NiO/CeO_2 and $NiCeO_x$ catalysts. A potentiostat (Princeton Applied Research, VersaSTAT 4) was used to perform the electrochemical measurements. The potentials were calibrated against the RHE according to the following equation: ($E_{RHE} = E_{Ag/AgCl} + 0.059\ pH + E^0_{Ag/AgCl}$), where $E_{Ag/AgCl}$ is the potential difference measured between the Ag/AgCl electrode and the working electrode, $E^0_{Ag/AgCl}$ (0.1976 V at 25 °C) is the standard electrode potential for a Ag/AgCl electrode, pH is the pH of the electrolyte solution, and E_{RHE} is the calibrated potential. The electrolytes used were saturated with oxygen before and during the OER experiments, and nitrogen before and during the HER and full water-splitting experiments.

The polarization curves were collected through linear sweep voltammetry (LSV) with a scan rate of 10 mV/s. The LSV measurement was repeated for at least 10 times to obtain a stable result. Controlled-current water electrolysis was performed using a chronopotentiometric technique.[2] The solution resistance R_s (~ 2 Ω), determined using

the electrochemical impedance spectroscopy (EIS) technique,[2] was used to correcte the *iR* drop across the solution. Unless otherwise stated, all given potentials are vs RHE and corrected for the *iR* drop across the electrolyte. Cyclic voltammetry (CV) was used to determine the electrochemical capacitance of the samples presented in this paper.[2,3] The potential was swept in a range from 0.05 V above the open-circuit potential (OCP) to 0.05V below the OCP in a static solution with five different scan rates: 0.005, 0.01, 0.025, 0.05 and 0.1 V s^{-1}. The working electrode was held for 10 s at each end of the potential sweep before continuing to the next sweep. All experiments were performed at room temperature.

4.3 Results and Discussion

4.3.1 Elements distribution across the $NiCeO_x$ catalyst

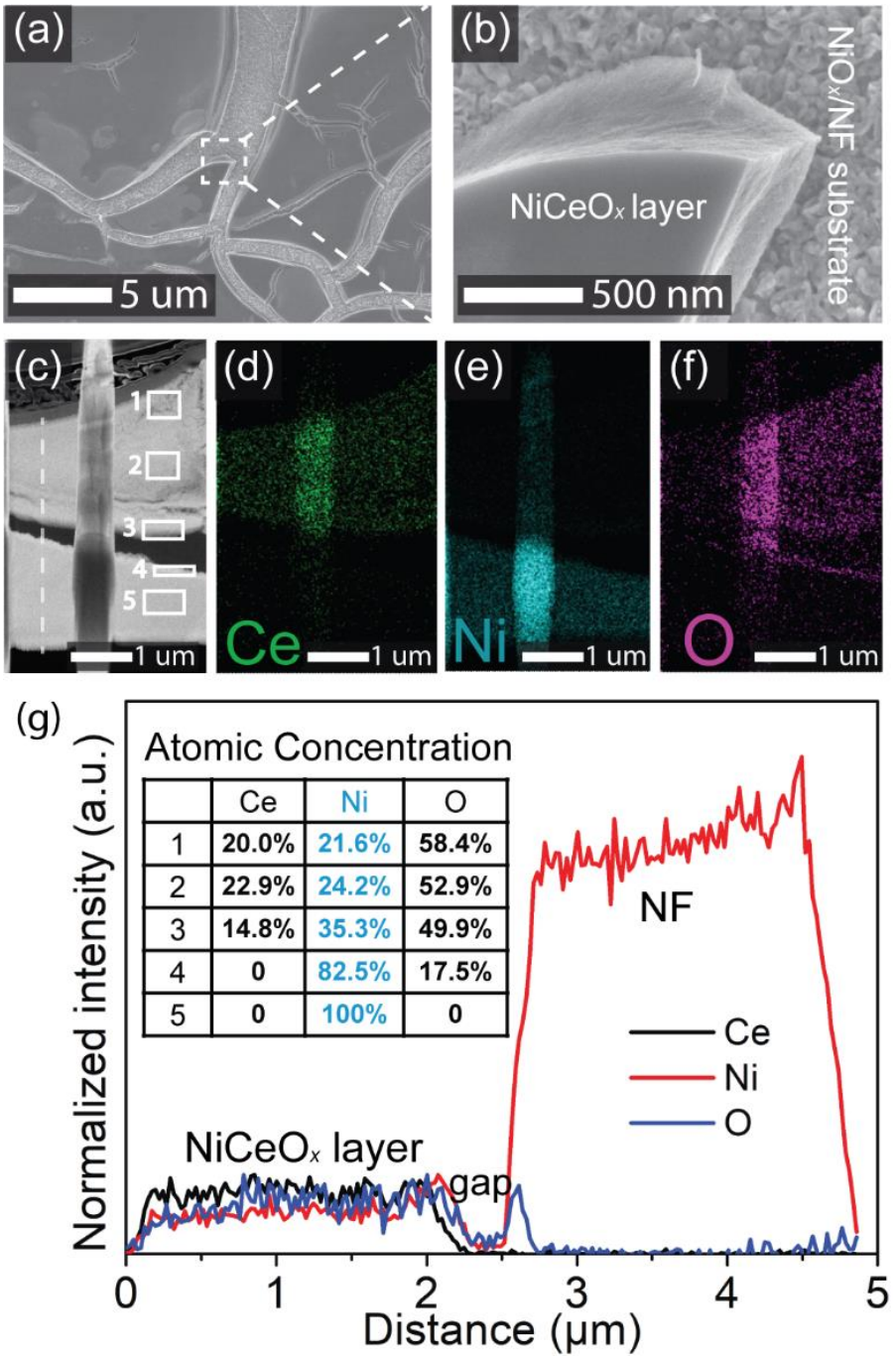

Figure 4.1 (a), (b) SEM images of the $NiCeO_x$ sample with different magnifications; (c)

the cross-sectional STEM image of the top $NiCeO_x$ layer (the upper part) and the NiO_x/NF substrate (the lower part) of the $NiCeO_x$ sample. The dark gap between the $NiCeO_x$ layer and NiO_x/NF substrate was created during the cutting of the cross-section with a FIB and is not present in the original material. Elemental mapping of the STEM image shown in (c) are given for Ce (d), Ni (e) and O (f); (g) elemental line profiles for Ce, Ni and O across a scan line indicated by the dashed white line shown in (c). The inset table shows the elemental composition at the five locations numbered in (c). The resolution of the line EDS is finer than 1 nm.

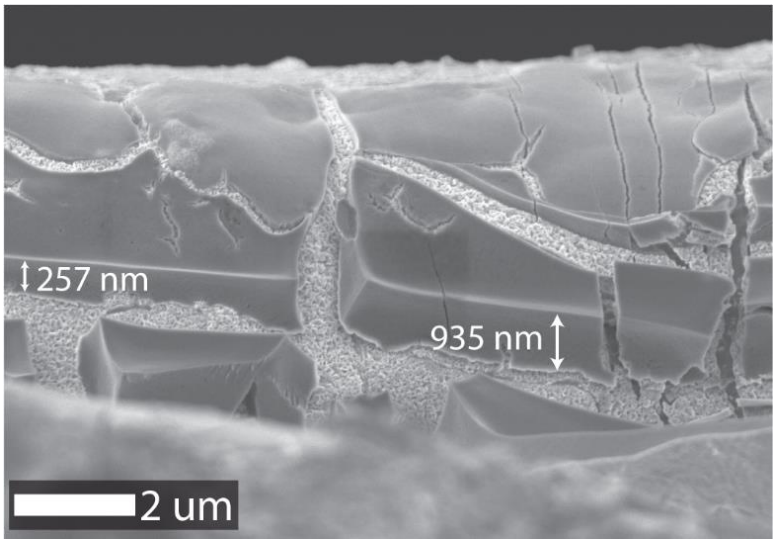

Figure 4.2 The cross-sectional SEM image of the $NiCeO_x$ sample.

The $NiCeO_x$ sample was synthesized by depositing a cerium salt solution on NF (Figure 4.1a) and then annealing the sample in air to form a $NiCeO_x$ layer on top of the NF, as can be seen in Figure 1a. From the cross-sectional SEM image of the sample (Figure 4.2), the thickness of the $NiCeO_x$ layer was found to vary from several hundred nanometers thick to several micrometers thick. Cracks, that are believed to have formed as a result of a combination of thermal stress in the layer and the release of gas produced

by the decomposition of nitrate ions during the annealing process, were also observed. The cracking of the layer resulted in gaps between portions of the layer where the underlying substrate was exposed. Upon SEM characterization of these areas of the substrate (Figure 4.1b), the substrate surface morphology was found to be extremely similar to that of the NiO sample (Figure 3.1).

A cross-sectional STEM image of the $NiCeO_x$ sample, prepared by FIB-TEM, is shown in Figure 4.1c. The upper and lower bright regions in Figure 4.1c represent the $NiCeO_x$ layer and NF/NiO substrate respectively, with the dark region between these two being a gap that was created during the FIB cutting process. STEM EDS was then used to determine elemental composition of the cross-sectional sample. Figures 4.1d, 4.1e and 4.1f illustrate the Ce, Ni and O distribution in the cross-sectional sample. In the top layer, all the three elements (Ce, Ni and O) were detected. Understandably, within the gap only trace amounts of O – from carbonaceous compounds created during the FIB cutting process – are detected. Below the gap, a thin layer (about 100 nm thick) composed of only Ni and O can be observed. The rest of the sample was found to contain only Ni. The above results show that the sample is composed of a $NiCeO_x$ top layer, a thin NiO_x middle layer, and a Ni base layer (the NF substrate). In Figure 4.1g, the concentration of each element as a function of the distance along the dashed line of Figure 4.1c, starting from the top of the $NiCeO_x$ layer, is illustrated. Figure 4.1g shows that although the Ni, Ce and O concentrations remain relatively constant throughout most of the $NiCeO_x$ film, at the interface between the $NiCeO_x$ layer and the NiO_x layer (just before the gap in the graph), the Ni concentration increases while the Ce concentration decreases. This is further supported by the concentration values reported for areas 1, 2 and 3 in the inset table of Figure 4.1g. The elemental concentrations of Ni, Ce and O in areas 1 ($NiCeO_x$ layer

surface), 2 ($NiCeO_x$ layer), 3 (the interface of $NiCeO_x$ and NiO_x layer), 4 (NiO_x layer) and 5 (Ni substrate) of Figure 4.1c are shown in the inset of Figure 4.1g. The distribution of Ni atoms in the $NiCeO_x$ layer, and the increase in the Ni concentration close to the interface suggests that Ni atoms from the substrate diffused into the top layer and mixed with the deposited Ce during the annealing process, resulting in the formation of the $NiCeO_x$ layer.

4.3.2 Structure characterization of the $NiCeO_x$ and NiO/CeO_2 catalysts

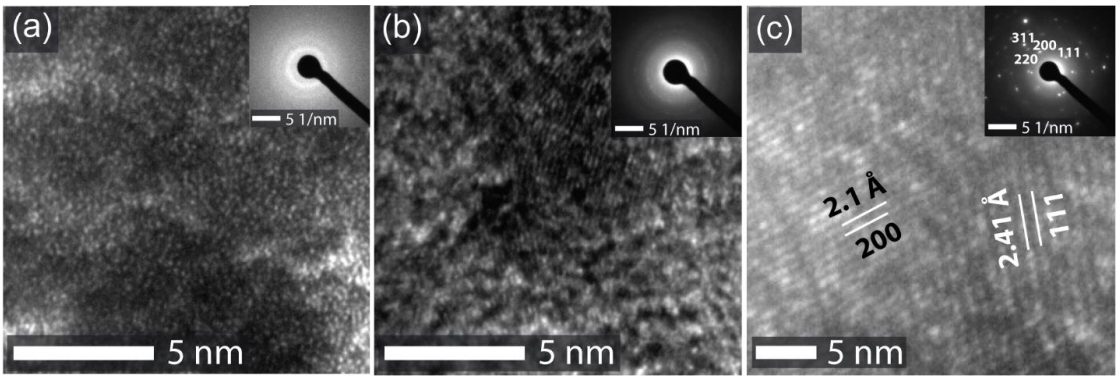

Figure 4.3 HRTEM images of (a) the $NiCeO_x$ layer, (b) the $NiCeO_x/NiO_x$ interface and (c) the NiO_x layer as defined in Figure 1c. Insets show the selected area electron diffraction (SAED) patterns of the area imaged in each HRTEM image.

HRTEM images of the $NiCeO_x$ layer (Figure 4.2a), $NiCeO_x/NiO_x$ interface (Figure 4.2b) and NiO_x layer (Figure 4.2c) were taken, along with an SAED pattern (insets) for each region. Figure 4.2a and the corresponding inset indicate that the $NiCeO_x$ layer is amorphous in structure. Similarly, the interface between the $NiCeO_x$ layer and the NiO_x layer shows no signs of crystallinity. The HRTEM image of the NiO_x layer in Figure 4.2c shows a clear ordered structure, with one inter-planar spacing of 2.1 Å and another inter-

planar spacing of 2.41 Å; these match the inter-planar spacings of the (200) and (111) planes of NiO, respectively. Furthermore, the diffraction spots for the (200), (111), (220) and (311) planes of NiO could be distinguished in the SAED pattern (Figure 4.2c inset), supporting the conclusion that the NiO_x intermediate layer is composed of polycrystalline NiO. The presence of polycrystalline NiO may have formed due to the higher Ni concentration in this layer, which is consistent with the distribution of Ni atoms shown by STEM EDS results. The amorphous structure of $NiCeO_x$ may indicates the uniform mixture of Ni and Ce atoms.

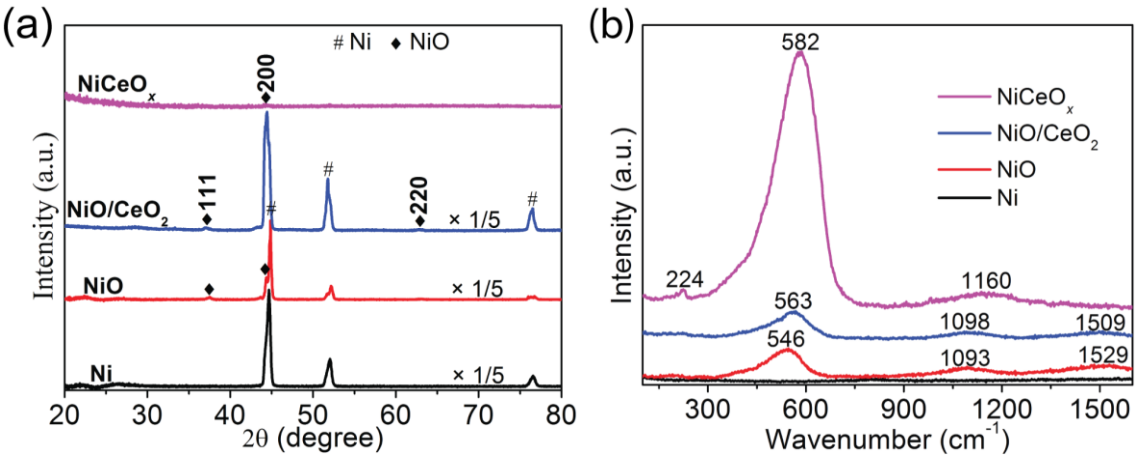

Figure. 4.4 (a) X-ray diffraction patterns and (b) Raman spectra of the Ni, NiO and $NiCeO_x$ samples.

XRD measurements were performed on the Ni, NiO and $NiCeO_x$ samples to examine the crystal structure of the three samples of Ni, NiO and $NiCeO_x$, and are shown in Figure 4.4a. For the Ni sample, only peaks associated with Ni (JCPDS 65-2865) were found. The annealed NiO sample had an additional four peaks, the (111), (200), (220) and (311) peaks, which were attributed to NiO (JCPDS 65-2901). For the $NiCeO_x$ sample, a single weak

peak corresponding to the (200) plane of NiO was found; it is believed that this peak is from the polycrystalline NiO_x intermediate layer. No peaks for ceria were found, suggesting that Ni and Ce mixed uniformly in the top layer and formed an amorphous $NiCeO_x$.

4.3.3 Oxygen vacancies in the $NiCeO_x$ catalyst

Figure 4.4b shows the Raman spectra of the Ni, NiO, NiO/CeO_2 and $NiCeO_x$ samples. The peaks at 546 cm^{-1}, 1093 cm^{-1} and 1511 cm^{-1} in the NiO sample spectrum were attributed to the one-phonon TO/LO mode of NiO, the two-phonon 2LO mode of NiO and the two-magnon mode of NiO, respectively [4]. For the $NiCeO_x$ sample, three peaks of 224 cm^{-1}, 582 cm^{-1} and around 1160 cm^{-1} are observed. Crystalline CeO_2 is known to have a strong F_{2g} Raman peak at 464 cm^{-1} related to its crystalline structure [5]. In addition, the Ce-O bond has a 2LO (second-order longitudinal) mode at 1160 cm^{-1} [5,6]. The presence of ions with the oxidation states lower than Ce^{4+} in the CeO_2 has been shown to induce a Raman band, known as the D band, from 500 to 700 cm^{-1} [5,7,8]. This band is associated with the presence of oxygen vacancy defects created in the non-stoichimometric CeO_{2-y} by the 3+ coordinated ions. In addition to the introduction of the D band, the F_{2g} band will be weakened and becomes asymmetric and broad [9]. In the Raman spectrum of the $NiCeO_x$ sample, there is no F_{2g} band, which suggests that there is no crystalline CeO_2 with a fluorite structure in the layer [6]. The strong intensity of the peak seen at 582 cm^{-1} (D band) indicates the formation of a large number of oxygen vacancy defects within the $NiCeO_x$ layer. The oxygen vacancy defects should be related to the presence of Ce^{3+} because of the incorporation of Ni into CeO_2, as suggested by the literature [5–7]. Furthermore, the amorphous structure of $NiCeO_x$ contributes to the broadness of the peak

[6,9]. The peak at 224 cm^{-1} is related to Ce-OH vibrations which result from surface defects. Different types of hydroxyl groups originate from the dissociation of surface adsorbed water and doubly bridging hydroxyl groups on reduced ceria are detected in the Raman spectra [10,11]. The Raman peak at 1160 cm^{-1} is observed; however, it has a very low intensity compared to the D band. This indicates that the Ce-O bond has been weakened, and suggests that electron transfer from Ni to the Ni-Ce-O bond has occurred [5,6]. The NiO/CeO_2 sample on the other hand, only peaks associated with NiO were observed because NiO substrate disturbed the diffusion of Ni. This clearly demonstrates that the oxygen vacancy defects in $NiCeO_x$ layer are induced by the incorporation of Ni into CeO_2.

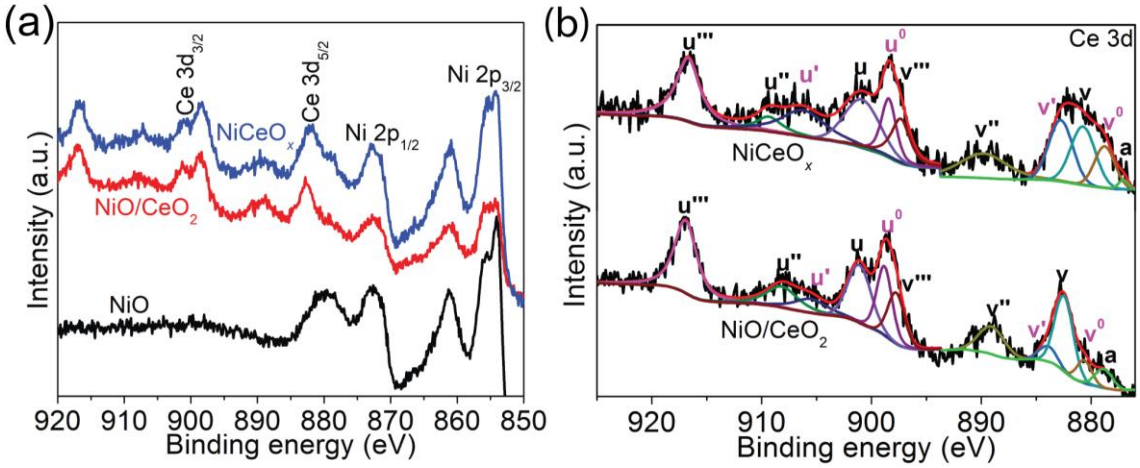

Figure 4.5. (a) XPS spectra of Ce 3d and Ni 2p of NiO, NiO/CeO_2 and $NiCeO_x$. (b) Ce 3d spectra of the NiO/CeO_2 and $NiCeO_x$ samples. The peak labeled *a* in the XPS spectra is ascribed to the Ni 2p peak.

XPS was carried out on NiO, NiO/CeO_2 and $NiCeO_x$ samples to further analyze the electron interactions between nickel and cerium oxide, and the results are shown in Figure 4.5 and Figure 4.4c. The observed XPS peaks in the NiO sample could be attributed to

the Ni $2p_{3/2}$ peak (854.1 eV) and the Ni $2p_{1/2}$ peak (872.5 eV) of NiO.[12] Additional intense satellite peaks (861.3 eV and 879.9 eV) characteristic of NiO were also observed, as shown in Figure 4.5. This confirms that the NiO sample is indeed composed of NiO. In the NiO/CeO_2 sample, a weak Ni 2p signal, associated with NiO, was observed. It is believed that this is due to cracks in the CeO_2 film exposing the underlying NiO. For both the NiO/CeO_2 and $NiCeO_x$ samples, Ce 3d peaks were observed. The Ce 3d band is composed of ten individual peaks, that are labeled on Figure 3c as v, v'', v''', u, u'', u''', v^0, v', u^0 and u'. The v, v'', v''', u, u'' and u''' peaks represent the $3d^{10}4f^0$ state of Ce^{4+}, and the v^0, v', u^0 and u' peaks represent the $3d^{10}4f^1$ state of Ce^{3+}.[12–14] The band energies of v^0, v', u^0 and u' for the NiO/CeO_2 sample are 880.6 eV, 883.9 eV, 898.8 eV and 905.5 eV, and the band energies are 880.5 eV, 883.6 eV, 898.6 eV and 904.9 eV for the $NiCeO_x$ sample. Based on the relative areas of the Ce^{3+} and Ce^{4+} peaks, it was possible to determine that the Ce^{3+} concentration is 24% for NiO/CeO_2 sample and 37% for the $NiCeO_x$ sample. The increase in the concentration of Ce^{3+} is a result of the reduction of Ce^{4+} by the removal of lattice O^{2-} anions through the formation of oxygen vacancy.[13] This, along with the change in the band energies for the $NiCeO_x$ sample, indicates that there are strong electronic interactions between the nickel and cerium oxide in the $NiCeO_x$ sample.[15] This suggests that the electron interactions between the nickel and cerium oxide in $NiCeO_x$ results in Ce^{4+} ions being reduced to Ce^{3+} and the formation of oxygen vacancies.

4.3.4 OER activities of the $NiCeO_x$ and NiO/CeO_2 catalysts

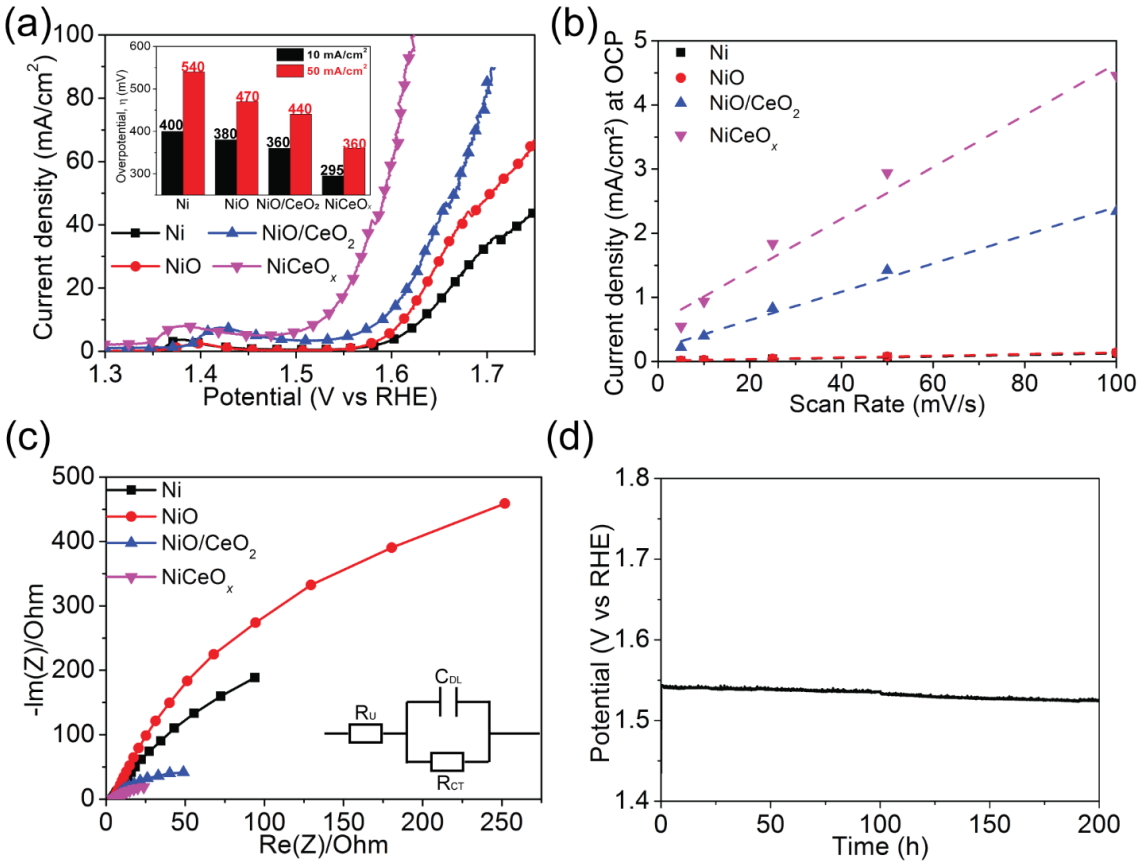

Figure 4.6 (a) Polarization curves of Ni, NiO, NiO/CeO_2 and $NiCeO_x$ samples for the OER with a scan rate of 10 mV s^{-1}. The inset shows the overpotential for a current density of 10 mA/cm^2 (black) and 50 mA/cm^2 (red). (b) Current density at OCP vs CV scan rate for the Ni, NiO, NiO/CeO_2 and $NiCeO_x$ samples. The slope of current density at OCP vs scan rate represents the double-layer capacitance. (c) Nyquist plots of Ni, NiO, NiO/CeO_2 and $NiCeO_x$ samples obtained at 1.50 V vs RHE. The inset shows the electrical equivalent circuit. (d) Potential trace of the $NiCeO_x$ sample obtained by fixing the current density for electrolysis at 10 mA/cm^2. The electrolyte was 1 M KOH (pH ≈ 14).

Table 4.1. Double-layer capacitance (C_{DL}), electrochemically active surface area (ECSA) and mass-transfer resistance (R_{CT}) for each catalyst investigated in 1 M KOH

Catalyst	C_{DL}/cm^2 for OER	ECSA/cm^2 for OER	R_{CT}/Ω
Ni	1.19 mF	29.75	174
NiO	1.31 mF	32.75	370
NiO/CeO_2	10.8 mF	270	36
$NiCeO_x$	40.4 mF	1010	12

To test the electrochemical activity of the samples prepared, the polarization curves of the samples (Figure 4.6a) were obtained using Linear Sweep Voltammetry (LSV). The Ni sample showed the lowest current density for the applied potentials, and had the largest overpotential of 400 mV for the current density of 10 mA/cm^2. The NiO sample exhibited a slightly better performance, with an overpotential of 380 mV for 10 mA/cm^2. The overpotential of 10 mA/cm^2 for NiO/CeO_2 was 360 mV. The best performance was shown by the $NiCeO_x$ sample which had a low overpotential of only 295 mV to obtain the current density of 10 mA/cm^2. The electrochemically active surface area (ECSA) of each sample was estimated by the double-layer capacitance.[2,16] In order to know the double-layer capacitance, we first obtained CV curves of the capacitance current in the non-Faradaic voltage region (a 0.1 V potential range centered on the OCP) for several different scan rates (Figure 4.7). The rate of change in the current at OCP with respect to the scan rate corresponds to the double-layer capacitance.[17] For this reason, the current at OCP was plotted against the scan rate for the four samples, and a line of best fit was fitted for each sample's data set, as shown in Figure 4.6b. The double layer capacitance was 1.19 mF,

1.31 mF, 22.1 mF and 40.4 mF for the Ni, NiO, NiO/CeO_2 and $NiCeO_x$ samples, respectively. The ECSA can be calculated according to the formula $ECSA = C_{DL}/C_s$, where a specific capacitance of $C_s = 0.040$ mF cm^{-2} was used in this work.[2] The calculated ECSA values for the four samples as well as other relevant electrochemistry parameters are summarized in Table 4.1. The ECSA of NiO was found to be only slightly larger than that of Ni, while the ECSA of NiO/CeO_2 was much larger than both. The ECSA of $NiCeO_x$ was nearly 31 times that of NiO and twice that of NiO/CeO_2. This is consistent with the observed current densities ($J_{NiCeOx} >> J_{NiO/CeO2} > J_{NiO} > J_{Ni}$), as a larger ECSA means a sample has more active sites and therefore can catalyze more reactions at once and sustain a large current.

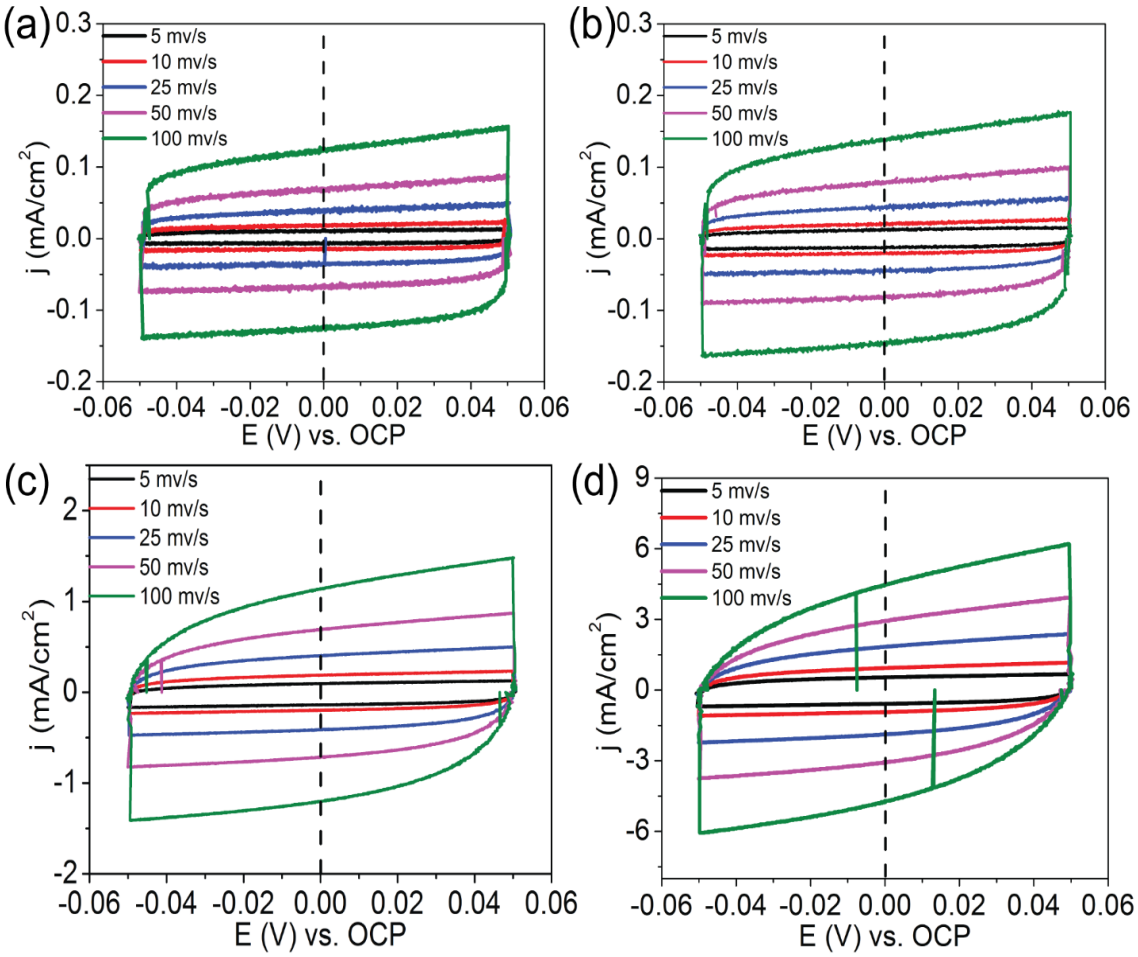

Figure 4.7 Cyclic voltammograms of (a) Ni, (b) NiO, (c) NiO/CeO_2 and (d) $NiCeO_x$ measured in a region with non-Faradaic process of the voltammogram with the scan rates of 5 mv/s, 10 mv/s, 25 mv/s, 50 mv/s and 100 mv/s for OER.

The charge transfer resistances (R_{CT}) of the samples were obtained from their Nyquist plots (Figure 3c). As shown in Table 1, the R_{CT} of NiO/CeO_2 (36 Ω) was much smaller than Ni (174 Ω) and NiO (370 Ω), and $NiCeO_x$ had the smallest R_{CT} of only 12 Ω at an applied bias of 1.5 V vs RHE. The high oxygen storage capacity and good ionic/electronic conductivity of CeO_2 surface layer of NiO/CeO_2 result in the sharp decrease of R_{CT} compared with pure NiO.[15,18,19] The smallest R_{CT} of $NiCeO_x$ indicates the oxygen vacancy defects in CeO_x can further promote the mobility of lattice oxygen and enhance the ionic conductivity.[20] Thus, $NiCeO_x$ has the lowest mass-transfer resistance, suggesting favorable OER kinetics. The strong electronic interactions between nickel and cerium oxide induced the oxygen vacancy defects in $NiCeO_x$, as shown by the XPS and Raman results. The large number of oxygen vacancy defects supply an abundance of electrochemically active OER sites and decrease the mass-transfer resistance, resulting in the large electrochemically active surface area and high OER performance of $NiCeO_x$. When the lower performance of the NiO/CeO_2 sample – which did not show any evidence of defects within the CeO_2 in its Raman spectrum – is considered, the importance of oxygen vacancy defects for Ce-containing in achieving a high OER performance is abundantly clear.

4.3.5 OER stability of the $NiCeO_x$ catalyst

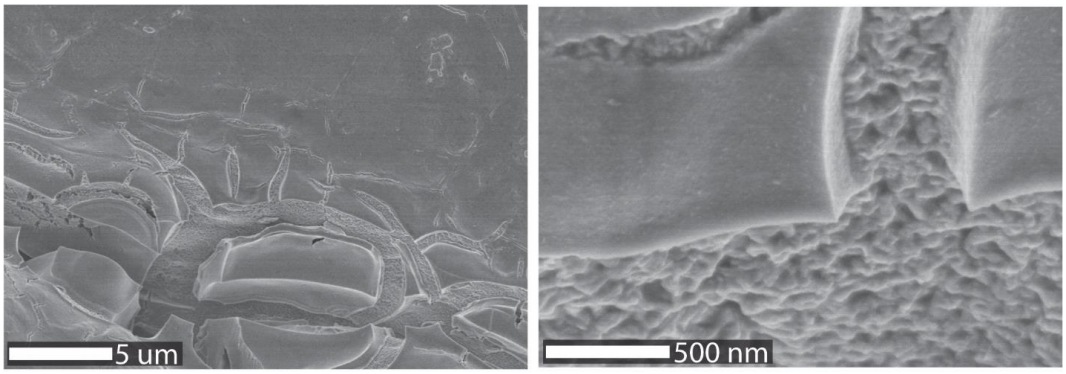

Figure 4.8 SEM images of the $NiCeO_x$ catalyst after 100-hour stability test with the current density of 10 mA/cm^2.

Controlled-current water electrolysis (Figure 4.6d) was performed to test the stability and long-term performance of the $NiCeO_x$ sample. With a fixed current density of 10 mA/cm^2, the potential remained stable at 1.54 V vs RHE for more than 100 h. SEM images of the $NiCeO_x$ sample after the 100-hour stability test are shown in Figure 4.8. The morphology remained nearly the same as the fresh $NiCeO_x$ sample. The OER performance of $NiCeO_x$ compared to that of other OER metal oxide catalysts reported recently (Table 4.2), including precious metals, Ni-based and Co-based catalysts. In addition to the $NiCeO_x$ having an initial activity and the activity after a 100-hour continuous test comparable to that of other OER metal oxide catalysts, the $NiCeO_x$ sample outperforms other metal oxide catalysts in terms of stability. $NiCeO_x$-Au (Ni:Ce 95: 5) was reported to have a low overpotential of 280 mV for a current density of 10 mA/cm^2, but the overpotential increased with the testing time and end up with 310 mV during a 2-hour stability test [14]. The long-time stability (over 100 h) of our $NiCeO_x$ sample may be attributed to the high Ce concentration (Ni:Ce 52:48) and the synthesis method (NF substrate as the source of nickel). It is noted that the overpotential for 10 mA/cm^2 was above 470 mV for the reported $NiCeO_x$-Au (Ni:Ce 50:50). The low overpotential (295 mV) of our $NiCeO_x$ sample is attributed to the large number of active sites induced by the

abundant oxygen vacancy defects. The low overpotential and long-term stability of $NiCeO_x$ achieved in this work make it an ideal OER catalyst.

Table 4.2. Overpotential (η) and the testing time (T) of stability at the current density of 10 mA/cm^2 of recently reported metal oxide catalysts for OER. Metal oxide catalysts are listed below when a stability test is available.

catalyst	$\eta_{t=0}$/V	T/h	$\eta_{t=T}$/V	Electrolyte	Ref.
NF/$NiCeO_x$	0.31	100	0.31	1 M KOH	This work
IrO_x	0.32	2	1.05	1 M NaOH	2
IrO_2-(i)	0.38	2	0.43	1 M NaOH	25
RuO_2	0.38	2	0.43	1 M NaOH	25
Ru-(a)	0.29	2	0.32	1 M NaOH	26
NF/NC-IrO_2	0.31	30	0.32	1 M KOH	27
NiO_x	0.42	2	0.41	1 M NaOH	2
NiO-(i)	0.43	2	0.42	1 M NaOH	25
$NiCeO_x$	0.43	2	0.44	1 M NaOH	2
$NiCeO_x$-Au	0.28	2	0.31	1 M NaOH	14
$NiCoO_x$	0.38	2	0.36	1 M NaOH	2
$NiCuO_x$	0.41	2	0.44	1 M NaOH	2
$NiFeO_x$	0.35	2	0.38	1 M NaOH	2
$Ni_yFe_{1-y}O_x$/C	0.28	6	0.28	0.1 M KOH	28
$NiLaO_x$	0.41	2	0.46	1 M NaOH	2
$LiNiO_2$	0.41	2	0.39	1 M NaOH	25
$LaNiO_3$	0.45	2	0.55	1 M NaOH	25
$NiCoO_2$	0.39	2	0.44	1 M NaOH	25
$NiFe_2O_4$	0.51	2	1.27	1 M NaOH	25
Ni-Co oxide	0.37	2.8	0.38	1 M NaOH	29
CoO_x-(a)	0.39	2	0.42	1 M NaOH	2
CoO_x-(b)	0.42	2	0.44	1 M NaOH	2
CoO	0.45	2	0.58	1 M NaOH	25
Co_3O_4	0.50	2	0.52	1 M NaOH	25
Porous Co_3O_4	0.52	2.3	0.52	1 M KOH	30
Co_3O_4/MCNT	0.41 V at 20 mA/cm^2 for 2.5 h			1 M KOH	31
Co_3O_4/C nanowires	0.29	30	0.31	0.1 M KOH	32

$Au/NiCo_2O_4$	0.36	2	0.36	1 M KOH	33
CoO/N-doped graphene	0.34	2	0.38	1 M KOH	34
$LiCoO_2$	0.47	2	0.50	1 M NaOH	25
$CoCr_2O_4$	0.38	2.8	0.56	1 M KOH	35
$CoCr_2O_4$/CNS	0.35	2.8	0.39	1 M KOH	35
$Zn_xCo_{3-x}O_4$	0.32	2	0.32	1 M KOH	36
Fe_2O_3	1.24	2	1.28	1 M NaOH	25
NF@NC-$CoFe_2O_4$/C NRAs	0.24	30	0.24	1 M KOH	27
NF@NC-$CoFe_2O_4$/C	0.32	30	0.32	1 M KOH	27
NF@NC-$CoFe_2O_4$	0.35	30	0.36	1 M KOH	27
Mn_3O_4	0.43	2	0.42	1 M NaOH	25

4.3.6 Overall water electrolysis activity of the $NiCeO_x$ catalyst

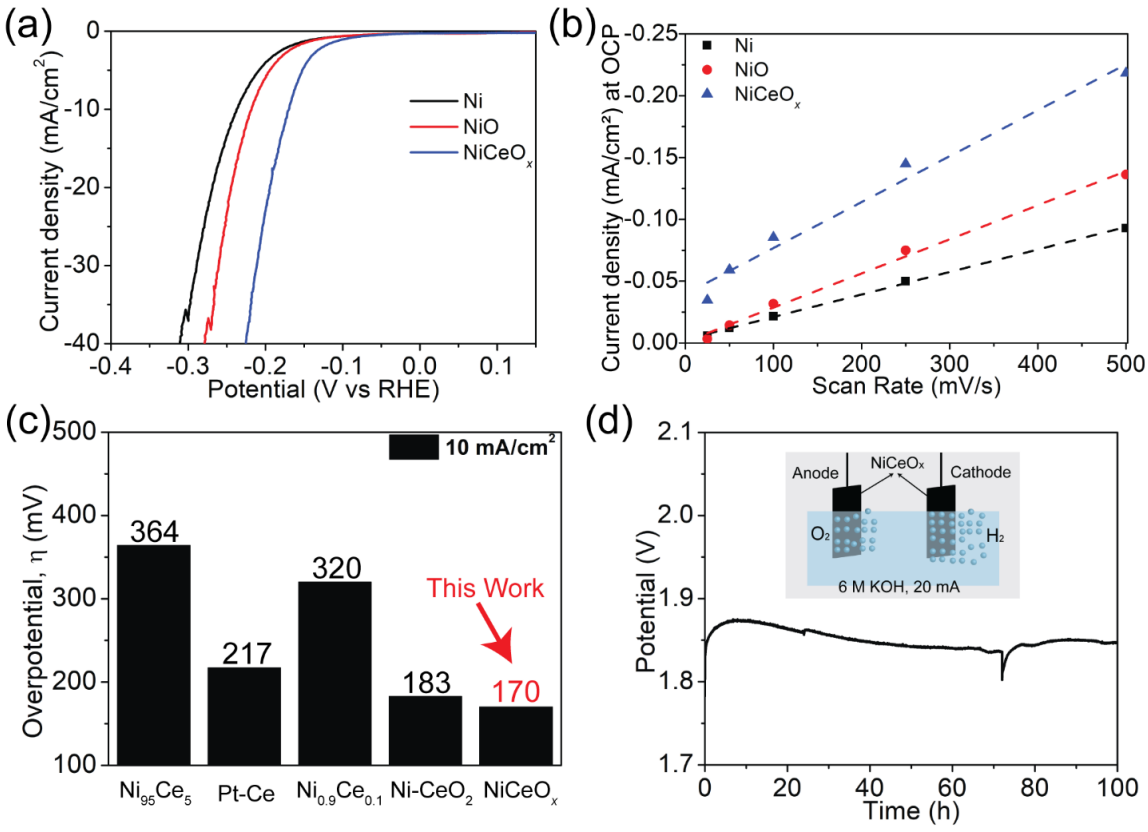

Figure 4.9 (a) Polarization curves for HER with a scan rate of 10 mV s^{-1} and (b)

current density at OCP vs scan rate for Ni, NiO and $NiCeO_x$ (1 M KOH electrolyte with a pH ≈ 14). (c) Comparison of the HER performance of the $NiCeO_x$ sample to the reported cerium-based catalysts.[18–21] 320 mV is the overpotential for the current density of 1.5 mA/cm^2 for $Ni_{0.9}Ce_{0.1}$. (d) Performance of the electrolyser held at 20 mA/cm^2 for 100 h at room temperature. The electrolyte was changed at 72h, resulting in a slight dip in the performance. Inset: schematic of the two-electrode configuration, which uses the same $NiCeO_x$ sample as the anode and cathode in a 6 M KOH solution.

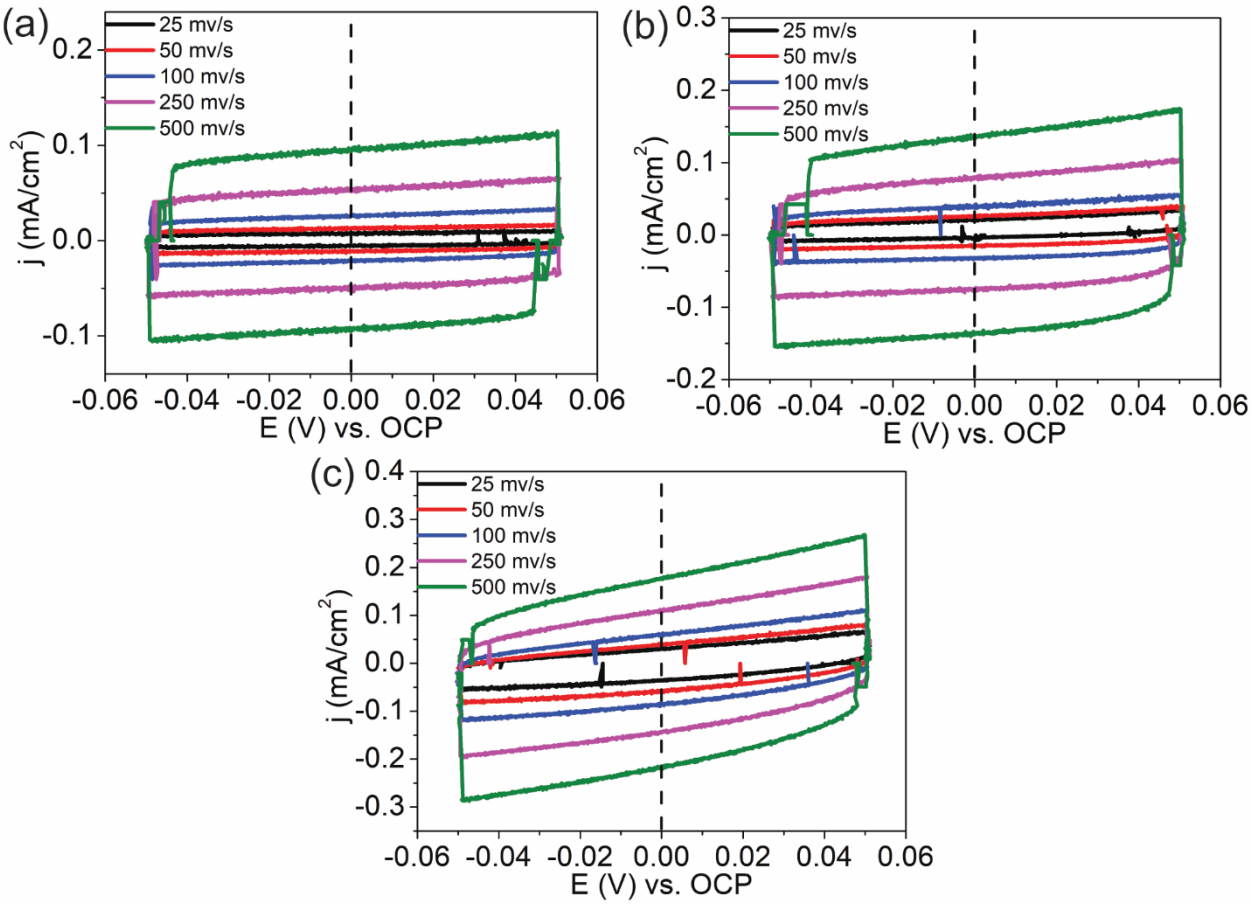

Figure 4.10 Cyclic voltammograms of (a) Ni, (b) NiO and (c) $NiCeO_x$ were measured in a region with non-Faradaic process of the voltammogram with the scan rates of 25 mv/s, 50 mv/s, 100 mv/s, 250 mv/s and 500 mv/s for HER.

Table 4.3. Double-layer capacitance (C_{DL}) and electrochemically active surface

area (ECSA) for Each Catalyst Investigated in 1 M KOH

Catalyst	C_{DL}/cm^2 for HER	ECSA/cm^2 for HER
Ni	0.182 mF	4.55
NiO	0.276 mF	6.90
$NiCeO_x$	0.371 mF	9.28

To determine if the $NiCeO_x$ would be suitable as a bifunctional catalyst for the full water-splitting reaction, the HER performances of the Ni, NiO and $NiCeO_x$ samples were further tested. As shown in Figure 4.9a, the hydrogen evolution ability of $NiCeO_x$ sample was the best among the three samples. The overpotential for a current density of 10 mA/cm^2 was 237 mV, 218 mV and 170 mV for the Ni, NiO and $NiCeO_x$ samples, respectively. The slopes of the curves in Figure 4.9b represent the double-layer capacitances of the samples, and from it the ECSA of each sample can be calculated. The ECSA values of the three samples are listed in Table 4.3. The ECSA of the NiO sample was slightly larger than that of the Ni sample and the ECSA value of the $NiCeO_x$ sample was much larger than the other two. This is consistent with the measured electrocatalytic activity of the three samples. The HER performance of the $NiCeO_x$ is compared to that of the other Ce based catalysts reported in the literature, as shown in Figure 4.9c.[21–24] For a current density of 10 mA/cm^2, the overpotential of $NiCeO_x$ (our sample) was the lowest among the reported results and even lower than one using a precious metal (Pt-Ce). Finally, $NiCeO_x$ was used as both the anode and cathode in a two-electrode configuration to test the overall water splitting ability of the catalyst (Figure 4.9d). During a 100-hour water electrolysis test in a 6 M KOH electrolyte, with a fixed current of 20 mA/cm^2, the potential increased slightly before stabilizing at around 1.85 V. This result indicates $NiCeO_x$ is a stable overall water splitting catalyst, and $NiCeO_x$ is the first reported Ce-based bifunctional electrocatalyst for overall water splitting.

4.4 Conclusion

In summary, an amorphous $NiCeO_x$ layer was synthesized on nickel foam directly using a simple two-step dip-coating/annealing method. Ni atoms from the nickel foam substrate transfer to the top layer and mix with deposited Ce to form an amorphous $NiCeO_x$ layer. The electronic interactions between the Ni atoms and cerium oxide results in a oxygen vacancy-rich $NiCeO_x$ layer that has a very high electrochemically active surface area and a low mass-transfer resistance, resulting the high OER performance. The $NiCeO_x$ catalyst, with the low overpotential of 295 mV for 10 mA/cm^2 and the stability of over 100 hours, outperforms the listed benchmark precious metal, Ni-based and Co-based catalysts. This makes it one of the best OER catalysts ever reported. The excellent performance and low-cost, environmentally friendly and reproducible synthesis method of $NiCeO_x$ catalyst make it suitable for industry application. In addition, the HER activity of $NiCeO_x$ is the best among the reported Ce-based catalysts, including Pt-Ce. The stable performance of the $NiCeO_x$ catalyst in a two-electrode configuration suggests it is a good candidate as a bifunctional catalyst for the overall water splitting. This work opens a way to develop Ce-based OER catalysts with high efficiency and stable performance by introducing defects. Ce-based catalysts have the potential to be robust bifunctional catalysts for overall water splitting.

References

1 N. Ozera, J. P. Cronin and S. Akyuza, 1999, **3788**, 195–214.

2 C. C. L. McCrory, S. Jung, J. C. Peters and T. F. Jaramillo, *J. Am. Chem. Soc.*, 2013, **135**, 16977–16987.

3 C. Fisica and U. Milano, *Pure Appl. Chem.*, 1991, **63**, 711–734.

4 N. Mironova-Ulmane, A. Kuzmin, I. Steins, J. Grabis, I. Sildos and M. Pärs, *J. Phys. Conf. Ser.*, 2007, **93**, 012039.

5 T. Taniguchi, T. Watanabe, N. Sugiyama, A. K. Subramani, H. Wagata, N. Matsushita and M. Yoshimura, *J. Phys. Chem. C*, 2009, **113**, 19789–19793.

6 L. He, B. Liang, L. Li, X. Yang, Y. Huang, A. Wang, X. Wang and T. Zhang, *ACS Catal.*, 2015, **5**, 1623–1628.

7 M. Guo, J. Lu, Y. Wu, Y. Wang and M. Luo, *Langmuir*, 2011, **27**, 3872–3877.

8 A. Nakajima, A. Yoshihara and M. Ishigame, *Phys. Rev. B*, 1994, **50**, 13297–13307.

9 J. E. Spanier, R. D. Robinson, F. Zhang, S.-W. Chan and I. P. Herman, *Phys. Rev. B*, 2001, **64**, 245407.

10 A. Filtschew, K. Hofmann and C. Hess, *J. Phys. Chem. C*, 2016, **120**, 6694–6703.

11 A. Badri, C. Binet and J. Lavalley, *J. Chem. Soc. Faraday Trans.*, 1996, **92**, 4669–4673.

12 J. Chastain, R. C. King and J. F. Moulder, *Handbook of X-ray photoelectron spectroscopy: a reference book of standard spectra for identification and interpretation of XPS data*, Physical Electronics Eden Prairie, MN, 1995.

13 J. Yu, Z. Si, L. Chen, X. Wu and D. Weng, *Appl. Catal. B Environ.*, 2015, **163**, 223–232.

14 J. W. D. Ng, M. García-Melchor, M. Bajdich, P. Chakthranont, C. Kirk, A. Vojvodic and T. F. Jaramillo, *Nat. Energy*, 2016, **1**, 16053.

15 J.-X. Feng, S.-H. Ye, H. Xu, Y.-X. Tong and G.-R. Li, *Adv. Mater.*, 2016, **28**, 4698–4703.

16 J. D. Benck, Z. Chen, L. Y. Kuritzky, A. J. Forman and T. F. Jaramillo, *ACS Catal.*, 2012, **2**, 1916–1923.

17 Y. Q. Gao, H. B. Li and G. W. Yang, *J. Appl. Phys.*, 2016, **119**, 034902.

18 Y.-R. Zheng, M.-R. Gao, Q. Gao, H.-H. Li, J. Xu, Z.-Y. Wu and S.-H. Yu, *Small*, 2015, **11**, 182–188.

19 X. Long, H. Lin, D. Zhou, Y. An and S. Yang, *ACS Energy Lett.*, 2018, **3**, 290–296.

20 F. Esch, S. Fabris and L. Zhou, *Science*, 2005, **309**, 752–755.

21 F. Rosalbino, G. Borzone, E. Angelini and R. Raggio, *Electrochim. Acta*, 2003, **48**, 3939–3944.

22 D. M. F. Santos, C. A. C. Sequeira, D. Macciò, A. Saccone and J. L. Figueiredo, *Int. J. Hydrogen Energy*, 2013, **38**, 3137–3145.

23 D. M. F. Santos, L. Amaral, B. Sljukic, D. Maccio, A. Saccone and C. A. C. Sequeira, *J. Electrochem. Soc.*, 2014, **161**, F386–F390.

24 Z. Chen, Z. Ma, J. Song, L. Wang and G. Shao, *RSC Adv.*, 2016, **6**, 60806–60814.

25 S. Jung, C. C. L. McCrory, I. M. Ferrer, J. C. Peters, T. F. Jaramillo, J. Mater. Chem. A 2016, 4.

26 C. C. L. McCrory, S. Jung, I. M. Ferrer, S. M. Chatman, J. C. Peters, T. F. Jaramillo, J. Am. Chem. Soc. 2015, 137, 4347–4357.

27 X.-F. Lu, L.-F. Gu, J.-W. Wang, J.-X. Wu, P.-Q. Liao, G.-R. Li, Adv. Mater 2017, 29, 1604437.

28 Y. Qiu, L. Xin, W. Li, Langmuir 2014, 30, 7893.

29 Y. Yang, H. Fei, G. Ruan, C. Xiang, J. M. Tour, ACS Nano 2014, 8, 9518.

30 X. Zhou, Z. Xia, Z. Tian, Y. Ma, Y. Qu, J. Mater. Chem. A 2015, 3, 8107.

31 Y.-X. Zhang, X. Guo, X. Zhai, Y.-M. Yan, K.-N. Sun, J. Mater. Chem. A 2015, 3, 1761.

32 T. Y. Ma, S. Dai, M. Jaroniec, S. Z. Qiao, J. Am. Chem. Soc. 2014, 136, 13925.

33 X. Liu, J. Liu, Y. Li, Y. Li, X. Sun, ChemCatChem 2014, 6, 2501.

34 S. Mao, Z. Wen, T. Huang, Y. Hou, J. Chen, Energy Environ. Sci. 2014, 7, 609.

35 M. Al-Mamun, X. Su, H. Zhang, H. Yin, P. Liu, H. Yang, D. Wang, Z. Tang, Y. Wang, H. Zhao, Small 2016, 12, 2866–2871.

36 X. Liu, Z. Chang, L. Luo, T. Xu, X. Lei, J. Liu, X. Sun, Chem. Mater 2014, 26, 1889-1895.

5. Conclusions

The research goal of the work in the thesis is about the synthesis of a noble-metal free water electrolysis catalyst with high activity and long-term stability in a simple method. Ni-based catalysts are considered as the good candidates for noble-metal oxygen evolution catalysts because their good activities and low cost. Defects can improve the OER performance of an electrocatalyst, and oxygen vacancy defects are easily formed in Ce-based catalysts. Therefore, we plan to combine the advantages of Ni- and Ce-based catalysts by designing the Ni and Ce mixed oxide ($NiCeO_x$) catalyst to achieve the research goal.

Firstly, a series of $Ni_yCe_{100-y}O_x$ ($Ni_{95}Ce_5O_x$, $Ni_{90}Ce_{10}O_x$, $Ni_{75}Ce_{25}O_x$, $Ni_{50}Ce_{50}O_x$, $Ni_{25}Ce_{75}O_x$ and $Ni_{10}Ce_{90}O_x$) with different Ni/Ce ratio are synthesized on NF (Nickel Foam)/NiO substrate with simple dip-coating and annealing methods. Oxygen vacancy defects are formed successfully in all the NF/NiO/$Ni_yCe_{100-y}O_x$ (simply referred to $Ni_yCe_{100-y}O_x$) catalysts. The concentration of oxygen vacancy defects for $Ni_{75}Ce_{25}O_x$ and $Ni_{50}Ce_{50}O_x$ catalysts are larger than other $Ni_yCe_{100-y}O_x$ catalysts, resulting in the lower Tafel slope, larger ECSAs, lower charge-transfer resistance and higher OER activities of these two catalysts.

Secondly, NF is used directly as the substrate instead of NF/NiO in order to simplify the synthesis process and reduce the material costs. A series of $NiCeO_x$ with different dip-coating times ($NiCeO_x$-Y) are synthesized directly on commercially available nickel foam (NF) using a simple, low-cost, environmentally friendly and reproducible synthesis method that consists of first dip-coating the NF in a cerium pre-cursor and then annealing

the sample at 400 °C. With the dip-coating times increasing from 1 to 15, the thickness of the surface layer, the concentration of formed oxygen vacancy defects and the OER performance remain constant increasing for $NiCeO_x$-Y catalysts. For the $NiCeO_x$-20 catalyst, the increased Ce content leads to the decrease of the oxygen vacancy defects, resulting in the lower OER performance than the $NiCeO_x$-15 catalyst. The $NiCeO_x$-15 shows the best OER performance with the lowest overpotential of 295 mV for 10 mA/cm^2, and the applied potential remains constant for over 100 h for the fixed current density of 10 mA/cm^2.

Finally, the reason of the formation of the oxygen vacancy-rich $NiCeO_x$ top layer in the $NiCeO_x$ (simply referred to $NiCeO_x$-15) catalyst has been studied in detail. Ni atoms from the nickel foam substrate transfer to the top layer and mix with deposited Ce uniformly to form an amorphous $NiCeO_x$ layer through thermal diffusion. The strong electronic interactions between nickel and cerium oxide induced the oxygen vacancy defects in $NiCeO_x$. The large number of oxygen vacancy defects supply an abundance of electrochemically active OER sites, resulting in the large electrochemically active surface area (ca. 34 times that of NF). The oxygen vacancy defects also promote the mobility of lattice oxygen and enhance the ionic conductivity, resulting in the low mass-transfer resistance of $NiCeO_x$. These bring in the high OER performance of $NiCeO_x$. The excellent performance and low-cost, environmentally friendly and reproducible synthesis method of $NiCeO_x$ catalyst make it suitable for industry application. In addition, the HER (hydrogen evolution reaction) activity of $NiCeO_x$ is the best among the reported Ce-based catalysts, including Pt-Ce. The stable performance of the $NiCeO_x$ catalyst in a two-electrode configuration suggests it is a good candidate as a bifunctional catalyst for the overall water splitting. This work might open a new avenue for developing Ce-based

OER catalysts with high efficiency and stable performance by introducing defects. Nickel foam can be used directly as the source of nickel for the synthesis of Ni-based catalysts through the thermal diffusion of Ni atoms.

List of publications

Journal papers

1. **Jun Yu**, Qi Cao, Yanbo Li, Changli Li, Li Zhang, J. Kenji Clark, Mamiko Nakabayashi, Naoya Shibata, Jean-Jacques Delaunay*. *Defect-rich $NiCeO_x$ electrocatalyst with ultrahigh stability and low overpotential for water oxidation.* ACS Catalysis (submitted).

2. **Jun Yu**, Qi Cao, Bin Feng, Changli Li, Jingyuan Liu, J. Kenji Clark, Jean-Jacques Delaunay*. *Insights into the efficiency and stability of Cu-based nanowires for electrocatalytic oxygen evolution*. Nano Research (*2018*). DOI: 10.1007/s12274-018-2020-1.

3. Qi Cao, **Jun Yu**, Kaiping Yuan, Miao Zhong, Jean-Jacques Delaunay*. *Facile and large-area preparation of porous Ag_3PO_4 photoanodes for enhanced photoelectrochemical water oxidation*. Applied Materials & Interfaces *2017*, 23, 19507-19512.

4. Mohammad Hassan Mirfasih, Changli Li, Ahmad Tayyebi, Qi Cao, **Jun Yu**, Jean-Jacques Delaunay*. *Oxygen-vacancy-induced photoelectrochemical water oxidation by platelike tungsten oxide photoanodes prepared under acid-mediated hydrothermal treatment conditions.* RSC Advances *2017*, 43, 26992-27000.

Appendix. Cu-based nanowires for electrocatalytic oxygen evolution

6.1 Introduction

A wide range of environmental problems, such as acid rain and the greenhouse effects, are exacerbated by the ongoing use of fossil fuels [1–4]. Water splitting is regarded as a potential way to produce hydrogen energy, which is an alternative to fossil fuels. The demand for clean and sustainable energy has inspired researchers to focus on water splitting technology. The oxygen evolution reaction (OER) is a crucial step in the water splitting reaction due to its more complex and sluggish reaction dynamics [5–9]. For many years, researchers have been endeavoring to find suitable anode materials for the OER. An ideal anode material should have a small overpotential, have a high efficiency, be abundant in the earth, and most importantly have long-term stability [10,11]. Till now, Co-[12–16] and Ni-[17–19] based electrodes have been studied broadly for use in OER because of their high activity and good stability. However, the high performance is usually achieved in combination with other materials or by using substrates with large surface areas. This increases the complexity of the fabrication of the electrodes, and their costs.

Cu-based catalysts [20–26] have been widely used to solve environmental and energy related problems. In particular, Cu_2O has been widely studied as a potential low-cost catalyst for solar H_2 generation [27–29]. The first time a copper-based catalyst was applied to electrolytic water oxidation was in 2012, when a copper-bipyridine catalyst was reported [30]. Following this, the role of Cu(II) ions in water oxidation was

investigated thoroughly [10,31], and it was shown that water can be oxidized by Cu(II) ions dissolved in weakly basic electrolytes [31]. Anodic corrosion of the copper electrode could be prevented by the formation of a compact film directly from the Cu(II) in the electrolyte. However, the improved performance required the addition of Cu(II) ions into the electrolyte [10,32]. To solve this problem, copper oxide (Cu-Bi thin film) was synthesized and used for water oxidation. This catalyst sustained a steady current density of 1.2 mA/cm^2 (overpotential η = 660 mV) for 11 h [32] and did not require the addition of extra Cu(II) ions. However, the relatively low current density and high overpotential of the catalyst are unsatisfactory. The poor water oxidation performance of these Cu-based catalysts may be caused by a lack of the active species in the Cu-based catalysts. Recently, $Cu(OH)_2$ was reported to be active for the OER in a 0.1 M NaOH electrolyte [33]. However, the $Cu(OH)_2$ material is not stable in a high pH solution and the morphology of the electrode after stability test was not displayed in the report. A solid understanding of the behavior of Cu-based materials during the OER process remains elusive: it is unclear which phase is the dominant active phase in Cu-based catalysts and what governs the stability of Cu-based catalysts.

In this work, the OER activities of $Cu(OH)_2$, Cu_2O, Cu_xO and CuO nanowires with varying degrees of crystallinity are investigated. CuO is found to be the active phase for the OER, and increasing crystallinity could improve the catalytic activity. A sample with highly crystalline CuO nanowires achieves the best performance with a Tafel slope of 41 mV/decade, an overpotential (η) of ~ 500 mV at ~ 10 mA/cm^2 (without compensation for the solution resistance), and nearly 100% faradaic efficiency in a weakly basic Na_2CO_3 solution (pH 10.8). Moreover, the current density of the electrode remains constant at ~ 10 mA/cm^2 for more than 15 h. The evolution of the chemical states and morphological

structure of the CuO electrode during and after the stability test is revealed and discussed, providing direct evidence of the stability of the CuO electrode. To the best of our knowledge, the CuO nanowires catalyst reported here has one of the best performances reported so far among the OER catalysts in weakly basic electrolytes.

6.2 Experimental Section

Sample Synthesis

$Cu(OH)_2$ nanowires were directly grown from a copper foil using a simple wet chemistry method [34]. First, the copper foil (99.6%, Nilaco) with a size of 10 × 10 mm^2 and a thickness of 0.2 mm was cleaned in an ultrasonic bath for 5 min with acetone first and then ethanol. The foil was then rinsed three times with deionized water. Afterwards, the cleaned copper foil was treated by submersion in a mixture of 2.67 M NaOH (97.0%, Wako) and 0.133 M $(NH_4)_2S_2O_8$ (98.0%, Wako) kept at 5 °C for 15 min. Finally, the copper foil showing a blue color was picked up from the solution, washed by deionized water, and dried in air.

Cu_xO nanowire layers were synthesized from as-prepared $Cu(OH)_2$ nanowires, *via* a two-step annealing process. $Cu(OH)_2$ nanowire layers were thermally treated at 120 °C for 2 h, and subsequently heated in air to either 150, 180, 210, or 250 °C for 3 h, with a heating rate of 5 °C/min. The samples were named according to the annealing temperature used in the second step (*i.e.* the A-150, A-180, A-210 and A-250 samples).

Structural Characterization

Scanning electron microscope (SEM) measurements were carried out on a field emission SEM (JEOL JSM 7600 performed using an X-MAX 100TLE SDD detector (Oxford Instruments). Scanning electron microscope (SEM) images were obtained from a field-emission SEM (JEOL JSM 7600 FA, Japan). Grazing incidence X-ray diffraction (XRD) patterns were recorded on an X-ray diffractometer (SmartLab, Rigaku Co. Ltd, Japan) with Cu Kα radiation (incident angle = 0.5°, λ = 1.541 Å, step size = 0.02 °,

dwelling time = 2 s). Raman spectra were collected on a Renishaw inVia^{TM} Raman Microscope system with a 488 nm excitation laser (0.82 mW) directed through a × 100 objective at room temperature. X-ray photoelectron spectroscopy (XPS) studies were carried out on a PHI 5000 VersaProbe (ULVAC-PHI) with an Al-Kα X-ray source (1486.6 eV). The electron analyzer was operated at pass energies of 117.4 eV for the wide scans and 23.5 eV for the narrow scans. Transmission electron microscopy (TEM) and high-angle annular dark-field (HAADF)-scanning transmission electron microscopy (STEM) observations were carried out with a JEM-2010 TEM (JEOL Co. Ltd., Japan) and an ARM-200CF TEM (JEOL Co. Ltd., Japan) operated at 200 kV, respectively. The HAAD-STEM observations were acquired with a probe-forming aperture semi-angle of 22 mrad and a detection angle of 90-370 mrad.

Electrochemical Measurements

Electrochemical measurements were conducted in a cylindrical glass cell with a standard three-electrode configuration. The electrochemical measurements were conducted in a cylindrical glass cell with a typical three-electrode configuration. The fabricated nanowire electrodes were used as the working electrode, and the reference electrode and counter electrode were a Ag/AgCl electrode and a Pt wire, respectively. The applied potential of the working electrode was controlled using a potentiostat (VersaSTAT 4, Princeton Applied Research). The potentials *vs.* Ag/AgCl reference electrode were converted to the reversible hydrogen electrode (RHE) using the Nernst's equation ($E_{RHE} = E_{Ag/AgCl} + 0.059\ pH + E^0_{Ag/AgCl}$), where $E_{Ag/AgCl}$ is the measured potential against the reference electrode and $E^0_{Ag/AgCl} = 0.1976$ V at 25 °C. The current density (J)–potential (V) curves and Tafel plots were obtained using controlled potential electrolysis in 1 M

Na_2CO_3 (pH 10.8), with a scan rate of 50 mV s^{-1} for the *J–V* curve and a scan rate of 1 mV s^{-1} for Tafel plot. Prior to each experiment, the electrolyte was stirred and purged with N_2 gas for 20 min. N_2 purging was continued in throughout the electrochemical measurements. The *iR* drop of the Tafel plots were corrected for the solution resistance, which was determined using the electrochemical impendence spectroscopy (EIS) technique [8]. EIS measurements were conducted in the same configuration as the other electrochemical measurements and under the potential corresponding to the current density of 10 mA/cm^2, with the frequency ranging from 100 kHz to 1 Hz. Unless otherwise stated, all the potentials were reported *vs*. RHE without *iR* compensation and all experiments were performed at room temperature. An on-line micro-gas chromatograph (GC-3000A, Agilent) was used to record the amounts of generated O_2 and H_2 during the water oxidation reaction. The faradaic efficiency was calculated according to the ratio of the number of electrons in the detected oxygen/hydrogen molecules to the number of electrons injected by the current.

6.3 Results and Discussion

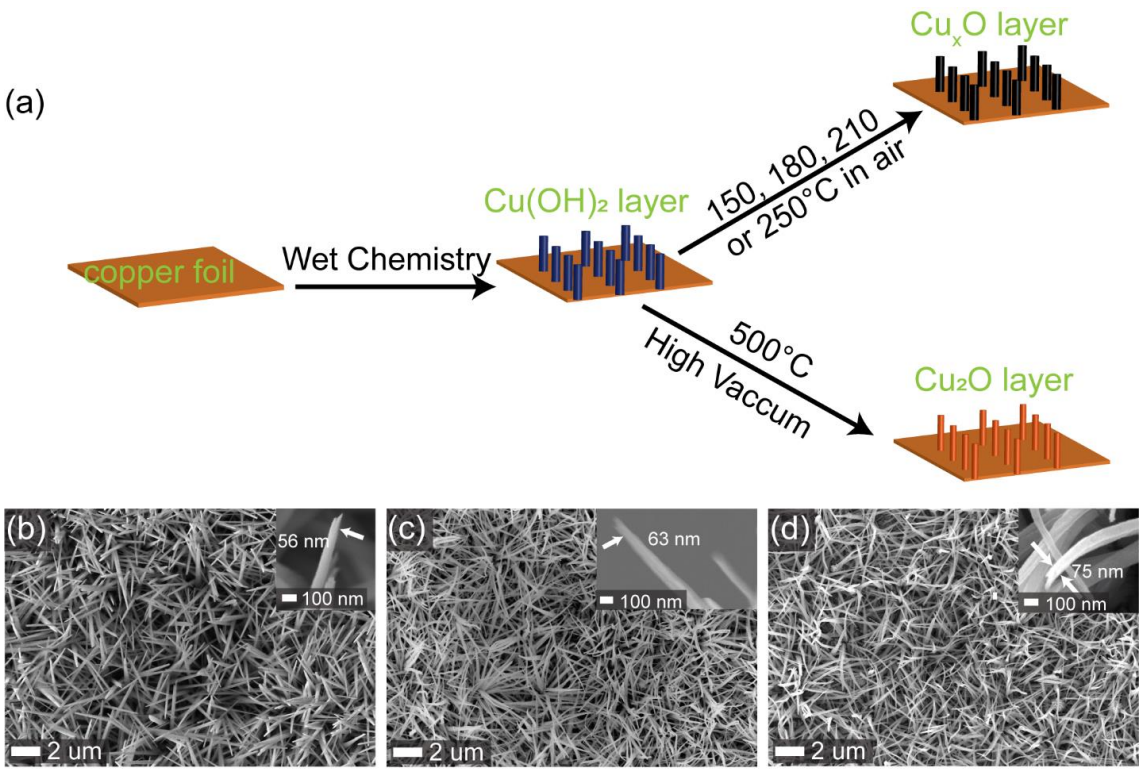

Figure 6.1 (a) Schematic illustration of the synthesis procedures for the Cu_xO nanowire layers; SEM images of the (b) $Cu(OH)_2$, (c) A-180 and (d) A-250 samples, with insets revealing the nanowires under higher magnifications.

Through a wet chemistry process, as described in the experimental section and depicted in Figure 6.1a, we have prepared $Cu(OH)_2$ nanowires (Figure 6.1b) from copper foil. The diameters of the $Cu(OH)_2$ nanowires were as small as 56 nm. After annealing the $Cu(OH)_2$ samples at 180 ºC (*i.e.* the A-180 sample) and 250 ºC (*i.e.* the A-250 sample), both samples still had a dense-nanowire morphology, although a slight increase in the diameter of the nanowires with increased annealing temperature was observed.

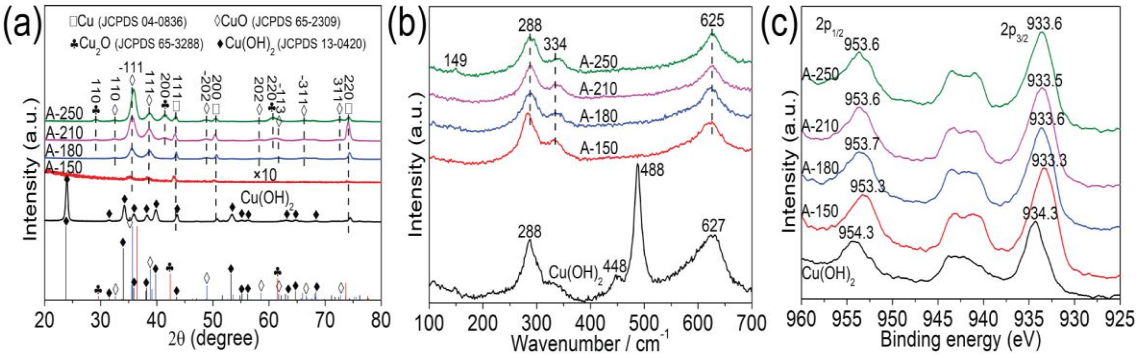

Figure 6.2 (a) X-ray diffraction patterns, (b) Raman spectra, and (c) XPS spectra of the obtained $Cu(OH)_2$, as well as the A-150, A-180, A-210 and A-250 samples.

The crystal structures of the various nanowires were examined by XRD, and the spectra are shown in Figure 6.2a. For the $Cu(OH)_2$ nanowires, several strong peaks associated with copper hydroxide (JCPDS 13-0420) could be identified. Two additional small peaks that could be attributed to the copper substrate (JCPDS 04-0836) were also seen. After annealing, the copper hydroxide peaks disappeared. For the sample annealed at 150 ºC, low-intensity peaks ascribed to CuO (JCPDS 65-2309) were detected. For the samples annealed at 180 ºC or higher, the intensity of the CuO peaks was much stronger. The main peaks could be indexed to the (-111), (111), (-113), (-202) and (110) planes of CuO. For the samples annealed at 210 ºC and 250 ºC, additional peaks associated with the Cu_2O phase (JCPDS 65-3288) were detected. This suggests that, upon annealing, the $Cu(OH)_2$ sample transforms first to CuO at moderate annealing temperatures, and then to a mixture of CuO and Cu_2O at higher temperatures.

The Raman spectra of the different samples are displayed in Figure 6.2b. CuO has a C^6_{2h} space group structure and each primitive cell contains two molecules. Among the nine zone-center optical phonon modes with symmetries $3A_u + 3B_u + A_g + 2B_g$ [35], there are three Raman active modes ($A_g + 2B_g$) [36] for CuO. According to results in the

literature [36,37], we can assign the peak at 288 cm^{-1} to the A_g mode and the peaks at 334 and 625 cm^{-1} to the B_g modes. For all samples except for the $Cu(OH)_2$ and A-250 sample, only CuO vibrational modes were observed. For the A-250 sample, an extra peak at 149 cm^{-1} related to the intrinsic Γ_{15}^- IR active modes of the Cu_2O phase [37,38] was observed. This suggests that in addition to CuO, Cu_2O was also formed in the sample annealed at 250 ºC.

The surface states of the samples were analyzed using XPS. Figure 6.2c shows the XPS spectra of the samples. A set of peaks including the Cu $2p_{3/2}$ peak (934.3 eV) and the Cu $2p_{1/2}$ peak (954.3 eV) were observed. Meanwhile, additional intense satellite peaks of Cu(II) were also observed [39]. These peaks are ascribed to the standard peaks of $Cu(OH)_2$. For those samples obtained after annealing, in addition to the intense satellite peaks ascribed to the binding energies of CuO, the Cu $2p_{3/2}$ and $2p_{1/2}$ peaks were identified to be at 933.3–933.6 eV and 953.3–953.7 eV, respectively [10,39].

In the transformation of copper hydroxide to copper oxide, the annealing temperature plays a key role. Annealing at 150 ºC for 3 h was insufficient for the formation of highly crystalline copper oxide, as evidenced by the XRD results (Figure 6.2a). When the annealing temperature was increased to 180 ºC, CuO with a high degree of crystallinity was formed. An additional Cu_2O phase was observed for the samples annealed at a temperature higher than 210 ºC. Previous reports have revealed that under an oxygen-moderate environment and a high annealing temperature, a Cu_2O mid-layer can form from the oxidization of the copper substrate and the removal of oxygen from the CuO lattice [29,40]. This may be the reason why Cu_2O were detected on the samples annealed at higher temperatures by XRD (Figure 6.2a). In contrast to XRD, only peaks ascribed to CuO were detected by XPS. As XPS is a surface characterization technique,

only the surface CuO was detected, and therefore the Cu_2O mid layer is not detected. For Raman spectroscopy, since the probing depth of the Raman laser is between that of XRD and XPS, a weak Cu_2O signal could be detected for the sample with the highest annealing temperature of 250 ºC. In summary, an annealing temperature of 180 ºC may be optimal to obtain nanowires with a pure CuO phase and high degree of crystallinity.

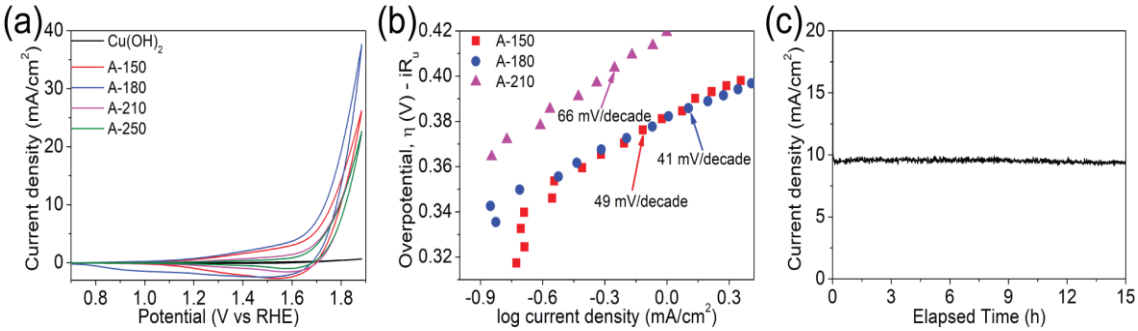

Figure 6.3 (a) Cyclic voltammogram (CV) curves of $Cu(OH)_2$, A-150, A-180, A-210 and A-250 samples for the OER without *iR* compensation with a scan rate of 50 mV s^{-1}. (b) Tafel plots collected from the steady-state CV measurement at a scan rate of 1 mV s^{-1}, which have been corrected for the *iR* drop of the solution. (c) Current density *vs.* time (*J*–*t*) curve of the A-180 sample obtained by fixing the electrolysis potential at 1.77 V *vs.* RHE without *iR* correction. The electrolyte was 1 M Na_2CO_3 (pH ≈ 10.8).

CV curves of the samples are shown in Figure 6.3a. The $Cu(OH)_2$ sample showed the lowest current density among all samples, with a maximum current density of 0.64 mA/cm^2 at a potential of 1.88 V. Upon annealing, the current density of all of the samples increased drastically. The A-180 sample exhibited the highest OER activity. The current density was 5 mA/cm^2 at 1.65 V (overpotential η = 0.42 V), 10 mA/cm^2 at 1.73 V (η = 0.5 V), and 37.64 mA/cm^2 at 1.88 V (η = 0.65 V). The current density of the A-150 sample

was slightly lower, and the potentials required for 5 mA/cm^2 and 10 mA/cm^2 were 1.69 V and 1.76 V, respectively. The current density for the A-210 and A-250 samples were very similar, which required 1.79 V and 1.80 V for 10 mA/cm^2. For the Cu_2O sample (Figure 6.4), the potential required for 10 mA/cm^2 was 1.86 V, which was higher than that of the A-210 and A-250 samples, indicating that the Cu_2O sample had the lowest OER activity among all of the samples.

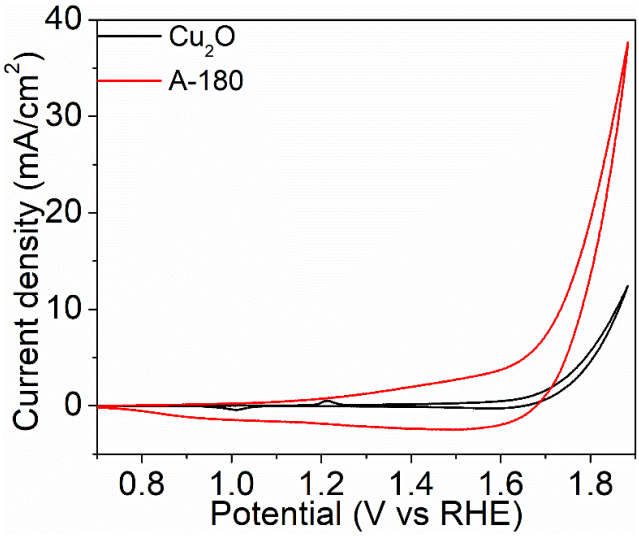

Figure 6.4 Cyclic voltammogram (CV) of Cu_2O nanowires, which was prepared by annealing the $Cu(OH)_2$ nanowires under high vaccum chamber (~ 10^{-5} Pa) at 500 °C for 3 h, and the A-180 sample for OER without *iR* compensation with a scan rate of 50 mV s^{-1}.

In Figure 6.3b, the Tafel plots, OER current density as a function of the overpotential (log (*i*) *vs.* η), of the A-180, A-150 and A-210 samples are shown. The Tafel slopes for the A-180, A-150 and A-210 samples are 41, 49, and 66 mV/decade, respectively. The smallest Tafel slope of the A-180 sample provides an evidence for the superior OER

activity of this sample, as a small Tafel slope indicates a catalyst is of good quality and has a high activity [41]. Mass transfer is favorable in catalysts with high-aspect-ratio morphologies and high crystallinities, because such structures reduce scattering losses during electron transfer [42,43]. Smaller Tafel slopes generally indicate smaller internal barriers for electron and mass transport [32]. This may help to explain why the current density of the A-180 sample is larger than that of the A-150 sample. The formation of Cu_2O at high annealing temperatures leads to a decrease in the current density and an increase in the Tafel slope, demonstrating that CuO performs better as an electrode for OER. Moreover, the dense nanowire morphology could reduce the scattering loss during the electron transfer process and offer a large surface area for the active species to take part in the OER. Overall, the A-180 sample, with a large surface area and a highly crystalline CuO active phase not only has the highest water oxygen ability among our samples, but also boasts one of the best results ever reported for Cu-based OER catalysts [10,30–32].

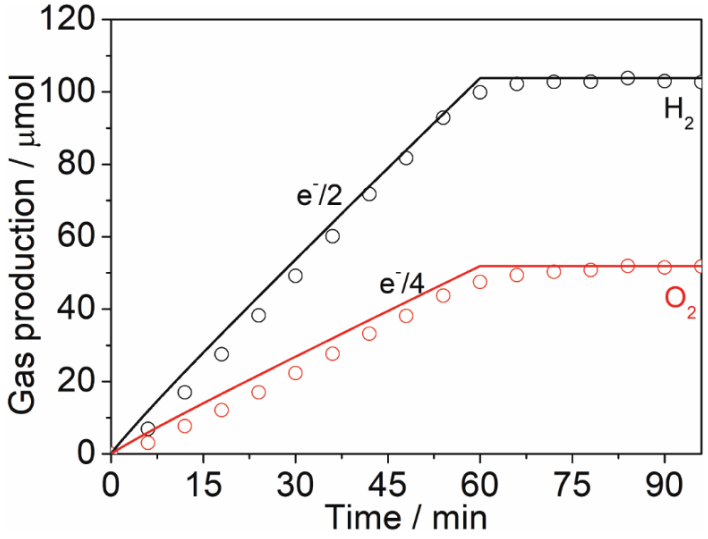

Figure 6.5 The time-dependent hydrogen and oxygen evolution for the A-180 electrode in a three-electrode configuration with an applied potential of 1.77 V *vs.* RHE without *iR* correction. The solid curves labelled $e^-/2$ and $e^-/4$ stand for the theoretical amount for hydrogen and oxygen evolution which are generated at unity faradaic efficiency. The empty circles correspond to the recorded amount of hydrogen and oxygen gases detected during the measurement. The electrolyte was 1 M Na_2CO_3 (pH ≈ 10.8).

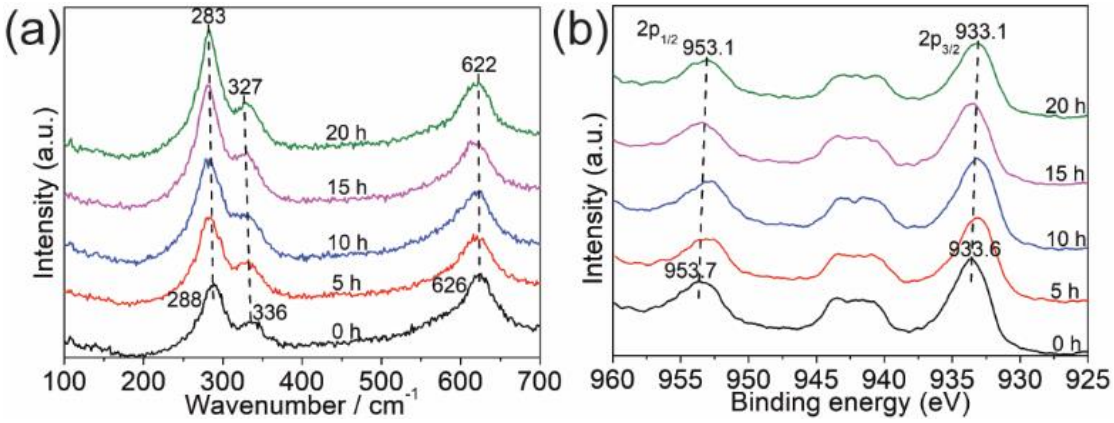

Figure 6.6 (a) Raman spectra and (b) XPS spectra of the A-180 sample after 0, 5, 10, 15, and 20 h of the stability tests.

Controlled-potential water electrolysis test was done to verify the long-term performance and stability of the A-180 electrode, as shown in Figure 6.3c. With an applied potential of 1.77 V (η = 0.54 V), the current density remained nearly constant at 10 mA/cm^2 for more than 15 h. The small fluctuations in the current were attributed to the formation and detachment of O_2 bubbles on the electrode surface. The corresponding gas evolution was analyzed by on-line micro-gas chromatography, as shown in Figure 6.5. For the 1-hour test, the amounts of hydrogen and oxygen gases produced were about 103.8 μmol and 51.9 μmol, respectively, which correspond to a faradaic efficiency of nearly 100%. To investigate the stability of the electrode, SEM, Raman and XPS characterizations of the A-180 electrodes were carried out after using the electrodes for 5 h, 10 h, 15 h and 20 h in the water electrolysis reaction. The Raman results (Figure 6.6a) showed that the vibrational peaks of CuO were preserved throughout the reaction [36,37]. For the XPS results, shown in Figure 6.6b, the peak values of 933.1–933.6 eV for Cu $2p_{3/2}$ and 953.1–953.7 eV for Cu $2p_{1/2}$ were still consistent with the binding energies of CuO [10,39]. Moreover, after a test of 20 h, as shown in Figure 6.7, the A-180 electrode still had the optical appearance of CuO.

Figure 6.7 Optical appearance of the A-180 sample at the beginning of the stability test (left) and at the end of 20 h of the stability test (right).

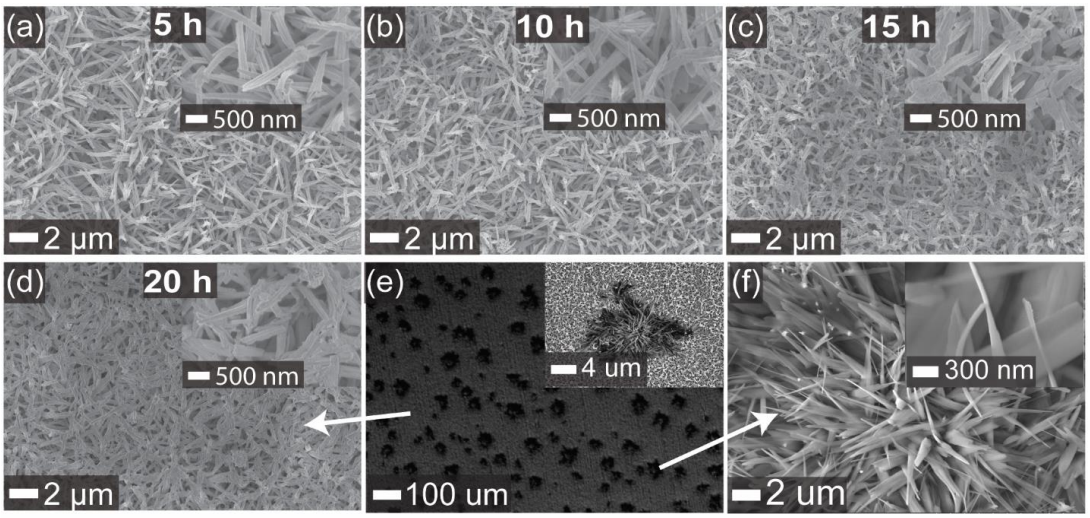

Figure 6.8 (a–c) SEM images of the A-180 sample after 5 h (a), 10 h (b) and 15 h (c) of the stability tests. (d–f) SEM images of the A-180 sample after 20 h of the stability test, with panel (e) showing the top-view morphology of the whole layer, and panel (d) and (f) showing the nanowire part and the clumps of nanosheets, respectively.

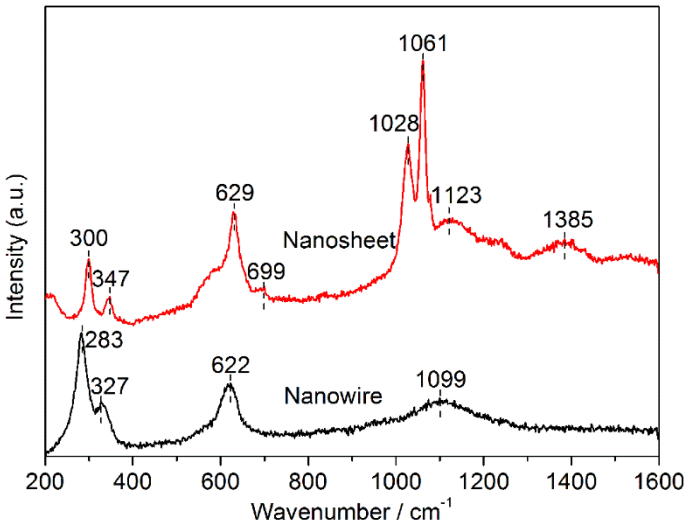

Figure 6.9 Raman spectra of the A-180 sample after 20 h of the stability test. The tested parts include the nanowires and nanosheets, as shown in Figure 6e.

With increased electrolysis time, the morphology of the nanowires in the A-180 sample remained unchanged, as can be seen in Figure 6.8. However, the nanowires tended to aggregate over time during the reaction (especially after 15 h), as confirmed by the magnified SEM images shown in the insets in Figure 6.8c–d. It is notable that after 20 h, nanosheet clumps were formed on some parts of the nanowire layer, as shown in Figure 6.7f. A Raman spectrum of the nanosheets is shown in Figure 6.9. In addition to the CuO peaks described earlier, peaks at 699 cm^{-1} and 1385 cm^{-1} attributed to the v_4 and v_3 regions of CO_3^{2-} and two more peaks at 1028 and 1061 cm^{-1} attributed to the v_1 symmetric stretching region of CO_3^{2-} were also found [44]. In this regard, it is speculated that CO_3^{2-} has been incorporated into the nanosheets and plays some role in their formation.

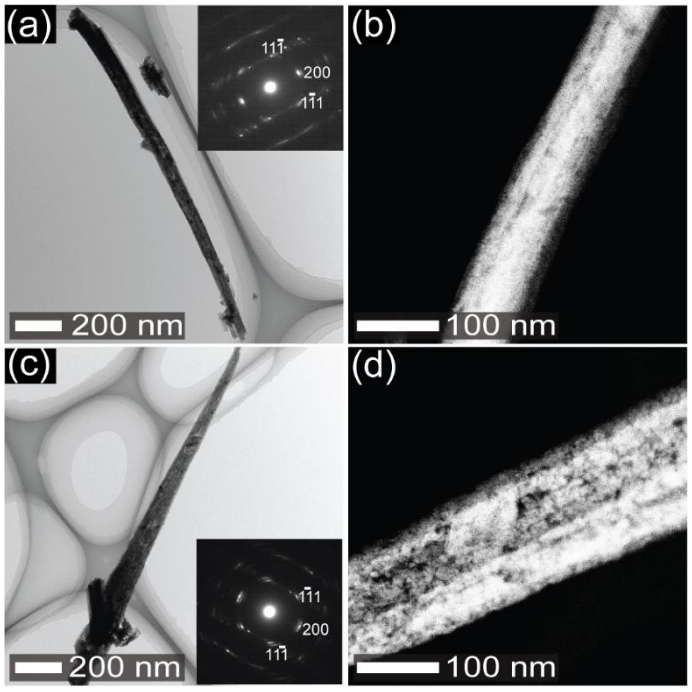

Figure 6.10 TEM images (a, c) and HAADF-STEM images (b, d) of the A-180 sample before (a–b) and after the 15-hour stability test (c–d). Insets of (a) and (c) are SAED patterns.

TEM and HAADF-STEM characterizations were exploited to further study the reason for the morphological change of the A-180 sample. Bright-field TEM images of a single nanowire before and after the 15-hour stability test are shown in Figure 6.10a and Figure 6.10c. The selected-area electron diffraction (SAED) patterns (insets in Figure 6.10a and Figure 6.10c) display similar diffraction spots corresponding to the monoclinic CuO phase for the samples before and after the 15-hour reaction [45]. However, some dark spots appeared in Figure 6.10d, whereas the contrast in Figure 6.10b was rather uniform. Since the intensity of the HAADF-STEM signal is sensitive to the sample thickness (if the atomic number of the materials is the same), a darker region suggests a thinner thickness. Given the dark regions distribute mostly in the middle of the nanowires, as exhibited in Figure 6.10d, it is likely that after the 15-hour water electrolysis reaction, some inner copper ions diffused to the outside, resulting in a decreased density or the emergence of porosity in these CuO nanowires.

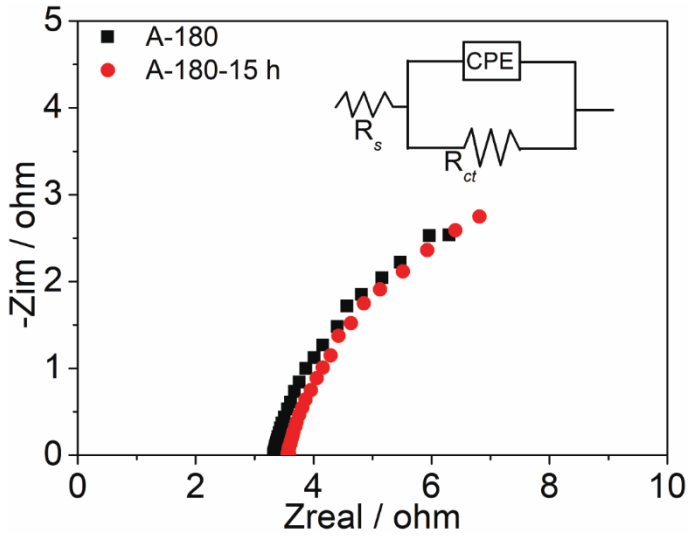

Figure 6.11 Nyquist plots of the A-180 sample before and after the 15-hour stability test. The inset shows the according equivalent circuit.

The electrochemical double-layer capacitance (C_{dl}) can be used to calculate the electrochemically active surface area (ECSA) according to the formula ECSA = C_{dl}/C_s, where C_s is the constant related to the sample properties and its surface under identical electrolyte conditions [8,46]. Figure 6.11 shows the EIS measurements of the A-180 sample before and after the 15-hour stability test (namely A-180-15 h). The calculated C_{dl} for the A-180 and A-180-15 h samples were 0.026 mF cm^{-2} and 0.024 cm^{-2}, respectively, suggesting the ECSA of the A-180 CuO electrode was nearly unchanged after the stability test.

Based on the Raman and XPS results (Figure 6.6), it is clear that even after the 15-hour reaction, the chemical composition of the A-180 sample does not change, and it is still composed of CuO. With this understanding, it could be supposed that during the electrolysis reaction, copper ions have diffused from the interior to the surface of the nanowires, leading to an increase in the porosity and a decrease in the density of the nanowires. The diffused copper ions may fuse individual nanowires together, resulting in the aggregation of nanowires, as illustrated in Figure 6.12 from panel a to panel b. The surface area of the active CuO species provided by the aggregated CuO nanowires is similar to the area provided by the non-aggregated nanowires, and therefore the current density remains stable despite the morphological change.

The reason for the formation of the nanosheets after 20 h of the stability test is still under investigation. We propose a possible explanation: the nanosheets were formed directly from the nanowires, as illustrated in Figure 6.12. In the electrolysis process, copper ions diffuse from the interior to the surface of the nanowires and thus cause the aggregation of nanowires with decreased density (Figure 6.12a and Figure 6.12b). Afterwards, the aggregated CuO nanowires transform into nanosheets with the help of

CO_3^{2-}, as illustrated in Figure 6.12b and Figure 6.12c.

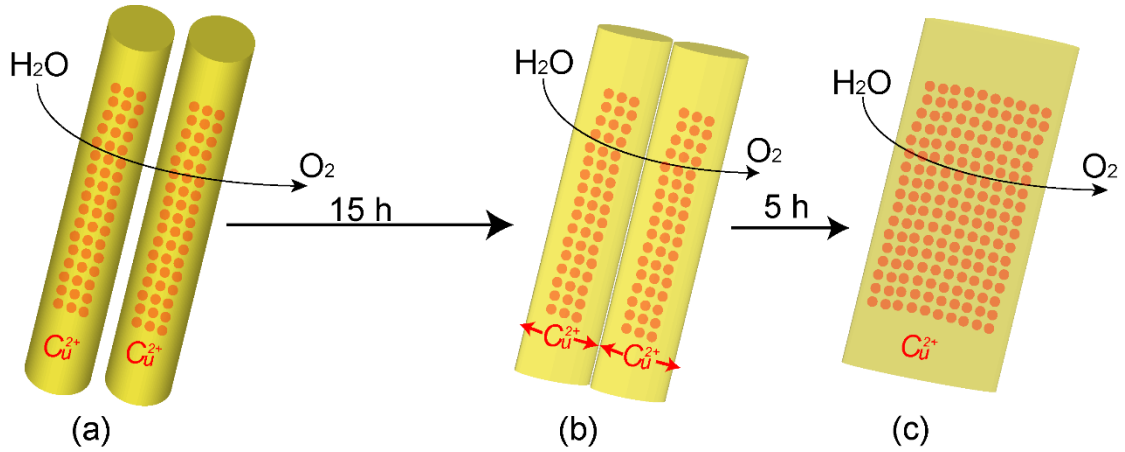

Figure 6.12 The morphological transformation process of CuO from nanowires to nanosheets during the reaction.

6.4 Conclusion

The OER activities of $Cu(OH)_2$, Cu_2O, CuO_x and CuO with varied degrees of crystallization were investigated experimentally. The nanowires composed of $Cu(OH)_2$ or Cu_2O showed poor activity towards the OER in water electrolysis. With improved crystallinity and the formation of CuO, the OER activity increased drastically. The A-180 sample showed the highest water splitting ability, the smallest Tafel slope of 41 mV/decade and almost 100% faradaic efficiency, as a result of the large amount of the active species (*i.e.* crystalline CuO). After a 15-hour stability test, the chemical composition of the electrode remained unchanged, resulting in a stable current density over time. During the stable water electrolysis, especially after 10 hours of test, copper ions diffused from the interior to the surface of the nanowires, leading to a decrease in the density and an increase in the porosity of the nanowires. The diffused copper ions may deposit between individual nanowires, resulting in the connection and aggregation of the nanowires. These aggregated CuO nanowires could still provide a sufficient amount of the active species for the OER. This may be the reason why the current remained stable despite the morphological change. Finally, a new nanosheet morphology formed after 20 hours of the stability test. This offers a novel methodology for the preparation of composites of nanosheets and nanowires from single-component nanowire templates. In conclusion, we have presented a facile and low-cost method for the synthesis of a highly efficient electrode for the OER using crystalline CuO as the active species, and explored the origin of the high efficiency and long-term stability.

References

1 Yu, J.; Si, Z.; Chen, L.; Wu, X.; Weng, D. *Appl. Catal. B Environ.* **2015**, *163*, 223-232.

2 Mamaca, N.; Mayousse, E.; Arrii-Clacens, S.; Napporn, T. W.; Servat, K.; Guillet, N.; Kokoh, K. B. *Appl. Catal. B Environ.* **2012**, *111-112*, 376-380.

3 da Silva, G. C.; Perini, N.; Ticianelli, E. A. *Appl. Catal. B Environ.* **2017**, *218*, 287-297.

4 Heo, I.; Wiebenga, M. H.; Gaudet, J. R.; Nam, I. S.; Li, W.; Kim, C. H. *Appl. Catal. B Environ.* **2014**, *160-161*, 365-373.

5 Ng, J. W. D.; García-Melchor, M.; Bajdich, M.; Chakthranont, P.; Kirk, C.; Vojvodic, A.; Jaramillo, T. F. *Nat. Energy* **2016**, *1*, 16053.

6 Zhong, M.; Hisatomi, T.; Kuang, Y.; Zhao, J.; Liu, M.; Iwase, A.; Jia, Q.; Nishiyama, H.; Minegishi, T.; Nakabayashi, M.; Shibata, N.; Niishiro, R.; Katayama, C.; Shibano, H.; Katayama, M.; Kudo, A.; Yamada, T.; Domen, K. *J. Am. Chem. Soc.* **2015**, *137*, 5053-5060.

7 Cao, Q.; Yu, J.; Yuan, K. P.; Zhong, M.; Delaunay, J.-J. *ACS Appl. Mater. Interfaces* **2017**, *9*, 19507–19512.

8 McCrory, C. C. L.; Jung, S.; Peters, J. C.; Jaramillo, T. F. *J. Am. Chem. Soc.* **2013**, *135*, 16977-16987.

9 Feng, J.-X.; Ye, S.-H.; Xu, H.; Tong, Y.-X.; Li, G.-R. *Adv. Mater.* **2016**, *28*, 4698-4703.

10 Du, J.; Chen, Z.; Ye, S.; Wiley, B. J.; Meyer, T. J. *Angew. Chem., Int. Ed.* **2015**, *54*, 2073-2080.

11 Zhong, M.; Hisatomi, T.; Sasaki, Y.; Suzuki, S.; Teshima, K.; Nakabayashi, M.; Shibata, N.; Nishiyama, H.; Katayama, M.; Yamada, T.; Domen, K. *Angew. Chem., Int. Ed.* **2017**, 1-6.

12 Peng, X.; Wang, L.; Hu, L.; Li, Y.; Gao, B.; Song, H.; Huang, C.; Zhang, X.; Fu, J.; Huo, K. *Nano Energy* **2017**, *34*, 1-7.

13 Chen, H.; Zhang, Q.; Han, X.; Cai, J.; Liu, M.; Yang, Y.; Zhang, K. *J. Mater. Chem. A* **2015**, *3*, 24022-24032.

14 Lu, X. F.; Liao, P. Q.; Wang, J. W.; Wu, J. X.; Chen, X. W.; He, C. T.; Zhang, J. P.; Li, G. R.; Chen, X. M. *J. Am. Chem. Soc.* **2016**, *138*, 8336-8339.

15 Feng, J. X.; Xu, H.; Dong, Y. T.; Ye, S. H.; Tong, Y. X.; Li, G. R. *Angew. Chem., Int. Ed.* **2016**, *55*, 3694-3698.

16 Lu, X. F.; Gu, L. F.; Wang, J. W.; Wu, J. X.; Liao, P. Q.; Li, G. R. *Advanced Materials* **2017**, *29*, 1604437.

17 Wang, H. Y.;Hsu, Y. Y.;Chen, R.;Chan, T. S.;Chen, H. M.; Liu, B. *Adv. Mater.* **2015**, *5*, 1-8.

18 Li, S.; Wang, Y.; Peng, S.; Zhang, L.; Al‐Enizi, A. M.; Zhang, H.; Sun, X.; Zheng, G. *Adv. Energy Mater.* **2016**, *6*, 1501661.

19 Zhan, T.; Liu, X.; Lu, S. S.; Hou, W. *Appl. Catal. B Environ.* **2017**, *205*, 551-558.

20 Li, L.; Zhang, L.; Ma, K.; Zou, W.; Cao, Y.; Xiong, Y.; Tang, C.; Dong, L. *Appl. Catal. B Environ.* **2017**, *207*, 366-375.

21 Xu, W.; Lan, R.; Du, D.; Humphreys, J.; Walker, M.; Wu, Z.; Wang, H.; Tao, S. *Appl. Catal. B Environ.* **2017**, *218*, 470-479.

22 Berenguer, R.; La Rosa-Toro, A.; Quijada, C.; Morallón, E. *Appl. Catal. B Environ.* **2017**, *207*, 286-296.

23 Cao, Q.; Che, R. C.; Chen, N. *Appl. Catal. B Environ.* **2017**, *162*, 187-195.

24 Ye, Z.; Giraudon, J.-M.; Nuns, N.; Simon, P.; De Geyter, N.; Morent, R.; Lamonier, J.-F. *Appl. Catal. B Environ.* **2018**, *233*, 154-166.

25 Liu, X.; Sui, Y.; Yang, X.; Wei, Y.; Zou, B. *ACS Appl. Mater. Interfaces* **2016**, *8*, 26886-26894.

26 Wang, G.; Sui, Y.; Zhang, M.; Xu, M.; Zeng, Q.; Liu, C.; Liu, X.; Du, F.; Zou, B. *J. Mater. Chem. A* **2017**, *5*, 18577-18584.

27 Paracchino, A.; Mathews, N.; Hisatomi, T.; Stefik, M.; Tilley, S. D.; Grätzel, M. *Energy Environ. Sci.* **2012**, *5*, 8673-8681.

28 Luo, J.; Steier, L.; Son, M. K.; Schreier, M.; Mayer, M. T.; Grätzel, M. *Nano lett.* **2016**, *16*, 1848-1857.

29 Li, C.; Hisatomi, T.; Watanabe, O.; Nakabayashi, M.; Shibata, N.; Domen, K.; Delaunay, J.-J. *Energy Environ. Sci.* **2015**, *8*, 1493-1500.

30 Barnett, S. M.; Goldberg, K. I.; Mayer, J. M. *Nat. Chem.* **2012**, *4*, 498-502.

31 Chen, Z.; Meyer, T. J. *Angew. Chem., Int. Ed.* **2013**, *52*, 700-703.

32 Yu, F.; Li, F.; Zhang, B.; Li, H.; Sun, L. *ACS Catal.* **2015**, *5*, 627-630.

33 Hou, C. C.; Fu, W. F.; Chen, Y. *ChemSusChem* **2016**, *9*, 2069-2073.

34 Zhang, W.; Wen, X.; Yang, S.; Berta, Y.; Wang, Z. L. *Adv. Mater.* **2003**, *15*, 822-825.

35 Reichardt, W.; Gompf, F.; Aïn, M.; Wanklyn, B. M. *Zeitschrift für Phys. B Condens. Matter* **1990**, *81*, 19-24.

36 Xu, J. F.; Ji, W.; Shen, Z. X.; Li, W. S.; Tang, S. H.; Ye, X. R.; Jia, D. Z.; Xin, X. Q. *J. Raman Spectrosc.* **1999**, *30*, 413-415.

37 Deng, Y.; Handoko, A. D.; Du, Y.; Xi, S.; Yeo, B. S. *ACS Catal.* **2016**, *6*, 2473-

2481.

38 Reydellet, J.; Balkanski, M.; Trivich, D. *Phys. Status Solidi* **1972**, *52*, 175-185.

39 Chastain, J.; King, R. C.; Moulder, J. F. *Handbook of X-ray photoelectron spectroscopy: a reference book of standard spectra for identification and interpretation of XPS data*; Physical Electronics Eden Prairie, MN, **1995**.

40 Li, C.; Li, Y.; Delaunay, J. J. *ACS Appl. Mater. Interfaces* **2014**, *6*, 480-486.

41 Tahir, M.; Pan, L.; Idrees, F.; Zhang, X.; Wang, L.; Zou, J.-J.; Wang, Z. L. *Nano Energy* **2017**, *37*, 136-157.

42 Pickrahn, K. L.; Park, S. W.; Gorlin, Y.; Lee, H. B. R.; Jaramillo, T. F.; Bent, S. F. *Adv. Energy Mater.* **2012**, *2*, 1269-1277.

43 Mao, S.; Lu, G.; Chen, J. *Nanoscale* **2015**, *7*, 6924-6943.

44 Brooker, M. H.; Bates, J. B. *J. Chem. Phys.* **1971**, *54*, 4788-4796.

45 Su, D.; Xie, X.; Dou, S.; Wang, G. *Sci. Rep.* **2014**, *4*, 5753.

46 Trasatti, S.; Petrii, O. *Pure Appl. Chem.* **1991**, *63*, 711-734.